RARE EARTH BASED MIXED METAL OXIDES FOR ENERGY APPLICATIONS

THESIS SUBMITTED TO AcSIR FOR THE AWARD OF THE DEGREE OF

DOCTOR OF PHILOSOPHY

IN CHEMICAL SCIENCES

By

GAYATHRI T. H.

Registration No: 10CC11A39002

Under the guidance of

Dr. S. ANANTHAKUMAR

MATERIALS SCIENCE AND TECHNOLOGY DIVISION

NATIONAL INSTITUTE FOR INTERDISCIPLINARY

SCIENCE AND TECHNOLOGY (CSIR-NIIST)

THIRUVANANTHAPURAM- 695 019

KERALA, INDIA

August, 2017

In loving memories of

Jose Sir

&

My "Ilayachan"

(Somanathan T. P.)

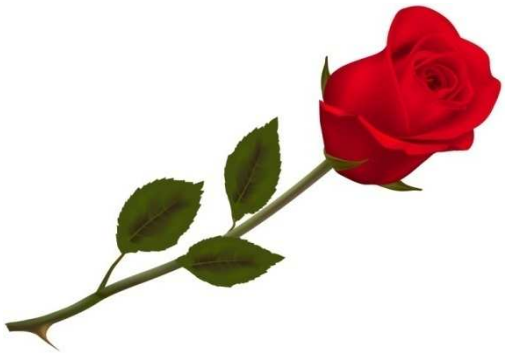

Dedicated to

My Beloved Family...

DECLARATION

I hereby declare that the matter embodied in the Ph. D. thesis entitled: "**Rare earth based mixed metal oxides for energy applications**" is the result of the investigations carried out by me at the Functional Materials Section, Materials Science and Technology Division, CSIR-National Institute for Interdisciplinary Science and Technology (CSIR-NIIST), Thiruvananthapuram, under the supervision of Dr. S. Ananthakumar and the same has not been submitted elsewhere for any other degree, diploma or title.

In keeping with the general practice of reporting scientific observations, due acknowledgement has been made wherever the work described is based on the findings of other investigators.

Gayathri T. H.

Thiruvananthapuram

August 2017

COUNCIL OF SCIENTIFIC & INDUSTRIAL RESEARCH
NATIONAL INSTITUTE FOR INTERDISCIPLINARY SCIENCE AND TECHNOLOGY (CSIR-NIIST)
Industrial Estate P.O., Pappanamcode Thiruvananthapuram - 695 019, Kerala, INDIA
www.niist.res.in

Dr. S. Ananthakumar
Senior Principal Scientist
Functional Materials Section
Materials Science and Technology Division

Off: 0471-2515289
Mob: 09497271547
Fax: +91-471-2491712
E-mail: ananthakumar70@gmail.com

CERTIFICATE

*This is to certify that the work incorporated in this Ph.D. thesis entitled "***Rare earth based mixed metal oxides for energy applications***" submitted by* ***Ms. Gayathri T. H.*** *to the Academy of Scientific and Innovative Research (AcSIR) in partial fulfillment of the requirements for the award of the* ***Degree of Doctor of Philosophy in Chemical Sciences*** *embodies original research work carried out by her under my supervision. I further certify that this work has not been submitted to any other University or Institution in part or full for the award of any degree or diploma. Research material obtained from other sources has been duly acknowledged in the thesis. Any text, illustration, table etc., used in the thesis from other sources, have been duly cited and acknowledged.*

Dr. S. Ananthakumar
(Supervisor)

Thiruvananthapuram
August 2017

Acknowledgements

I present this thesis, in the name of GOD, the Almighty, who showers HIS unperturbed blessings undeservingly upon me throughout my life.

This thesis is the end of my journey in obtaining my Ph.D. I have not travelled in a vacuum in this journey. This thesis has been kept on track and been seen through to completion with the support and encouragement of numerous people including my well-wishers, my friends and colleagues. I would like to thank all those people who made this thesis possible and an unforgettable experience for me. At the end of my thesis, it is a pleasant task to express my thanks to all those who contributed in many ways to the success of this study and made it an unforgettable experience for me.

At this moment of accomplishment, first of all I pay homage to my former guide, Late. Dr. Jose James. This work would not have been possible without his guidance, support and encouragement. Under his guidance I successfully overcame many difficulties and learned a lot. His unflinching courage and conviction will always inspire me, and I hope to continue to work with his noble thoughts. I wish his soul roots in peace and solace in the heaven. I can only say a proper thanks to him through my future work. This work is a tribute to him.

I offer my sincere gratitude to my supervisor, Dr. S. Ananthakumar, for his guidance, understanding, patience and encouragement and also for providing necessary infrastructure and resources to accomplish my research work. I am extremely indebted to him for picking me up as a student at the critical stage of my Ph.D. I warmly thank him, for his valuable advice, constructive criticism and his extensive discussions around the final stage of my thesis work.

Words fail me to express my deepest sense of gratitude to Dr. Aleksey A. Yaremchenko, University of Aveiro, Portugal, for his unconditional support. This work would not have been possible without his guidance and help. I extend my gratitude to Mr. K. Zakharchuk and J. Macias, University of Aveiro, for their valuable help.

I would like to convey my gratitude to Dr. A. Ajayaghosh, Director, CSIR-NIIST, Thiruvananthapuram, Dr. Suresh Das and Dr. Gangan Prathap, (former Directors, NIIST), for providing all the research facilities for my Ph. D. Work.

I wish to thank Dr. P. Prabhakar Rao (Head, Materials Science and Technology Division, NIIST), Dr. M. L. P. Reddy, Dr. M. T. Sebastian and Dr. K. G. K. Warrier (former Heads, MSTD) for their help rendered during the course of this work.

I wish to express my since thanks to my doctoral committee members Dr. K. P. Surendran, Dr. U. S. Hareesh and Dr. Mangalam S. Nair for their understanding, encouragement and personal attention which have provided good and smooth basis for my Ph.D. tenure and also for their helpful suggestions and comments during my presentations.

I am deeply indebted to Dr. G. Subodh and Dr. S. Rajesh for their valuable help at the critical stage of my research carrier.

I am thankful to Dr. K. G. Nishanth, Dr. Manoj Raama Varma, Dr. S. Shukla, Dr. M vasundhara, Dr. Senoy Thomas for their support. The support provided by other scientists of NIIST is also thankfully acknowledged.

I am extending my gratitude to Mr. M. R. Chandran, Mr. A. Peer Mohammed, Ms. Soumya, Mr. Prithviraj, Mr. Kiran Mohan and Ms. Luci Paul for helping me in many ways. I am very thankful to all scientists, students and staff members of Materials Science and Technology Division for their help and support. I convey my special acknowledgments to Administrative section, Finance and Account section, Stores and Purchase Section, and Library and Information section for extending me various services to facilitate my research program. I am also thankful to Dr. T. Premkumar of CSIR-CECRI for providing me the measurement facility.

The creative suggestions, valuable advices and helps given by my seniors in the lab, Dr. Danesh Thomas, Dr. Manu K. M., Dr. Jobin Varghese, Dr. Nina Joseph, Dr. Chameswari J., and Dr. Neenulekshmi P. are greatly acknowledged.

I would also like to extend huge, warm thanks to the companionship, support, and generous care of Dr. Deepa K. S. and Dr. Namitha L. K., both of them were always beside me during the happy and hard moments to push me and motivate me.

My wholehearted gratitude to my colleagues: Ms. Aiswarya R., Mr. Dijith K. S., Ms. Lekshmi D. R., Ms. Angel Mary Joseph, Ms. Kanakangi S. Nair, Mr. K. Krishnakumar, Ms. Induja I. J., Ms, Roshni S. Babu, Mr. Arun S., Ms. Heera Menon, Mr. Sikander Ahammed, Ms. Ann Rose Sunny, Ms. Varsha Viswanath, Mr. Arun B., Ms. Varsha G. S., Ms. Sreejitha Prajith, Ms. Sumi Sanju with whom I have spent many memorable occasions and who have been very helpful and supportive both in personal and academic. I would also like to thank some people from early days of my research tenure, Dr. Sameera S., Dr. Mariyam Thomas were among those who kept me going at the beginning.

I take this opportunity to sincerely acknowledge the Council of Scientific and Industrial Research (CSIR), Government of India, New Delhi, for providing financial assistance which buttressed me to perform my work comfortably.

I express my sincere gratitude to all my teachers and well-wishers of my college and school life. I express my deep love and thankfulness to my best friends, Dr. Usha Gangan, Dr. Sambhu R., Mr. Shibin Thomas, Ms. Malini Prabhakaran, Mr. Vishnu Subhash, Dr. Sibi Mathew, Ms. Parvathy M. R. for their love, care and moral support. I would also like to extend huge, warm thanks to my roommates Dr. Harsha N. and Ms. Remya K. for their valuable help and support.

Last but not least, I would like to pay high regards and my heart-felt thanks to my father Haridasan T. P., my mother Rajeswari T. N., my brother Jayakrishnan T. H. and my sister-in-law Anjali for their sincere encouragement, prayers and inspiration throughout my research work and lifting me uphill this phase of life. I express my deepest sense of gratitude to my husband's family members for their patience, care and understanding. Words are short to express my deep sense of gratitude and love towards my husband Abhilash P. for his unconditional love, care, and valuable support to accomplish this goal. During the inevitable ups and downs of conducting my research carrier he was always with me to push me and inspire me. This list is incomplete without acknowledging my little Prince, Ishaan Madhav, for his indefinable love and patience. I owe everything to them. Besides this, I thank several people who have knowingly and unknowingly helped me in the successful completion of this project and apologize for not mentioning all of them personally.

Gayathri T. H.

Contents

Abbreviations

CA	Citric Acid
CCD	Charged Coupled Device
CN	Coordination Number
CPE	Constant Phase Element
CS	Combustion Synthesis
CTE	Coefficient of Thermal Expansion
e.m.f.	Electromotive Force
EDS	Energy Dispersive Spectroscopy
EG	Ethylene Glycol
EIS	Electrochemical Impedance Spectroscopy
EPR	Electron Paramagnetic Resonance
FIC	Fast Ionic Conductor
GOF	Goodness of Fit
HF	High Frequency
HRTEM	High Resolution Transmission Electron Microscope
ICDD	International Centre for Diffraction Data
LF	Low Frequency
$LnVO_4$	Lanthanide Orthovanadates
LSGM	$La_{1-x}Sr_xGa_{1-y}Mg_yO_{3-\delta}$
MRI	Magnetic Resonance Imaging
OPMs	Oxygen Permeable Membranes
PDF	Powder Diffraction File
PL	Photoluminescence
ppm	Parts per Million
PVA	Poly Vinyl Alcohol
$REVO_4$	Rare earth Orthovanadates
SEM	Scanning Electron Microscope
SEOS	Solid Electrolyte Oxygen Separation
SG	Space Group
SIC	Super Ionic Conductor
SOFC	Solid Oxide Fuel Cell
SS	Solid State Synthesis
TMA	Thermomechanical Analyser
TPB	Triple Phase Boundary
TWCs	Two Way Catalysts
XRD	X-ray Diffraction
YSZ	Yttria Stabilized Zirconia
Zircon	$ZrSiO_4$

PREFACE

The topic of reliable, clean and sustainable energy is something that is heavily sought after. This has to do with the increasing global demand for energy and the pressure to boost efficiency and lower emissions, since lots of the energy we are presently using creates a high carbon footprint that is harmful for our environment. In an era when the requirement for traditionally exploited natural resources is outpacing supply, conventional industrial practices are contributing to unwanted climatic change and developing regions are competing for a larger share of limited fuel stocks, the search for innovative ways to meet this necessity becomes more urgent than ever. Materials science is only one aspect of the response to these intimidating challenges, it however has an essential part to play in achieving the ambitious goals. In the past, it has contributed appreciably to advances in the safe, consistent and efficient use of energy and accessible natural resources.

Solid-state inorganic electrolytes play a crucial role in energy conversion and energy storage systems and enable a number of emerging technologies ranging from fuel cells, batteries, gas pumps, sensors, ion exchange membranes, electrolysis, solid electrodes, electrochromics and displays, capacitors, optical materials, timers, and environmental monitoring devices etc. However, for any practical uses, a lot of scientific and technological challenges have been noticed related to the transport of ions in solids. The crystal structure and chemical composition are truly critical to have acceptable ionic transport property. The subject matter of this thesis is to establish a structure - property correlation between the crystal structure, chemical composition and ionic conduction in a group of solid state materials selected from the rare earth based zircon-type mixed metal vanadates. The thesis comprises of six chapters of which **Chapter 1** gives an overview of ionic conductors especially oxide ion conductors, ionic conduction mechanism and applications of oxide ion conductors.

Chapter 2 deals with the synthesis of $LnVO_4$ and magnesium-doped $Ln_{0.95}V_{0.95}Mg_{0.10}O_{4-\delta}$ (Ln = Pr, Sm, Gd, Dy and Er) orthovanadates. Influence of magnesium doping on the structural and electrical characterization of the prepared materials is discussed. In $LnVO_4$ series, highest electrical conductivity is obtained for $PrVO_4$ and $SmVO_4$ and a decreasing trend is seen with increasing atomic number of rare-earth cation. Addition of magnesium results in a drop of electrical conductivity. Interstitial oxygen diffusion is discussed as a prevailing mechanism of ionic transport in undoped $LnVO_4$, whilst acceptor-type magnesium doping suppresses the formation of interstitial oxygen ions. Effect of humidified atmosphere has also investigated.

In **Chapter 3** synthesis of $EuVO_4$ and Mg substituted $EuVO_4$ ceramics $Mg_xEuVO_{4\pm\delta}$ (x = 0-0.5) by solid state method is discussed. The impact of Mg substitution on the prepared materials is investigated. Undoped $EuVO_4$ is predominantly an oxygen-ionic conductor, whereas acceptor-type substitution suppresses total conductivity and oxygen-ionic transport. The variations of electrical transport properties are discussed in terms of interstitial oxygen diffusion in parent $EuVO_4$ and oxygen vacancy diffusion in Mg-substituted vanadate. Impact of humidified atmosphere on the electrical properties of substituted as well as undoped ceramics has also discussed and it indicates a protonic contribution to the total electrical transport for $EuVO_4$.

Chapter 4 focused on the preparation of YVO_4 and Mg substituted YVO_4 ceramics, $Y_{1-x/2}Mg_xV_{1-x/2}O_{4-\delta}$ (x=0.0-0.5) by two synthetic approach viz. solid state as well as combustion method and the effect of Mg substitution on the structural, microstructural and electrical characterization of YVO_4 prepared by both methods. Employment of the combustion method was found to result in a significant decrease of zircon phase formation temperature. In this case a smaller grain size and lower densification on sintering was noticed. Acceptor-type substitution by magnesium is

compensated by the formation of oxygen vacancies and results in a moderate increase of oxygen-ionic conductivity with respect to the parent yttrium vanadate. Combustion-synthesized ceramics showed higher conductivity compared to the samples prepared by conventional solid state reaction method.

In the **fifth chapter**, effect of Li^+ and Ag^+ doping on the structural and electrical properties of zircon-type $SmVO_4$ prepared by solid state route is discussed. Doping by monovalent metal cations improved the conducting property of the parent material with highest conductivity obtained for Ag doped material. The conductivity of Ag doped sample is found to be purely oxygen ionic and can be comparable to the currently known oxide ion conductors like YSZ LSGM, GDC, SDC etc. The final chapter, **Chapter 6**, proposes the scope for some future work.

CHAPTER 1

IONIC CONDUCTORS: CLASSIFICATION, MECHANISM & APPLICATIONS

This chapter is an introduction to ionic conduction in solids, mechanism of ionic conduction and application of ionic conductors in various fields giving emphasis to oxide ion conductors. The chapter begins with a brief introduction of ionic conduction in solids followed by the background of invention and development in this field. Mechanism of ionic conduction and classification of ionic conductors are discussed in later part of the chapter. A detailed introduction to oxide ion conduction in solids is presented followed by a description to zircon structure and a literature survey on the oxide ion conductivity of zircon structured compounds are discussed. Application of oxide ion conductors are presented in the last section and the chapter ends with the scope of the present work.

1.1. INTRODUCTION

Solid state ionic conductors play a vital role in various major scientific investigations and technological applications, especially in the domains of energy conversion and storage and in monitoring environmental changes supported by the progressing growth in fuel cells, battery and sensor technologies[1,2]. It is only in the last few decades that solid state ionic conductors were regarded as exceptions in materials science and the theory and application of these materials have found to gather into a coherent field. Thus the discovery of these materials was considered as a fortuitous event. However, for the last few years, a large number of solids that exhibit anomalously high levels of ionic conductivity have been discovered. In fact, some solid materials exhibit ionic conductivity comparable to those of liquids. These kinds of materials are described as fast ionic conductors. Till now, numerous solid materials varying from ceramics to glass and polymers have been discovered or rediscovered, detected and analysed with fast ionic conduction. In spite of the intensive research on the theory of ionic transport and its significance for solid state reactions, material scientist were mainly focussed on the potential technological importance of these materials in diverse areas including fuel cells, batteries, gas pumps, sensors, ion exchange membranes, electrolysis, solid electrodes, electrochromics and displays, capacitors, optical materials, timers, environmental protection etc. A lot of scientific and technological challenges have been raised related to the transport of ions in solids upon the development of practical devices which in turn formed a ground for solid state ionics to emerge as a major scientific area.[1,3]

Even though, with the exhaustive research for finding new ionic conductors, there is a lack of hike in this field. This is mainly owing to the deficiency of knowledge on the relationship among the crystal structure, chemical composition and the ionic transport property in different kind of compounds. The subject matter of this thesis is to establish a

structure-property correlation between the crystal structure, chemical composition and ionic conduction in some rare earth based zircon-type mixed metal vanadates.

1.2. Background

There exist a small group of solids, which admit the macroscopic movement of ions, either cations or anions but not usually both, through their structure, leading to high values of ionic conductivity (> 10^{-4} S/cm) and negligible electronic conductivity. These kind of materials is generally termed as *'superionic conductor' (SIC) or 'fast ion conductor' (FIC) or solid electrolytes*[4-6]. In general, ionic conduction occurs at elevated temperatures and is distinguished by the fast diffusion of a considerable amount of one of the constituent species within a substantially rigid framework constituted by the other species. Examination of the last three to four decade's literatures for solid electrolytes signifies that these materials are not merely scientific curiosities, but have various technological applications ranging from miniature, lightweight lithium-ion batteries to high-capacity energy storage devices.[6] Discovery of SICs opened a vast area of research in the field of non-stoichiometry, disorder, ionic diffusion etc. with a broad range of experimental and theoretical techniques and hence keep the research on these materials as a vigorous and active field in materials science.

Michael Faraday was the first to discover the motion of mobile ions in solid electrolytes with his continuing investigations on ion conducting materials like PbF_2 and Ag_2S in a few years from 1831-1834.[2,7-11] Faraday introduced the fundamental terminology of electrochemistry, and in 1834, with the support of many results regarding the concept 'electrolyte', he classified materials into first and second types of conductors, metallic and electrolytic and the former is now recognised as electronic and the latter as ionic conductors.[8] He thus not only established the basics of electrochemistry but also of solid state ionics. At that time it was found difficult to interpret why the ionic

conductivity in Ag_2S show large enhancement with increasing temperature as it was in strong conflict to the behaviour of metallic phases. In 1851, Hittorf reached a conclusion after the investigations on the conductivity of Ag_2S and Cu_2S that an electrolytic conduction mechanism has existed in these materials during the current flow.[8,12] This marked the opening of the era of solid state ionic materials. At the end of nineteenth century Walther Nernst provide fundamental contributions to science and technology in terms of explaining the ionic transport in solids and derived the well known Nernst Equation. He also discovered that the ionic conduction in heterovalently doped zirconia at elevated temperature occurs due to the transport of oxide ions. The so- called *Nernst mass* with specifically favourable composition 85% zirconia and 15% yttria was thus discovered which he used in his *Nernst lamp* and the material is still remained as a 'high-tech' oxygen ion conductor.[7,8,11,12] Later in 1914, Tubandt and Lorenz investigated the temperature variation of conductivity of AgI and detected remarkably high values of ionic conductivity when heated beyond 147°C. At this temperature AgI undergoes a structural change from a low conducting hexagonal phase to high conducting cubic (α) phase. The superionic conductivity of α-AgI is due to the Ag^+ ions and its ionic conductivity is higher than that of the molten material.[2,7,11,13,14] This experimental study has been considered as the first methodological investigation in the exploration for high ionic conduction in solid systems. In subsequent years, different kinds of solids exhibiting remarkably high ion conductivity at their operating temperature were identified. Indeed the existence of the field of solid state ionics came in to picture in the year 1967 after the discovery of two groups of solids having fascinating conductivity (~0.1 S/cm) : Ag^+ ion conducting MAg_4I_5 (where M= Rb, K, NH_4) and Na^+ ion conducting Na-β-alumina.[2,11,14] Bradely et al. discovered the silver ion conducting solids like Ag_3SI and Ag_4MI_5 (M = Rb, K, NH_4).[13,15] Later on the discovery of these conducting solids, Takahashi and

Yamamoto[16], and Chandra et al.[17] established the use of Ag_3SI and Ag_4KI_5 in electrochemical cells. The discovery of AgI led to the innovation of a wide variety of new superionic conductors by the substitution of any one of the ionic species of AgI. Investigation on the substitution of Ag ions by divalent cations like Pb^{2+}, Cd^{2+}, Zn^{2+} and Hg^{2+} were carried out by Brightwell et al.[18-21] They reported the materials Ag_4PbI_6, Ag_2CdI_4, Ag_2ZnI_4 and Ag_2HgI_4, which were of high ionic conductivity and are stable at temperatures lower than that of α–AgI. Similar to this development in Ag ionic conductors, Takahashi and his co-workers reported a new class of materials in which the conducting species are oxide ions. In 1970s they reported the oxide ion conductivity of Bi_2O_3 and mixed bismuth oxides[22] and in 1971 that of perovskite materials.[23] Another milestone in this field was the discovery of significant oxide ion conductivity in a brownmillerite structure of $Ba_2In_2O_5$ by Goodenough.[24] After an order-disorder transition in the oxygen vacancy network, the conductivity of these materials reached to 10^{-1} S/cm from 10^{-3} S/cm at 800°C. From then variety of solid electrolytes having cationic (H^+, Li^+, Ag^+, Na^+, Cu^+ etc.), protonic and anionic (F^-, O^{2-}) conductivity have been reported. An attractive description of the development and a list of ionic conducting materials are available in the text books by Kharton[14] and Laskar and Chandra.[25]

For all-solid-state electrochemical device applications, the solid electrolytes should exhibit the following common features

- Ionic conductivity should be high (~10^{-1}-10^{-4} S/cm)
- Electronic conductivity should be negligibly small (< 10^{-8} S/cm)
- Principal charge carriers should be ions
- Ionic transference number should be close to unity
- Activation energy for ion migration should be low (< 1 eV)
- They should preferably be a single ion conducting solids[25,26]

In general, solid electrolytes exhibit conductivity values in between that of metals and insulators with same order of magnitude as those of liquid electrolytes and semiconductors. Fig. 1.1 illustrates the schematic of the electrical conductivities of typical solid electrolytes with metals, semiconductors and insulators compared at room temperature.[27,28]

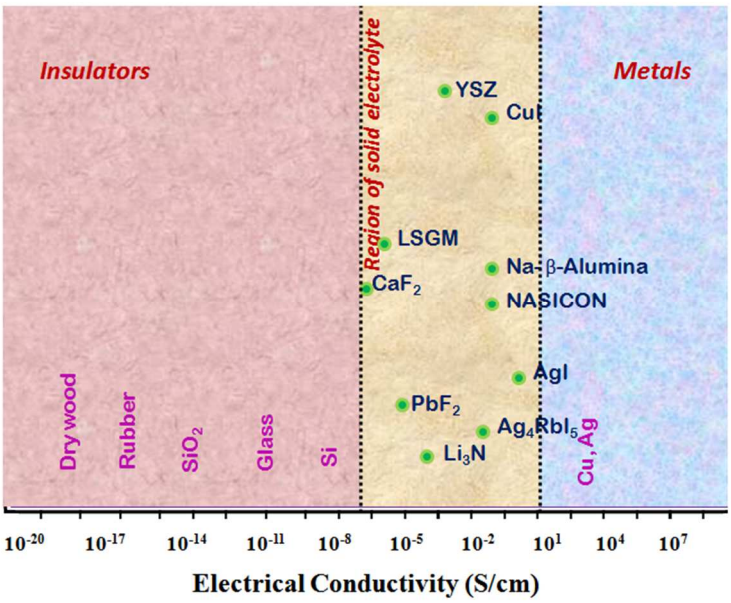

Figure 1.1: Comparison of electrical conductivity of some solid electrolytes with metals and insulators at room temperature

Some of the well-known ionic conductors proposed by different research groups are listed in Table 1.1.

Table 1.1: Examples of some ionic conducting materials and their conductivity values

Conducting ion	Compound	Conductivity (S/cm)	Temperature (°C)	Ref.
Silver (Ag^+)	α-AgI	2.6×10^{0}	147	[29]
	Ag_3SI	1.0×10^{-2}	25	"
	$Ag_6I_4WO_4$	4.7×10^{-2}	25	"
	$Ag_4I_2WO_4$	4.8×10^{-2}	27	"
	$RbAg_4I_5$	2.7×10^{-1}	24	"
	KAg_4I_4CN	1.4×10^{-1}	25	"
	$RbAg_4I_4CN$	1.8×10^{-1}	25	"
	Silver-β- alumina	6.4×10^{-3}	25	"
	$Rb_3Cu_7Cl_{10}$	3.32×10^{-2}	25	[30]
	$RbCu_3Cl_4$	2.25×10^{-1}	25	"

Copper (Cu^{+})	KCu_4I_5	6.0×10^{-1}	270	"
	β-Cu_2S	2.0×10^{-1}	400	[31]
	α-Cu_2Se	4.0×10^{0}	750	"
	$Rb_4Cu_{16}I_7Cl_3$	3.4×10^{-1}	25	[32]
	CuTeBr	1.0×10^{-5}	25	"
Lithium (Li^{+})	$LiAlCl_4$	1.4×10^{-4}	140	[33]
	$LiCdCl_4$	3.2×10^{-1}	400	"
	$LiMgCl_4$	1.4×10^{-1}	400	"
	$LiMnCl_4$	1.4×10^{-1}	400	"
	$LiFeCl_4$	6.3×10^{-2}	400	"
	$Li_{14}ZnGe_4O_{16}$	1.3×10^{-1}	300	[34]
	$Li_7La_3Zr_2O_{12}$	7.1×10^{-4}	75	"
	$Li_{1+x}Al_xTi_{2-x}(PO_4)_3$ ($x = 0.3$)	1.1×10^{-2}	100	"
	Li_3N (H-doped)	6.0×10^{-3}	25	[32]
	$Li_{3.6}Ge_{0.6}V_{0.4}O_4$	4.0×10^{-5}	18	"
Sodium (Na+)	$Na_{1+x}Zr_2Si_xP_{3-x}O_{12}$ ($0 \le x \le 3$)	1.0×10^{-4}	25	[35]
	$Na_{3.1}Zr_{1.95}Mg_{0.05}Si_2PO_{12}$	1.0×10^{-3}	25	"
	$Na_{3.1}Zr_{1.55}Si_{2.3}P_{0.7}O_{11}$	3.0×10^{-3}	25	"
	$Na_2Ni_2TeO_6$	10.1-10.8	300	[36]
	$Na_2Zn_2TeO_6$	5.1-7.0	300	"
	Na- β-Alumina	1.4×10^{-2}	25	[32]
	NASICON	1.0×10^{-1}	300	"
Potassium (K^{+})	K- β-Alumina	6.5×10^{-5}	25	[32]
	K_2O-Ga_2O_3	1.0×10^{-3}	300	[37]
Lead (Pb^{2+})	Pb- β”-Alumina	4.6×10^{-3}	40	[32]
Proton (H^{+})	$SrCe_{0.95}Yb_{0.05}O_{3-\delta}H_x$	8.0×10^{-3}	900	[32]
	$H_3PW_{12}O_{40}.29H_2O$	1.7×10^{-1}	25	"
Oxide (O^{2-})	$(Bi_{1.67}Y_{0.33})O_3$	1.0×10^{-2}	550	[32]
	$Ce_{0.8}Gd_{0.2}O_{1.9}$	5.0×10^{-2}	727	"
	ZrO_2-CaO-MgO	7.4×10^{-2}	1000	[38]
	ZrO_2-Y_2O_3	1.2×10^{-1}	1000	[38][39] [40]
Fluoride (F^{-})	α'-$PbSnF_4$	1.0×10-3	25	[41]
	β-PbF_2	$\sim10^{-6}$	20	[42]
	β-$PbSnF_4$	8.0×10^{-2}	150	"
	$KBiF_4$	1.0×10^{-4}	20	"
	CaF_2	$\sim10^{-11}$	150	"
	LaF_3	$\sim10^{-2}$	200	"
	PbF_2	1.0×10^{0}	460	[32]
	$NH_4Sn_2F_5$	1.0×10^{-1}	80	"
Chloride (Cl^{-})	$SrCl_2$	1.0×10^{-2}	642	[43]
	$RbPbCl_3$	1.0×10^{-3}	310	"

1.3. Mechanism of ionic conduction

Essential condition for ionic conductivity to occur is the presence of defects. Besides to this other conditions, like continuous paths of ions to ease vacancy movement or continuous paths of vacant interstitial sites to assist interstitial migration, also needs to satisfy.[44] Ionic conductivity occurs by the hopping of ions from one site to other through the crystal structure, so it is essential to have partial occupancy of energetically equivalent or near-equivalent sites. The conduction mechanism can be broadly classified in two (a) vacancy migration and (b) interstitial migration. In the case of vacancy migration, a number of sites that would be occupied in the defect–free structure are indeed, empty may be due to either a created Schottky defect formation or the presence of charged impurities. So it is possible for an ion adjacent to the vacancy site can able to hop to this site leaving its own site vacant. Even though, hopping is occurred by the ions not by the vacancies, this process is known as vacancy migration. In the case of interstitial migration, ions displaced from their lattice site and occur in the interstitial site (*Frenkel defect* formation). Once this happened there is a chance of ions in the interstitial sites to hop into neighbouring interstitial sites. Both of these ion migration mechanisms in the ion lattice are also known as hopping model.[32,44,45] Fig. 1.2 explains the migration mechanisms schematically. In the case of solid electrolytes, sometimes cooperative ion migration mechanism also operates. This is known as interstitialcy or knock-on mechanism. In this case an interstitial ion displaces an ion from its equilibrium lattice site. Afterwards the displaced ion can move to another interstitial site. In this way this mechanism is different from the direct interstitial mechanism.[32,45] The process of ionic conduction is thus takes place by a series of definite hops between neighbouring sites in the conduction pathways. The mobile ions are majorly located in a specific site, where they can undergo thermal vibrations. Rarely do they escape from their site and hop rapidly into an adjacent site

where they can reside for a considerable time before moving or hop back to their original site. This concept of occasional ion hop forms the basis of random walk theory and is commonly used to describe ionic conductivity semiquantitatively.[32]

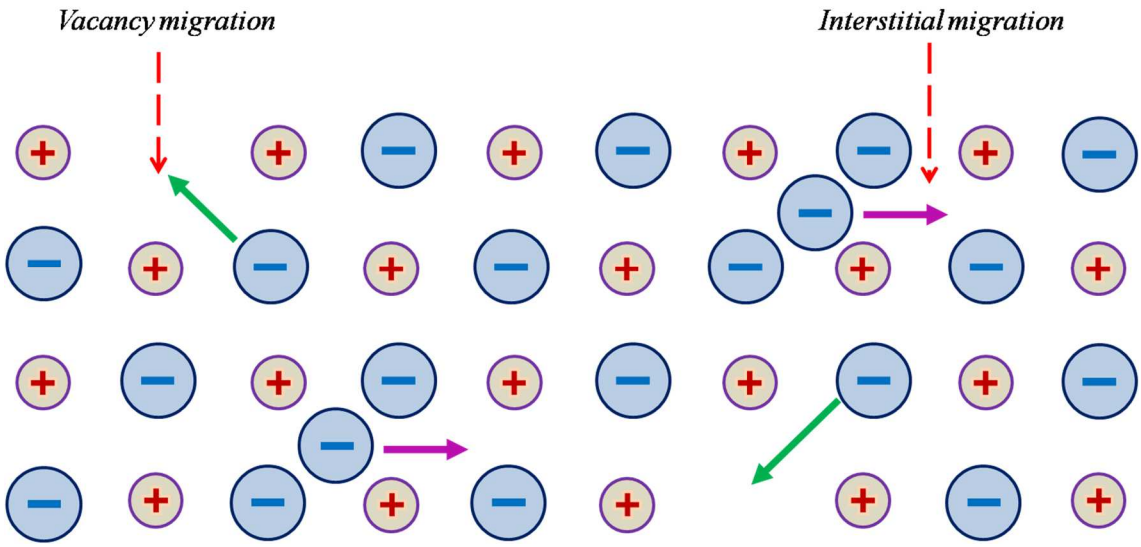

Figure 1.2: Schematic representation of the ion migration mechanisms

For a material to become an ideal solid electrolyte, it should act as an electronic insulator and a good conductor of a particular ionic species. Transport number is one of the figures of merit of this material.[46]

$$t_i = \frac{\sigma_i}{\sigma} < 1 \qquad 1.1$$

where σ_i = conductivity of the desired ionic species

σ = total conductivity viz. $\sigma_{electronic} + \sigma_{ionic}$

Generally, for a material to become a promising solid electrolyte its ionic conductivity (σ) and ionic transport number (t_i) needs to have properly high numerical values over a wide range of temperatures and partial oxygen pressures. The commonly used mechanism to explain oxygen ionic migration in oxide ion conductor materials is vacancy hopping mechanism.[26] Ionic conductivity can be expressed in terms of the product of concentration (c_i) of the mobile species (interstitial ions or vacancies) and their mobility (μ_i) and charge (q) as shown in equation 1.1.

$$\sigma_i = c_i q \mu_i \qquad 1.2$$

It is obvious that in order to increase the ionic conductivity the two parameters i.e., either mobility and/or concentration of the mobile ions can be modified.[32] The value of c_i can be improved by a number of ways: (a) by doping (b) by deviation from stoichiometry. Doping involves the addition of aliovalent (or heterovalent) impurities.[2] This includes the partial replacement of one kind of ions by ions of different formal charge. For maintaining the charge balance, either interstitial ions or vacancies must be created at the same time. If any of the vacancies or interstitials are able to migrate, exciting increase in conductivity can result. For obtaining charge balance, there are four fundamental mechanisms are present for aliovalent doping of cations as explained in fig. 1.3.[32] The stoichiometry deviation involves the reaction with gas phase results in the reduction or oxidation of the compound and creation of excess interstitials or vacancies. But at the same time this process produce electronic species also, thereby leading to mixed conduction.[2]

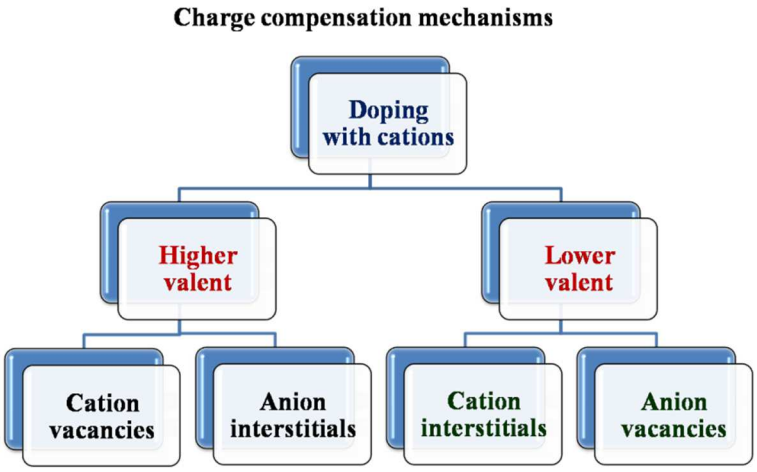

Figure 1.3: Solid solution formation by creation of vacancies/interstitials on aliovalent cation doping

Concerning the ionic conductivity in solids, some observations are made to understand its origin. The first scrutiny is that the crystal must have unoccupied sites which has to be equivalent to those occupies by the lattice oxygen ions. The next

observation is regarding the activation energy which is the minimum energy required for the ions to overcome the free energy barrier for a successful jump among the site. The activation energy involved in the process of migration of ions from one site to the unoccupied equivalent site should definitely be small viz. less than about 1 eV.[47]

The ionic conductivity is strongly temperature dependent, so an ionic conductor with negligible electronic contribution the electrical conductivity follows Arrhenius type temperature dependence as expressed in equation 1.3.

$$\sigma = \frac{\sigma_0}{T} \exp(-\frac{E_a}{kT}) \qquad 1.3$$

Where E_a = Activation energy for conduction

T = Temperature

σ_0 = pre exponential factor

k = Boltzmann constant

The pre exponential factor depends on many terms including the number of mobile ions, defect concentration, ion jump distance and frequency, structural geometry of conduction path ways etc. This is the basic equation which can be useful for studying the ionic conductivity data for oxide ion conductors.[32]

1.4. Classification of SICs:

Depending on the type of mobile charge carriers, the ionic conductors are classified generally in to three categories (i) cationic (ii) anionic (iii) protonic.

1.4.1. Cationic conductors

In the case of cationic conductors the electrical conductivity is due to the presence of positively charged ions which acts as the mobile charge carriers. Cationic conductors are further divided depending upon the kind of mobile ions. Some of the major cationic conductors include lithium ion, silver ion, sodium ion, copper ion conductors etc.

Examples of a few cationic conductors, their mobile ions and conductivity values are listed in Table 1.1.

1.4.2. Proton conductors

A proton conductor is a crystalline or amorphous material,which permits the passage of electric current through the material particularly by the movement of protons, H^+.[48] Because of the small radius of the proton, isolated H^+ ion will not exist in solids under equilibrium conditions. In the case of solid materials H^+ does not move itself rather it would bind to a molecular unit in a crystal and shift from one site to another by molecular rotation.[49] H^+ is having strong polarizing power, so it can bond covalently to one or two electronegative ions or atoms in the surrounding system. In general, there are three different bonding mechanism for proton are present

(a) The acceptor site for the H^+ may be an ion of the immobile lattice → like the formation of a hydroxo group.

(b) H^+ may be attached to a mobile ion →formation of a hydroxyl ion, OH^-

(c) H^+ may be attached to a mobile molecule →formation of H_3O^+, NH_4^+ [50]

Therefore, the present day literatures included the solid materials in which conductivity is by means of migration of polyatomic protonic species like H_3O^+, OH^- or NH_4^+ also under protonic conductors. The first investigations on the protonic conductivity of trivalent cation doped (Y, Yb, Gd and Eu) $SrCeO_3$ and $BaCeO_3$ is reported by Iwahara and collaborators.[51] Proton conductors find many technological application in the field of fuel cells, sensors, membranes, electrochromic devices etc.[52]

1.4.3. Anionic conductors

Ionic conductivity in these kind of materials occurs by the movement of negatively charged ions which acts as the mobile charge carriers. Two major classification of anionic conductors are

(i) Oxide ion (O^{2-}) conductors

(ii) Halide ion conductors (F^-, Cl^- etc.)

1.4.3.1. Fluoride ion conductors

Among the various halide ion conducting systems, F^- ion conducting system is well studied. Because of its small size, and single charge, fluoride ion conducting materials exhibits high anionic conductivty even at low temperature with negligible electronic conductivity.[53,54] Thus F^- ion conductors can find applications in many solid state electrochemical devices like fuel cells, solid state batteries, electrochromic displays, sensors etc. Temperature dependent conductivity of some representative F^- ion conducting materials in various forms are depicted in fig. 1.4.[54]

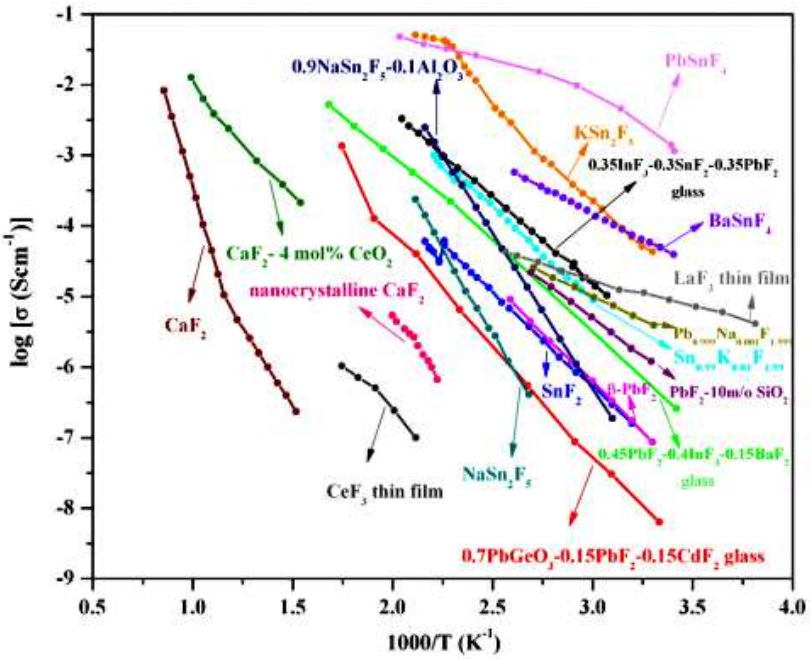

Figure 1.4: Temperature dependent conductivity plots for some representative fluoride ion conducting materials in the form of glasses, polyionic conductivity crystalline, nano-crystalline and thin films[54]

1.4.3.2. Oxide ion conductors

Oxide ion conductors are an exciting class of materials in which migration of oxide ions in an oxide lattice occurred by means of oxide ion vacancies and the electrical charge carried exclusively by oxide ions.[55] Oxide ion conduction is a peculiar property of some

solid materials and the first report on the oxide ion conductivity was by Nernst in stabilized zirconia designated as YSZ (ZrO_2 with 15 wt. % Y_2O_3) system in the turn of 19^{th} century.[56.57]

In the case of solid state oxide ion conductors, the transport of mobile ions is carried out by vacancy hopping mechanism. Accordingly, majority of the materials studied contain oxygen vacancies.[58] Considering the recognized demand for the presence of oxygen vacancies for obtaining significant oxygen ion conductivity, researchers have introduced anion vacancies into a non-oxygen-deficient structure. One approach to create anion vacancies is by doping with aliovalent cations.[59] This in turn forms extrinsic anion vacancies, as opposed to the inherent intrinsic vacancies in the structure.[58]

For a long period after the discovery of oxide ion conductivity in solid materials, their applications were restrained to peculiar domains that do not demand high current densities such as oxygen sensors due to the lack of high performance materials.[56] The ground for this restriction is that, being a doubly charged ion with a big radius (r) of 1.40 Å, oxide ion, strongly interacts with the cation network. Due to this, high mobility can only be accomplished by specific classes of materials with relevant structural features.[56,60] Many research efforts have been executed in order to reduce the operating temperature and/or to permit high current densities by improving the known materials especially zirconia based electrolytes and to come across with new phases or families of materials which can assure the increasing variety of needs. From the historical point of view, fluorite-type oxide materials consisting of quadrivalent cations (such as ZrO_2, CeO_2, ThO_2, etc.) has been most widely investigated, primarily because of the considerable research works performed on stabilized zirconia for application in solid oxide fuel cells (SOFCs).[56]

Oxide ion conductors such as Fluorite type, Pervoskite type, Rhombohedral type, Pyrochlore type, Aurivillius type, Roddlesden-Popper type and Bi_2O_3 based oxides etc. find important applications in solid-state electrochemical devices, including sensors, solid oxide fuel cells, high temperature electrolyzers, and oxygen separation membranes. A large number of literature reviews are available on the discussion of conductivity properties and the application of these systems.[56,58,59,61-63]

So far, high mobility has been observed in only a small number of structural families, such as fluorite, perovskites, pyrochlores, Bi_2O_3 based oxides etc. Some of the important classes of oxide ion conductors are shown in fig. 1.5.

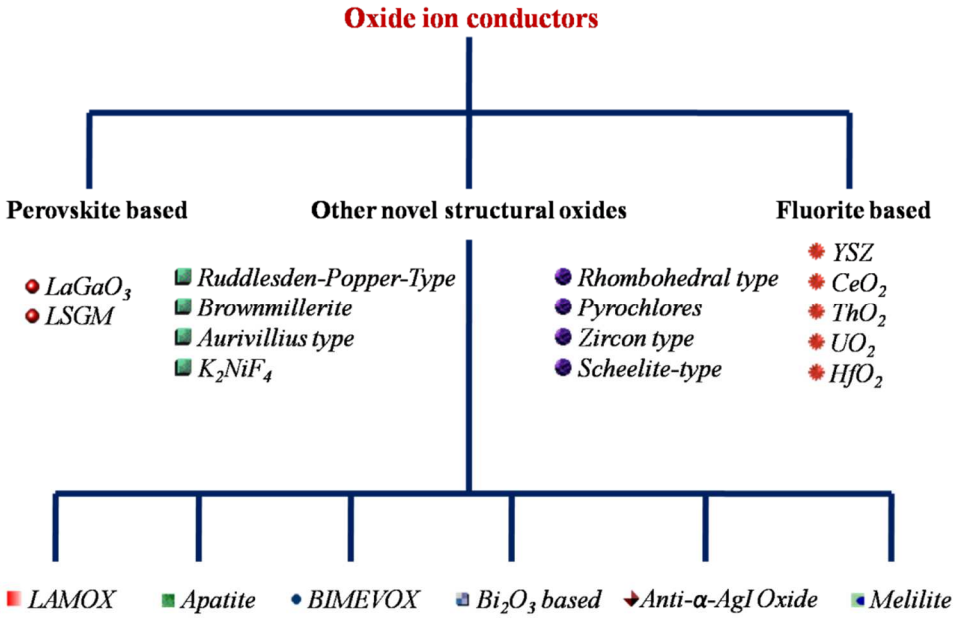

Figure 1.5: Classification of different types of oxide ion conductors

1.5. Brief introduction to Zircon structure

Zirconium silicate (zircon, $ZrSiO_4$), a common accessory mineral in nature, is considered as the prototype of zircon structure [64]. The crystal structure of Zircon was concluded independently by Vegard (1926), Binks (1926), Hassel (1926), and Wyckoff and Hendricks (1927). Later in 1958 Krstanović has refined the structure of this material.[65] Zircon-type compounds [Space group (SG): $I4_1/amd$, Z=4] with chemical

composition ABO_4 have been extensively studied because of their technologically important physical properties such as magnetic and optical properties as well as the mineralogical significance in understanding their crystal chemistry.[64,66] Ionic radii and charge combination of the A and B cations are the crucial factors in determining the diversity of crystal chemistry of ABO_4 compounds. Depending on these two parameters, these types of compounds can crystallize in scheelite (SG: $I4_1/a$), monazite (SG: $P2_1/n$), zircon (SG: $I4_1/amd$), wolframite (SG: *P2/c*), barite (SG: *Pbnm*), anhydrite (SG: *Amma*), $MnSO_4$ (SG: *Cmcm*) and $CrPO_4$ (SG: *Imma*)-type structures.[66-68] Among various ABO_4 oxides, most of the silicates, vanadates, arsenates, chromates and phosphates are isostructural with zircon; some of the phosphates and arsenates appear as polymorphs of quartz; a few of them such as germinates, molybdates, tungstates etc. prefer to crystallize in the scheelite structure whereas a number of molybdates, tungstates and tantalates choose the wolframite structure to crystallize.[69] Among the various ABO_4 oxides with trivalent A (A^{3+}) and pentavalent B (B^{5+}) cation combinations, structures associated to scheelite, monazite, zircon, $CrPO_4$ and $MnSO_4$ are recognised either at ambient or non-ambient temperature pressure conditions. Though, the trivalent cation A^{3+} belongs to any one of the rare earth ions i. e. La-Lu, Y and Sc, monazite and zircon type structures are the only crystal structures recognized for vanadates and phosphates. However, most of the heavier lanthanide vanadates and phosphates crystallize in tetragonal zircon structure.[66]

The tetragonal zircon type structure consists of isolated BO_4 tetrahedra. The A atom is coordinated by eight O atom that delineate a triangular dodecahedron (bisdisphenoids). The AO_8 dodecahedron in zircon can be defined as two interpenetrating AO_4 tetrahedra: one elongated along [001] and the other one is compressed.[70] The principal structural unit in zircon can be described in terms of chains of alternating BO_4 and AO_8 polyhedra extending parallel to the c-axis. The chains are joined laterally by edge-sharing AO_8

dodecahedra. Four edges of each dodecahedron share with adjacent dodecahedra and two edges with neighbouring tetrahedral.[71] Fig. 1.6 shows a representation of zircon structure of ABO_4 type compound. Zircon is having a relatively open structure with small voids between the BO_4 tetrahedra and AO_8 dodecahedra and open channels parallel to [001]. These kinds of voids can be possible interstitial site which can have the ability to incorporate impurities. These sites can hold interstitial ions without much structural strain.[70]

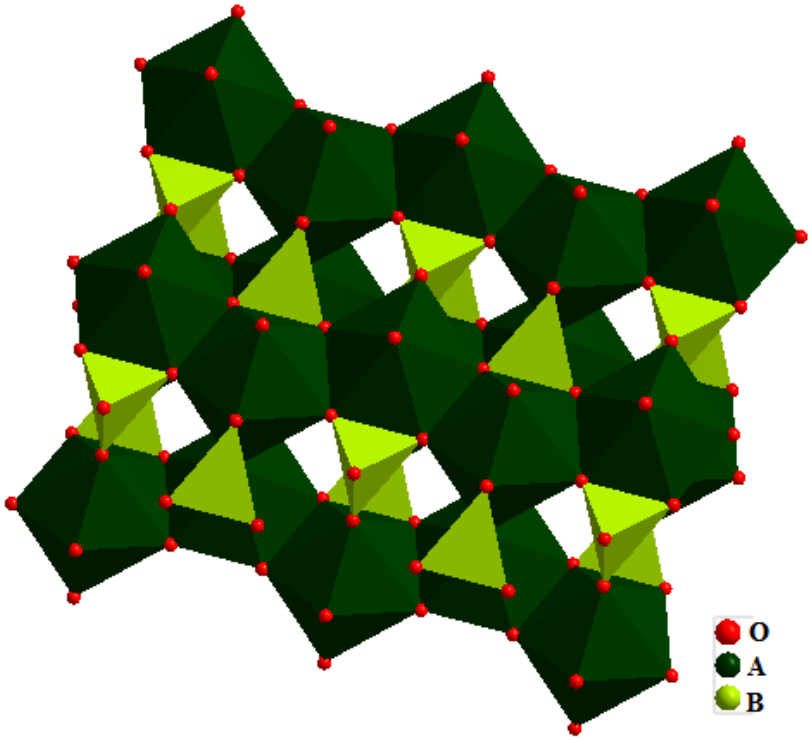

Figure 1.6: Zircon structure of ABO_4 compounds

Materials from the family of lanthanide orthovanadates ($LnVO_4$), mineral name wakefeldite, have recently been appeared as promising class of materials due to their unique physiochemical and optical properties. Owing to these properties, these materials find applications in the various fields such as components of catalysts, lasers, cathodoluminescent materials, Raman lasers, low-loss optical planar waveguide, thermophosphors, scintillators etc.[71,72] High temperature electrochemical applications of rare earth orthovanadates due to their sufficient stability under operating conditions have

been reported by Tsipis.[73] Generally, $LnVO_4$ compounds show polymorphism and may crystallize in two common structural forms; tetragonal (t-) zircon ($ZrSiO_4$) and monoclinic (m-) monazite ($CePO_4$).[74-78] Both of these structural forms are related in such ways that lower symmetry monoclinic structure can be formed by the introduction of ninth oxygen into the A-site cation coordination sphere of the zircon structure.[78] At ambient pressure and temperature larger lanthanide ion prefer the crystallization in monazite-type structure, while smaller lanthanide ions favor zircon-type structure.[79]

In zircon phase of orthovanadates, the V-O distance remains constant within the experimental error and there exists four long and four short A-O distances. One set of A-O contact is of long bond distance which is associated with the elongated AO_4 tetrahedra and the other set of short bond distance related to the compressed AO_4 tetrahedra.[70,80] Conceptually, zircon structure can be imagined as the chains of alternating edge-sharing AO_8 bisdisphenoids and VO_4 tetrahedra as isolated chains of edge-sharing VO_4 and elongated AO_4 tetrahedra, both being tetragonal disphenoids extending parallel to c.[70,81] The zircon structure can be analysed as a superstructure of rutile (TiO_2) because in the zircon structure each of the cations is surrounded by two adjacent cations of the other kind along the c- axis by eight (4+4) cations at a larger distance thus forming a body centred tetragonal subshell which is a typical cation arrangement of rutile structure.[80]

Detailed crystal structure refinement of most of rare earth vanadates with zircon structure were carried out by Chakoumakos et al.[81] They reported that depending upon the size of the Ln atom, viz. as the Ln atom size decreases V-O distance showed a systematic shortening and the average V-O bond length is found to be around 1.709(2) Å for all the studied orthovanadates. The Ln ion atomic number has a strong influence on the oxygen positional parameters, the cell dimensions and the Ln-O distance. The O---O edge shared with the bisdisphenoids are about 8% shorter than the polyhedral edges which are not

shared, results in a slightly elongated *VO_4* tetrahedron. The two sets of Ln-O distance of *LnO_8* bisdisphenoids originating from the four long bonds to the edges shared with the tetrahedral and the four short bonds to the edges shared with other bisdisphenoids. In $LnVO_4$ system the lanthanide metal atom and vanadium atoms are placed at 4a and 4b positions respectively and oxygen is at 16h position with (0, y, z) coordinates.[82]

1.5.1. Literature survey of zircon type ionic conductors

In the last ten years, $LnVO_4$ materials have emerged as prospective materials for electrochemical applications such as Li ion batteries[83,84] and SOFCs.[85-91] One notable benefit for $LnVO_4$-derived components of SOFC anodes is their good resistance to carbon deposition and sulphur-containing impurities.[87,91-93] Scrutiny of available literature data on electrical characterization shows that the most studied system among $LnVO_4$ series is cerium orthovanadate $CeVO_4$. Many researchers are already visible in the synthesis and exploration of electrical conductivity of $CeVO_4$ based materials.[79,88,90,94-96] In 1995 Rao and Palanna[97] reported the electrical and thermal behaviours of $CeVO_4$ for the first time. According to them, however $CeVO_4$ behaves as an insulator both in pure and stoichiometric compositions; it exhibits a p-type semiconductor behaviour in a temperature range of 30°C to 800°C due to the deviation from cation stoichiometry. An explanation given to account for the p-type conduction in the lattice was given by the coexistence of a few numbers of Ce^{4+} ions among the lattice sites of Ce^{3+} ions and therefore the conduction was occurring via thermally activated motions of holes on equivalent Ce^{3+} sites. Thus the existence of Ce^{4+} ions in the place of Ce^{3+} sites leads to the formation of a few vacant cationic sites which in turn results in a p-type semiconduction. Watanabe et al.[95] reported a detailed discussion on the electrical conductivity of $CeVO_4$, $Ce_{1-x}M_xVO_{4-0.5x}$ (M= Ca, Sr and Pb) and $Ce_{1-y}Bi_yVO_4$ systems. Based on the Seebeck effect data, the compound $CeVO_4$ was demonstrated as a p-type

semiconductor. The electrical conductivity as well as the number of oxygen vacancies increased with the incorporation of divalent cations such as Ca, Sr and Pb in to the Cerium sublattice. The conductivity of Bi doped $CeVO_4$ is found to be slightly higher than that of parent $CeVO_4$ for $y<0.5$, and lower with $y\geq0.5$. Increased conductivity for $CeVO_4$ system was reported with A-site substitution by alkaline earth ions like Ca and Sr.[88,90] Oxygen ion conductivity of the substituted $CeVO_4$ is essentially independent of A-site dopant concentration Acceptor-type substitution is compensated by increasing average oxidation state of cerium ions which in turn induces higher electronic conductivity. The higher value of conductivity is contributed by hopping of electron-holes between Ce^{4+}/Ce^{3+} cations. Ionic transport was explained in terms of interstitial oxygen diffusion mechanism. Contrary to the ionic conduction, divalent cations have influence on the p-type electronic conductivity and Seebeck coefficient of the vanadates. Later reports by Petit et al.[79,94] on Sr^{2+} and Ca^{2+} substituted $CeVO_4$ also confirmed that the alkaline earth metal cations increases the electrical conductivity in $Ce_{1-x}A_xVO_4$(A = Ca, Sr) system within the solid solution formation limits. In both cases the conductivity of the doped $CeVO_4$ is higher in air but have a lower value in a reducing atmosphere comparing to the pure $CeVO_4$ whereas the latter shows an increased conductivity in reduced atmosphere. The improvement in conductivity in air for the doped samples is independent of dopant level.

According to the available literatures the data on electrical properties of other $LnVO_4$ orthovanadates and their derivatives are very scant. Gaur and Lal[98-100] studied the electrical transport data for the $LnVO_4$ (Ln = La-Yb) series using pressed pellets for conductivity measurements. From their results they concluded that $LnVO_4$ systems are essentially electronic semiconductors. For all the studied compositions, the Arrhenius plots of conductivity showed unusual behavior having several variations of slope and a

sharp enhancement of conductivity in the temperature range between just about 600°C and 850°C, in vicinity of melting point of vanadium pentoxide, V_2O_5 (T_{melt} = 681°C). So it is possible to imagine that these data therefore may be strongly influenced by the presence of V_2O_5 impurity, its melting and evaporation, and accompanying dimensional changes of the samples on temperature cycling.

Electrical transport properties of $PrVO_4$ single crystals were reported by Yadava et al.[101] for the first time. They measured the electrical conductivity of this material perpendicular to the crystallographic *c* axis in a temperature range of 25°C to 730°C. In the lower temperature region from 25°-430°C the material showed an extrinsic conduction and above 430°C large polarons are responsible for electrical conduction. Huse et al.[102] reported the electrical properties of undoped and Ca doped $LaVO_4$. Acceptor-type substitution by Ca in a monazite-type $La_{1-x}Ca_xVO_4$ resulted in approximately one order of magnitude increase in the electrical conductivity compared with the undoped $LaVO_4$, but the solid solubility of calcium in La sublattice is very limited i.e., < 5 at. %. $La_{0.99}Ca_{0.01}VO_4$ was reported to be a pure ionic conductor in oxidizing atmosphere and in the measured temperature range from 300°-1100°C. Proton conductivity dominating at low temperatures under wet conditions reaching a maximum conductivity of 5×10^{-5} S/cm at ~900°C, and oxide ions act as the dominating charge carriers at high temperatures.

1.6. Applications of ionic conductors

Oxide ion conductors are an exciting class of materials having technical importance in a wide range of application domains. Oxide ion conductors are primarily used as a potential candidate for fuel cells of the solid oxide type (SOFCs)[8,103], oxygen pumps[104,105], oxygen gas sensors[3,106], ceramic membranes for oxygen separation[107,108],

partial oxidation of light hydrocarbons[109,110] and as catalysts[111] etc. A brief description of some of the important applications is highlighted in the later sections of this chapter.

For commercial applications solid electrolytes needs to satisfy the following fundamental requirements [112]

a. The material offers an impermeable barrier to gases and liquids, but permits the passage of one or more kinds of ions through its lattice when a tendency for such migration exists. The potential gradient created either by an applied voltage or by a chemical potential gradient of the migrating ions will induce this tendency.
b. The material permits the measurement of the difference of chemical potential of the migrating species on either side of it in terms of e. m. f. in an appropriately constituted cell.
c. The materials should be stable and resistant to high temperature corrosion.

1.6.1. Oxygen sensors

An oxygen sensor or oxygen probe or oxygen meter is an electrochemical device which is used to determine the proportions of oxygen ($p(O_2)$) in gas mixtures or liquid metals and alloys being analysed**.** It consists of a solid oxide electrolyte, a reference electrode (a gas mixture or two-phase solid mixture having a known chemical potential of oxygen) and an unknown electrode**.**[113]

Oxygen sensor is an oxygen concentration cell of the following type

reference gas, Pt | solid oxide electrolyte | Pt, sample gas

$p(O_2)^\circ, \mu_{O2^\circ}$ (O^{2-}) $p(O_2), \mu_{O2}$

A simple schematic representation of the same is given in fig. 1.7.

The chemical potential of the unknown electrode (μ) can be determined directly from the measured electromotive force (e.m.f) of the cell using the following well known equation by Nernst[112]

$$E = -\frac{(\mu_{O_2} - \mu^{o}_{O_2})}{4F} = \frac{RT}{4F}\left(\frac{ln\, p_{O_2}}{ln p^{o}_{O_2}}\right) \qquad 1.4$$

F → Faraday constant

μ → chemical potential

p → partial pressure

R → Universal gas constant

T → absolute temperature

Superscript ° refers to the reference gas.

By determining F, the unknown pressure p_{O2} may be calculated if the partial pressure of oxygen in the reference gas $p(O_2)°$ is known. Concentration of oxygen in moles per unit volume can be calculated from the equation[112]

$$p = \left(\frac{n}{v}\right) RT \qquad 1.5$$

n → no. moles of oxygen

v → total volume of the gas

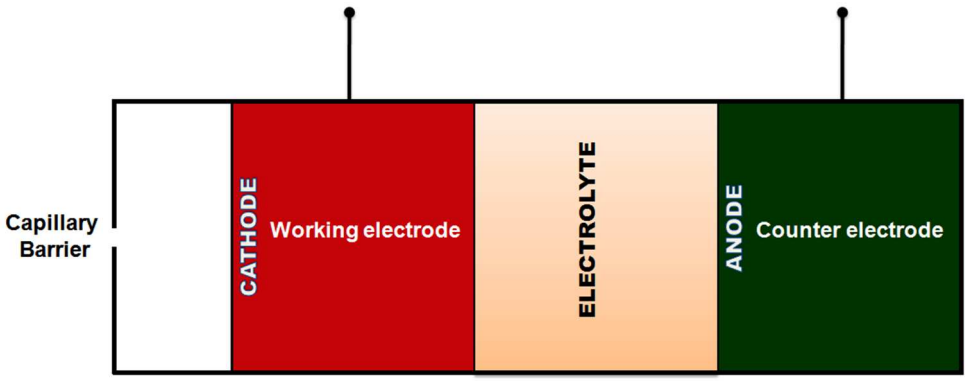

Figure 1.7: Simplified schematic representation of an oxygen sensor

Depending upon on two principles different kinds of sensors have been developed based on solid electrolytes. These are

(a) Potentiometric sensors based on the chemical potential difference across the solid electrolyte

(b) Amperometric sensors based on the charge passed through the electrolyte.

1.6.1.1. Potentiometric sensors

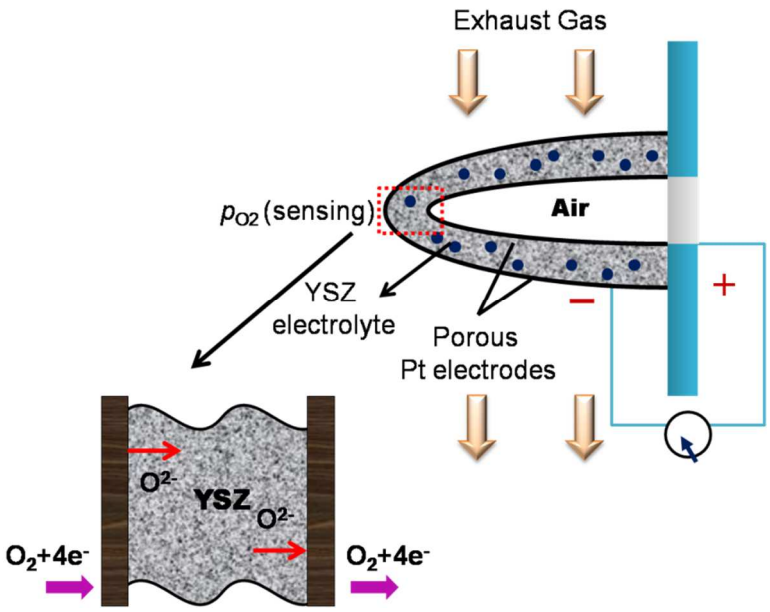

Figure 1.8: Schematic diagram of potentiometric oxygen sensor

In a potentiometric gas sensor, determination of the concentration or partial pressure of oxygen is carried out by the equilibrium potential measurement on solid electrolyte –electrode cells using Nernst equation.[1,114] Even for low levels (ppm) of oxygen also these kinds of sensors offer accurate, stable and reproducible measurements In general these high temperature solid state sensors use oxygen ion conducting materials as electrolytes.[114] Commonly used electrolyte is YSZ due to its high oxide ion conductivity and stability even at harsh environments. The most important applications for the auto exhaust sensor includes the control of Air to Fuel ratio (A/F) in automobile exhaust gases and industrial combustions.[1,3,114] Sensor output arises from the combined effect of chemical and electrical processes. When the device is exposed to the test gas environment, adsorption of oxygen molecules onto the porous electrodes occur leading to the formation of atomic oxygen. Which in turn diffuse in to the boundary of the electrode, electrolyte and the gas called the 'triple phase boundary' (TPB) where electron transfer from the electrode takes place leading to the formation of oxide ions. For assisting these

processes the electrodes needs to be a good catalyst for oxidation and reduction of oxygen, required to have a porous microstructure to clear sufficient TBPs and the electrolytes must be good conductor of oxide ions at the operating temperature of the device.[3]

1.6.1.2. Amperometric sensor

By applying an external potential across the electrolyte, electrochemical pumping of chemical species from one chamber to another is possible. The resulting current flow through the cell provides the measure of oxygen concentration and is called limiting current amperometric sensors. These sensors do not require reference oxygen column since the diffusion or interfacial phenomena at the electrode is linearly depend upon the partial pressure of the gas constituent. Amperometric sensors are mainly used to measure dissolved oxygen in liquids. They are also find application in lean burn engines where the $p(O_2)$ does not vary strongly with A/F ratio compared to the engines operating at or near the Stoichiometric A/F ratio.[1,114] In such condition the logarithmic dependence of $p(O_2)$ as in the case of potentiometric sensors not work good, a linear dependence of oxygen concentration as in amperometric sensors provide better results.[1,3,114]

Fig.1. 9 represents an amperometric oxygen sensor

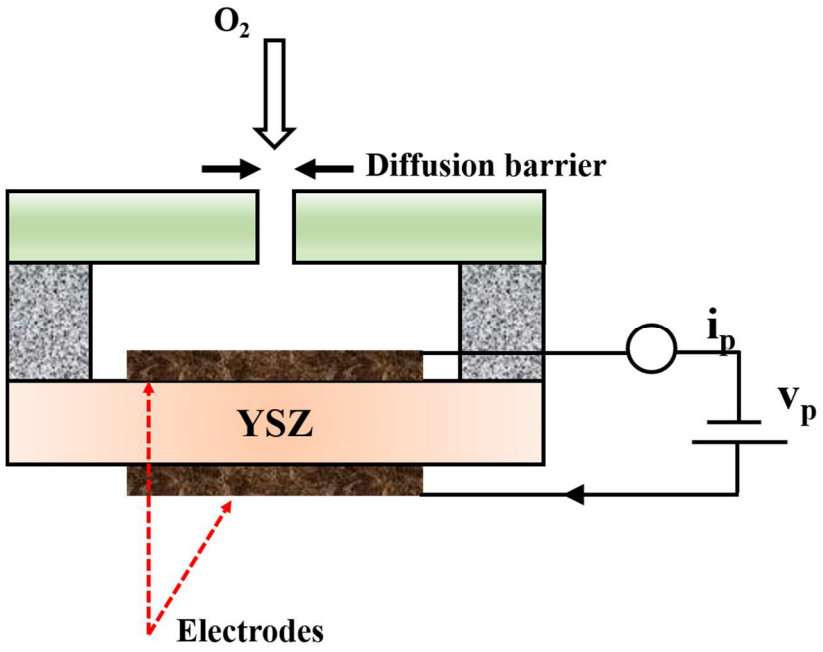

Figure 1.9: Amperometric oxygen sensor based on YSZ electrolyte

1.6.2. Oxygen Pumps

Oxygen pumps or solid electrolyte oxygen separation (SEOS) device is an electrochemical device which is used to produce oxygen from air without using water. In an oxygen pump electrical potential is utilized to pass separation and the device requires an electrolyte which is oxygen ion conducting only. Ceramic membranes based on oxygen pump systems comprised of two main advantages over the conventional technologies such as

a. An oxygen transport membrane based on oxygen pump permits the continuous operation and
b. Air can combine with the pure oxygen streams produced by the pump and thus it can form varying levels of oxygen enriched gas.[115]

According to the operating principle of oxygen pump, application of voltage V_{appl} across the electrodes promotes the conduction of oxide ions from cathode to anode. At high temperature, O_2 in cathode get reduced to oxide ions by receiving electrons from the external circuit. The oxide ion conducting electrolyte then acts as a medium for the

transport of O^{2-} ions from cathode to anode. At anode, by losing electrons O^{2-} again form O_2 molecule.

$$O_2 + 4e^- \rightarrow 2O^{2-}$$ (Cathode)

$$2O^{2-} \rightarrow O_2 + 4e^-$$ (Anode)

The applied voltage drives the movement of electrons between the electrodes via external circuit and hence the current can be produced. Thus the oxygen pumps operating in such a way, by applying continuous current on to the cathode/electrolyte/anode system, movement of oxygen from cathode to anode via the solid electrolyte occurs.[116] According to Faraday's law this current correspond to an oxygen flux of I/4F moles of O_2 s^{-1} (where I is the current density and F is the Faraday's constant) transported through the solid electrolyte.[104,115] By adjusting the applied voltage or current to the pump, in principle, one can accurately control the oxygen removal rate, thus offer a distinct way to attain a high precise values of oxygen partial pressure in either closed or open system. Oxygen pumps can be useful for removing oxygen from ambient environments, both liquid and gaseous, deoxidation of molten metals, and for the removal of oxygen from a flowing gas stream or from a closed system.[117]

1.6.3. Oxygen permeable membranes

Dense ceramic oxygen permeable membranes (OPMs) with mixed oxide and electronic conductivity have become of great interest for high temperature electrochemical applications including oxygen production from air or other oxygen containing atmospheres, separating high-purity oxygen from air or other oxygen containing gas mixtures, partial oxidation of methane and other light hydrocarbons, waste reduction and recovery, sensors, and as membrane reactor for the chemical upgrading in efficient, clean and economical means.[107,109,118,119] Difference of oxygen partial pressure on the two sides of the membrane will act as the driving force for the separation of

oxygen.[120] Use of pure oxide ion conducting membrane instead of a mixed conducting membrane offer better control over the intensity of oxygen removed or generated via the control of the level of current passed. Pure oxide ion conducting ceramic membrane technology is useful for the production of oxygen, removal of oxygen in gas streams and enclosures and for the control of oxygen level to generate calibration gases.[121]

1.6.4. Solid Oxide Fuel Cells (SOFCs)

One of the major challenges for the scientist and engineers is the production of energy by means of a clean, efficient and environmentally friendly manner. Solid Oxide Fuel Cells (SOFCs) are electrochemical devices that can offer considerable advantages over the conventional power generation technologies. Fuel cells are the devices which can convert chemical energy of a fuel gas in to electrical power without the need of direct combustion and thus they are efficient and environmentally clean.[122,123] SOFCs find high power applications in various fields such as full scale industrial stations and large-scale electricity generating stations, motor vehicles etc. compared to the other fuel cell technologies, SOFCs has some differences

1. SOFCs are composed of all-solid state materials
2. SOFCs are capable operating at high temperatures (~1000°C)
3. Since the components of SOFCs are all-solid state materials, there is no basic restriction on the cell configuration.[122]

The basic unit cell of SOFC consists of four main ceramic components

(a) Anode (b) cathode (c) solid electrolyte and (d) interconnect

A schematic of the SOFC and its working is illustrated in fig.1. 10.

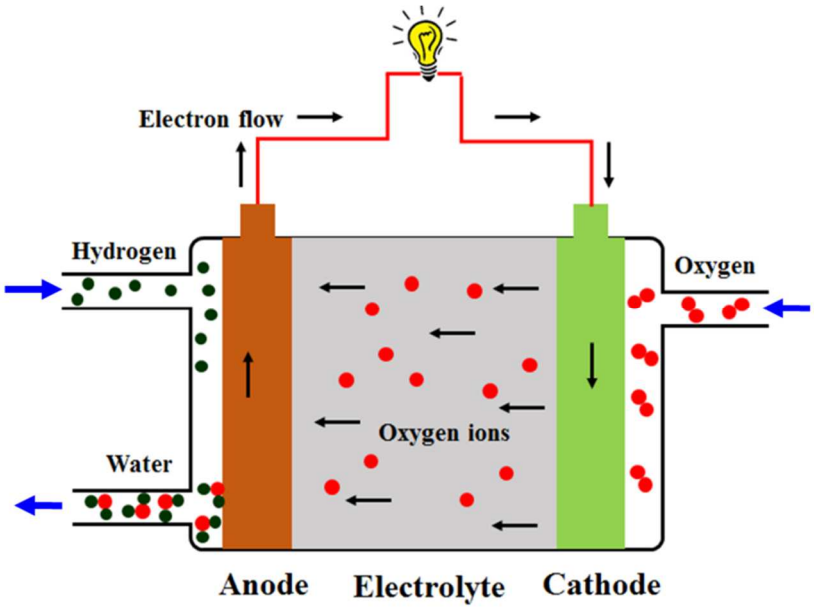

Figure 1.10: Working of an SOFC

Elementary steps involved in the production of electric power can be explained as follows: the fuel is fed into the anode of the fuel cell and the oxidant gas, usually air, is supplied to the cathode. The solid electrolyte which is either an oxide ion conducting or proton conducting material is sandwiched in between the two electrodes. At the anode the fuel will undergo oxidation reaction and release electrons to the external circuit.

Anode reaction: $H_2 + O^{2-} \rightarrow H_2O + 2e^-$

At the cathode, the oxidant accepts these electrons from the external circuit and gets reduced to oxide ions.

Cathode reaction: $\frac{1}{2}O_2 + 2e^- \rightarrow O^{2-}$

These oxide ions can diffuse through the solid electrolyte to the anode where it will electrochemically oxidize the fuel. In order to fulfil this reaction, the cathode must be able to dissociate oxygen and to be electronically conductive. Presence of electrical connections between the two electrons permits the flow of electrons from anode to cathode, where a continuous supply of oxide ions for the electrolyte is maintained, and

oxide ions can move from cathode to anode via electrolyte, maintaining the overall electrical charge balance.

Overall cell reaction: $H_2 + \frac{1}{2}O_2 \rightarrow H_2O$

Thus, the flow of electrons through the external circuits from anode to cathode produces electric power and the cycle repeats as those electrons enters the cathode material again. The only by-product obtained by the cell reaction is water and heat. As long as the reactants are available to the electrodes, the cell will produce current under the cell operating conditions.[122,124]

The electrochemical reduction of oxygen occurs at the SOFC cathode. In order to accomplish this, the cathode should possess the following requirements (a) it should have sufficient porosity to permit the diffusion of oxygen (b) matching thermal expansion coefficient with the other components under the operating conditions (c) chemically compatible with the other contacting components under the operating temperature (d) high catalytic activity for the reduction reaction (e) high electronic and oxide ion conductivity (f) chemical and microstructural stability under oxidizing atmospheres during the operation and fabrication (g) adhesion to electrolyte surface. It is usually considered that the electrochemical reaction occurs at the triple phase boundary (TBP), i.e., the site where oxide ion conductor, electronic conductor and the gas phase are in contact (fig 1.11). The cathode polarization losses connected to the reduction reaction is generally responsible for the considerable loss of voltages in SOFC. Appropriate cathode material selection is required to minimize this problem. The choice of cathode material is dependent on the electrolyte material. Commonly used cathode material is Sr doped $LaMnO_3$ (LSM).[8,123-125]

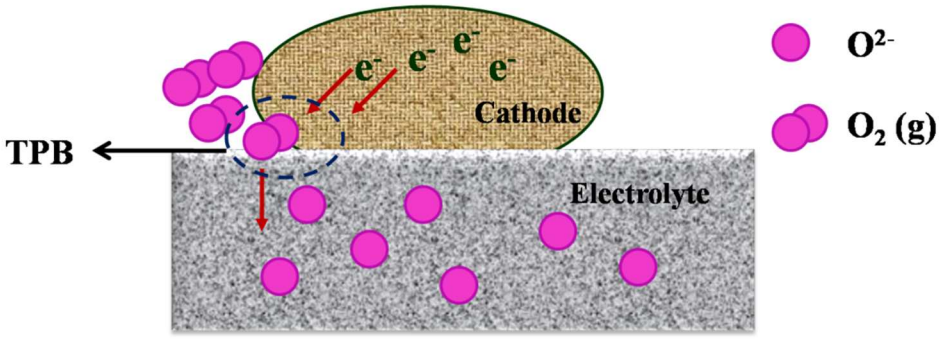

Figure 1.11:. Schematic diagram of triple phase boundary (TPB)

An electrolyte is one of the major components of SOFC and is responsible for the transportation of ions between the electrodes, for the separation of the reacting gaseous species, for restricting the internal electronic conduction, and to compel the electrons to flow through the external circuits.[8] Current researches are mainly focused on SOFCs with oxide ion conducting electrolytes instead of proton conducting electrolytes. In the case of oxide ion conducting electrolytes the conduction occurs by means of oxide ions from the air electrode to the fuel electrode. The transport of ions is a result of the thermally activated hopping of O^{2-} ions from one crystal lattice site to the neighbouring site. The energy required for this ion migration must be small.[125]

At present a lot of oxide ion conducting material is reported, only few of them are suitable for SOFC applications. For satisfactory performance as a solid electrolyte, the material should meet multifaceted property criteria that limit the choice of the material. This includes

(a) For an optimum cell performance, the electrolyte material must be free of porosity so that it will restrict the gases to permeate from one side of the electrolyte to the other side

(b) The material should be thermodynamic stable over a wide range of temperature and oxygen partial pressure.

(c) The material should have high oxide ion conductivity (> 10^{-2} S/cm) at the cell operating conditions

(d) The electronic conductivity of the material should be negligibly small under the cell operating temperature

(e) The material should have good chemical and mechanical compatibility with the electrodes in order to reduce the interfacial resistances and to avoid the formation of blocking interface phases.

(f) Coefficient of thermal expansion (CTE) between the electrodes, electrolytes and interconnects should be compatible in order to avoid cracking during cell operation.

(g) The material should be stable in both oxidizing and reducing environments

(h) Low cost of starting material and should be economic for fabrication [8,125,126]

Due to these requirements, the choice of electrolytes is limited to zirconia electrolytes, doped ceria, doped $LaGaO_3$ based perovskites and Bi_2O_3. The mostly studied and developed electrolytes for high temperature SOFC are stabilized zirconia especially yttria stabilized zirconia (YSZ).[8,123,125]

The primary role of an anode material in the SOFC is to act as a site for the electrochemical oxidation of the fuel and to transfer charge to the conducting contact.[123-125] The general requirements for an anode material include (a) high electronic conductivity under the cell operating conditions (b) matching CTE with adjoin cell components (c) good chemical and thermal stability during fabrication and operation of the fuel cell (d) chemical compatibility with electrolytes and interconnects under reducing atmosphere and under the operating conditions (e) admirable catalytic activity towards the oxidation of fuels (f) tolerance to coke deposition and sulphur poisoning and reoxidation (g) sufficient porosity for the fuel supply and removal of reaction product (h)

adequate mechanical strength and flexibility, ease of fabrication into required microstructures and low cost (i) good ionic and electronic conductive phases (j) larger TPBs.[8,123,125] Ionic conductivity allows the anode to extend active reaction sites for fuel oxidation from a broader region of TPBs to anode surface, and electronic conductivity is essential to transmit the electrons resulting from the electrode reaction out into the external circuit.[8] Ni-YSZ cermet is the commonly used anode material in conventional SOFC designs using YSZ as electrolytes and H_2 gas or mixture of CO and H_2 gas as fuel.[8,123,125]

In SOFCs, interconnects are generally used for making electrical contact between the cells and for the gas separation within the cell stack. Major requirement for this material includes (a) high thermal and electrical conductivity (b) manageable CTE mismatch with other components of the cell (c) high mechanical strength and phase stability under the cell operating conditions (d) it should be impermeable to gas (e) compatible with the other components of the cell and has to be stable with respect to the oxidising and reducing gases (f) low cost and ease of fabrication (g) high electronic and low ionic conductivities.

For high temperature operations, suitable material which satisfies the above mentioned criteria is doped rare earth chromites such as perovskite lanthanum chromite ($LaCrO_3$) doped with Sr and Ca.[8,123]

1.7. Scope of the present work

Mixed metal oxides find applications in several energy related fields, electrode materials, electrolytes, superconductors etc. In this context rare earth based mixed metal oxides show superior properties. Therefore the present work envisages preparation of novel mixed metal vanadates having tetragonal zircon structure. The preparative methods adopted for the current study are solid state synthesis and combustion synthesis. The effect of alkaline earth metal such as magnesium and monovalent metals like lithium and silver on the electrical properties of well known zircon-type rare earth orthovanadates is the main focus of the study. These materials were synthesized and their structural and microstructural characterization was done. Influence of Mg cations on the conducting properties of the materials compared with the parent materials was carried out in detail. Structure-property correlation of the prepared materials was studied.

1.8. References

[1] S. Kasap, P. Capper, Springer Handbook of Electronic and Photonic Materials, Springer, 2006.

[2] P. Knauth, H. L. Tuller, Solid-State Ionics : Roots , Status , and Future Prospects, *J. Am. Ceram. Soc.* 85 (2002) 1654–1680.

[3] R.V. Kumar, H. Iwahara, Handbook on the physics and chemistry of rare earths, Elsevier, 2000

[4] A. R. West, Solid electrolytes and mixed ionic-electronic conductors: An applications overview, *J. Mater. Chem*. 1 (1991) 157–162.

[5] P. P. Kumar, S. Yashonath, Ionic conduction in the solid state, *J. Chem. Sci.* 118 (2006) 135–154.

[6] D. A. Keen, Disordering phenomena in superionic conductors, *J. Phys.: Condens. Matter*. 14 (2002) R819–R857.

[7] K. Funke, Solid State Ionics: from Michael Faraday to green energy — the European dimension, *Sci. Technol. Adv. Mater.* 14 (2013) 043502.

[8] S. C. Singhal, K. Kendall, High temperature solid oxide fuel cells: Fundamentals, design and applications, Elsevier, 2002.

[9] R. Collongues, A. Kahn, D. Michel, Superionic conducting oxides, *Ann. Rev. Mater. Sci.* 9 (1979) 123–150.

[10] H. Schulz, The physics of superionic conductors and electrode materials, Plenum Press, 1983.

[11] H. Mehrer, Diffusion in solids: Fundamentals, methods, materials, diffusion-controlled processes, Springer, 2007.

[12] H. Möbius, On the history of solid electrolyte fuel cells, *J. Solid State Electrochem.* 1 (1997) 2–16.

[13] T. Takahashi, Early history of solid state ionics, *Mat. Res. Soc. Symp. Proc.* 135 (1989) 3–9.

[14] V. V. Kharton, Handbook of solid state electrochemistry: Fundamentals, methodologies, applications, Volume 1, Wiley, 2009.

[15] J. N. Bradley, P. D. Greene, Potassium Iodide+silver iodide phase diagram: High ionic conductivity of KAg_4I_5, *Trans. Faraday Soc.* 62 (1966) 2069–2075.

[16] T. Takahashi, O. Yamamoto, The $Ag/Ag_3SI/I_2$ solid-electrolyte cell, *Electrochim. Acta.* 11 (1966) 779–789.

[17] S. Chandra, H. B. Lal, K. Shahi, An electrochemical cell with solid , super-ionic Ag_4KI_5 as the electrolyte, *J. Phys.: D Appl. Phys.* 7 (1974) 194–198.

[18] J. W. Brightwell, C. N. Buckley, B. Ray, Electrical and phase behaviour of the system AgI-PbI_2, *J. Solid State Commun*. 42 (1982) 715–716.

[19] J. W. Brightwell, C. N. Buckley, G. Foxton, L. S. Miller, B. Ray, Electrical conductivity and equilibrium diagram studies in the AgI-ZnI_2 system, *J. Mater. Sci. Lett.* 1 (1982) 429–431.

[20] J. W. Brightwell, C. N. Buckley, R. C. Hollyoak, B. Ray, Structural and phase equilibrium comparisons of Ag_2Hgl_4 with Ag_2CdI_4 and Ag_2ZnI_4, *J. Mater. Sci. Lett.* 3 (1984) 443–446.

[21] J. W. Brightwell, C. N. Buckley, L. S. Miller, B. Ray, Structural studies and electrical conductivity versus temperature measurements in mixed silver-lead iodide phases, *Solid State Ionics*. 9 & 10 (1983) 1169–1174.

[22] R. N. Vannier, J. C. Boivin, G. Mairesse, Supermaterials, Kluwer Academic, 2000.

[23] T. Takahashi, H. Iwahara, Ionic conduction in perovskite -type oxide solid solution and its application to the solid electrolyte fuel cell, *Energy Convers*. 11 (1971) 105–111.

[24] J. B. Goodenough, J. E. Diaz, Y. S. Chen, Oxide-ion conduction in $Ba_2In_2O_5$ and Ba_3 In_2MO_8 (M = Ce, Hf, or Zr), *Solid State Ionics*. 44 (1990) 21-31.

[25] A. L. Laskar, S. Chandra, Superionic solids and solid electrolytes Recent Trends, Academic Press, 1989.

[26] P. Hagenmuller, W. V. Gool, Solid Electrolytes: General principles, characterization, materials, applications, Academic Press, 1978.

[27] M. Nunez, New developments in electrochemistry research, Nova Science, 2005.

[28] V. Thangadurai, W. Weppner, Recent progress in solid oxide and lithium ion conducting electrolytes research, *Ionics* 12 (2006) 81–92.

[29] T. Takahashi, Handbook of solid state batteries and capacitors, World Scientific, 1995:

[30] T. Takahashi, Solid copper (I) ion conductors, *J. Electroanal Chem.* 180 (1984) 231–239.

[31] T. Takahashi, High conductivity solid ionic conductors: Recent trends and applications, World Scientific,1989.

[32] P. G. Bruce, Chemistry of solid state materials: solid state electrochemistry, Cambridge University Press, 1995.

[33] R. Kanno, Y. Takeda, O. Yamamoto, Ionic conductivity of solid lithium ion conductors with the spinel structure: Li_2MCl_4 (M= Mg, Mn, Fe, Cd), *Mat. Res. Bull.* 16 (1981) 999–1005.

[34] C. Cao, Z. Li, X. Wang, X. Zhao, W. Han, Recent advances in inorganic solid electrolytes for lithium batteries, *Front. Energy Res.* 2 (2014) 1–10.

[35] S. Song, H.M. Duong, A.M. Korsunsky, N. Hu, L. Lu, A Na + Superionic Conductor for room-temperature sodium batteries, *Sci. Rep.* 6 (2016) 1–10.

[36] M. A. Evstigneeva, V. B. Nalbandyan, A. A. Petrenko, B. S. Medvedev, A. A. Kataev, A new family of fast sodium ion conductors: $Na_2M_2TeO_6$ (M = Ni, Co, Zn, Mg), *Chem. Mater.* 23 (2011) 1174–1181.

[37] K. Kuwabara, T. Takahashi, Formation of β-alumina type potassium gallate and its ionic conductivity, *J. Solid State Chem.* 19 (1973) 147–153.

[38] T. H. Etsell, S. N. Flengas, The electrical properties of solid oxide electrolytes, *Chem. Rev.* 70 (1970) 339–376.

[39] W. Strickler, W. G. Carlson, Ionic conductivity of cubic solid solutions in the system CaO-Y_2O_3-ZrO_2, *J. Am. Ceram. Soc.* 47 (1964) 122–127.

[40] D. W. Strickler, W. G. Carlson, Electrical conductivity in the ZrO_2-rich region of several M_2O_3-ZrO_2 systems, *J. Am. Ceram. Soc.* 48 (1965) 286–289.

[41] M. Balkanski, T. Takahashi, H. L. Tuller, Solid state ionics, in: *Proc. Symp. A2 Solid State Ionics Int. Conf. Adv. Mater.* ICAM 91, 1991.

[42] J. Portier, J.M. Reau, S. Matar, J.L. Soubeyroux, P. Hagenmuller, Advances on fluorine ion conductors, basic and applied research, *Solid State Ionics*. 11 (1983) 83–90.

[43] I. V Murin, O. V Glumov, N.A. Mel'nikova, Solid Electrolytes with predominant chloride conductivity, *Russ. J. Electrochem.* 45 (2009) 411–416.

[44] D. S. Khaerudini, G. Guan, P. Zhang, X. Hao, A. Abudula, Prospects of oxide ionic conductivity bismuth vanadate-based solid electrolytes, *Rev. Chem. Eng.* 30 (2014) 539–551.

[45] A. Chroneos, B. Yildiz, A. Tarancón, D. Parafitt, J. A. Kilner, Oxygen diffusion in solid oxide fuel cell cathode and electrolyte materials:mechanistic insights from atomistic simulations, *Energy Environ. Sci.* 4 (2011) 2774–2789.

[46] R. J. Brook, Concise encyclopedia of advanced ceramic materials, Elsevier, 1991.

[47] S. J. Skinner, J.A. Kilner, Oxygen ion conductors, *Mater. Today.* (2003) 30–37.

[48] F. W. Poulsen, An introduction to proton conduction in solids, 1980.

[49] J. W. Phair, S. P. S. Badwal, Review of proton conductors for hydrogen separation, *Ionics*. 12 (2006) 103–115..

[50] W. Gao, N. M. Sammes, An introduction to electronic and ionic materials, World Scientific, 1999.

[51] M. A. R. Rolando, The physical chemistry of materials: Energy and environmental applications, CRC Press, 2010.

[52] P. Knauth, M. L. D. Vona, Solid state proton conductors: Properties and application in fuel cells, Wiley, 2012.

[53] P. J. Gellings, H. J. M. Bouwmeester, The CRC handbook of solid state electrochemistry, CRC Press, 1997.

[54] L. N. Patro, K. Hariharan, Fast fluoride ion conducting materials in solid state ionics : An overview, *Solid State Ionics*. 239 (2013) 41–49.

[55] T. Ishihara, H. Matsuda, Y. Takita, Doped $LaGaO_3$ perovskite type oxide as a new oxide ionic conductor, *J. Am. Chem. Soc.* 116 (1994) 3801–3803.

[56] J. C. Boivin, G. Mairesse, Recent Material Developments in Fast Oxide Ion Conductors, *Chem. Mater*. 10 (1998) 2870–2888.

[57] S. P. Jiang, Y. Yan, Materials for high-temperature Fuel Cells, Wiley, 2013.

[58] K. R. Kendall, C. Navas, J. K. Thomas, H. Loye, Recent developments in perovskite-based oxide ion conductors, *Solid State Ionics.* 82 (1995) 215–223.

[59] C. Navas, H. Loye, Conductivity studies on oxygen-deficient Ruddlesden-Popper phases, *Solid State Ionics*. 93 (1997) 171–176.

[60] P. Lacorre, F. Goutenoire, O. Bohnke, R. Retoux, Y. Laligant, Designing fast oxide-ion conductors based on $La_2Mo_2O_9$, *Nature*. 404 (2000) 9–11.

[61] A. M. Azad, S. Larose, S. A. Akbar, Review Bismuth oxide-based solid electrolytes for fuel cells, *J. Mater. Sci.* 29 (1994) 4135–4151.

[62] K. R. Kendall, C. Navas, J. K. Thomas, H. Loye, Recent Developments in Oxide Ion Conductors: Aurivillius Phases, *Chem. Mater*. 8 (1996) 642–649.

[63] P. Shuk, H. D. Wiemhofer, U. Guth, W. Gopel, M. Greenblatt, Oxide ion conducting solid electrolytes based on Bi_2O_3, *Solid State Ionics.* 89 (1996) 179–196.

[64] Y.W. Long, L.X. Yang, Y. Yu, F.Y. Li, R.C. Yu, C.Q. Jin, Synthesis, structure , magnetism and specific heat of $YCrO_4$ and its zircon-to-scheelite phase transition, Phys. Rev. B. B75 (2007) 104402.

[65] K. Robinson, G. V Gibbs, P. H. Ribbe, The structure of Zircon: A comparison with Garnet, *Am. Mineral*. 56 (1971) 782-790.

[66] S. J. Patwe, S. N. Achary, A. K. Tyagi, Lattice thermal expansion of zircon-type $LuPO_4$ and $LuVO_4$: A comparative study, *Am. Mineral*. 94 (2009) 98–104.

[67] A. K. Tyagi, S. Banerjee, Materials under extreme condictions Recent trends and future prospects, Elsevier, 2017.

[68] S. N. Achary, S. J. Patwe, P. S. R. Krishna, A. B. Sindhe, A. K. Tyagi, Crystal structure analysis of Scheelite and Zircon type thorium germanates : A neutron diffraction study, *J. Alloy. Compd*. 438 (2007) 274–278.

[69] H. Li, S. Zhou, S. Zhang, The relationship between the thermal expansions and structures of ABO_4 oxides, *J. Solid State Chem.* 180 (2007) 589–595.

[70] R. J. Finch, J. M. Hanchar, Structure and chemistry of Zircon and Zircon-group minerals, *Rev. Mineral. Geochemistry*. 53 (2003) 1–25.

[71] D. Errandonea, R. Perales, J. Fuertes, A. Segura, S. N. Achary, A. K. Tyagi, High-pressure structural investigation of several zircon-type orthovanadates, *Phys. Rev. B*. 79 (2009) 184104-184112.

[72] O. Ermakova, Paszkowicz, J. Solano, A. Munoz, H. Dabkowska, Experimental and theoretical study of Zircon and Scheelite phases of $DyVO_4$, *Acta Phys. Pol. A*. 121 (2012) 920–924.

[73] E. V. Tsipis, M. V. Patrakeev, V. V. Kharton, N. P. Vyshatko, J. R. Frade, Ionic and p-type electronic transport in zircon-type $Ce_{1-x}A_xVO_{4\pm\delta}$ (A = Ca, Sr), *J. Mater. Chem.* 12 (2002) 3738–3745.

[74] C. Yu, M. Yu, C. Li, C. Zhang, P. Yang, J. Lin, Spindle-like lanthanide orthovanadate nanoparticles: Facile synthesis by ultrasonic irradiation, characterization, and luminescent properties, *Cryst. Growth Des.* 9 (2009) 783–791.

[75] W. Fan, X. Song, S. Sun, X. Zhao, Microemulsion-mediated hydrothermal synthesis and characterization of zircon-type $LaVO_4$ nanowires, *J. Solid State Chem.* 180 (2007) 284–290.

[76] Z. Xu, C. Li, Z. Hou, C. Peng, J. Lin, Morphological control and luminescence properties of lanthanide orthovanadate $LnVO_4$ (Ln = La to Lu) nano-/ microcrystals via hydrothermal process, *CrystEngComm*. 13 (2011) 474–482.

[77] Y. Oka, T. Yao, N. Yamamoto, Hydrothermal synthesis of Lanthanum vanadates: Synthesis and crystal structures of Zircon-type $LaVO_4$ and a new compound LaV_3O_9, *J. Solid State Chem.* 152 (2000) 486–491.

[78] A. Meldrum, S. J. Zinkle, L. A. Boatner, R. C. Ewing, Heavy-ion irradiation effects in the ABO_4 orthosilicates: Decomposition, amorphization, and recrystallization, *Phys. Rev. B.* 59 (1999) 3981–3992.

[79] C. T. G. Petit, R. Lan, P. I. Cowin, S. Tao, Structure and conductivity of strontium-doped cerium orthovanadates $Ce_{1-x}Sr_xVO_4$ ($0 \leq x \leq 0.175$), *J. Solid State Chem.* 183 (2010) 1231–1238.

[80] X. Wang, I. Loa, K. Syassen, M. Hanfland, B. Ferrand, Structural properties of the zircon- and scheelite-type phases of YVO_4 at high pressure, *Phys. Rev. B.* 70 (2004) 064109.

[81] B. C. Chakoumakos, M. M. Abraham, L. A. Boatner, Crystal structure refinements of zircon- type MVO_4 (M=Sc, Y , Ce, Pr, Nd, Tb, Ho, Er, Tm, Yb, Lu), *J. Solid State Chem.* 109 (1994) 197–202.

[82] D. F. Mullica, E. L. Sappenfield, M. M. Abraham, B. C. Chakoumakos, L. A. Boatner, Structural investigations of several $LnVO_4$ compounds, *Inorganica Chim. Acta.* 15 (1996) 85–88.

[83] M. Yi, S. Park, C. Seong, Y. Piao, T. Yu, The general synthesis and characterization of rare earth orthovanadate nanocrystals and their electrochemical applications, *J. Alloy. Compd.* 693 (2017) 825–831.

[84] H. Zhan, J. Shu, X. Wei, K. Wang, J. Chen., Cerium vanadate nanoparticles as a new anode material for lithium ion batteries, *RSC Adv.* 3 (2013) 7403–7407.

[85] L. Adijanto, V. B. Padmanabhan, K. J. Holmes, R. J. Gorte, J. M. Vohs, Physical and electrochemical properties of alkaline earth doped, rare earth vanadates, *J. Solid State Chem.* 190 (2012) 12–17.

[86] L. Adijanto, V. B. Padmanabhan, K. Rainer, R. J. Gorte, J. M. Vohs, Transition metal-doped rare earth vanadates : A regenerable catalytic material for SOFC anodes, *J. Mater. Chem.* 22 (2012) 11396–11402

[87] N. Danilovic, J. Luo, K.T. Chuang, A. R. Sanger, $Ce_{0.9}Sr_{0.1}VO_x$ (x=3, 4) as anode materials for H_2S-containing CH_4 fueled solid oxide fuel cells, *J. Power Sources.* 192 (2009) 247–257.

[88] E. V. Tsipis, V. V. Kharton, N. P. Vyshatko, A. L. Shaula, J. R. Frade, Stability and oxygen ionic conductivity of zircon-type $Ce_{1-x}A_xVO_{4+\delta}$ (A=Ca, Sr), *J. Solid State Chem.* 176 (2003) 47–56.

[89] T. H. Gayathri, A. A. Yaremchenko, K. Zakharchuk, J. James, Effect of magnesium addition on the structural , microstructural and electrical properties of YVO_4, *J. Alloy. Compd.* 672 (2016) 549–557.

[90] E. V. Tsipis, M. V. Patrakeev, V. V. Kharton, N. P. Vyshatko, J. R. Frade, Ionic and p-type electronic transport in zircon-type $Ce_{1-x}A_xVO_{4\pm\delta}$ (A = Ca, Sr), *J. Mater. Chem.* 12 (2002) 3738–3745.

[91] C. Peng, J. Luo, A. R. Sanger, K. T. Chuang, Sulfur-tolerant anode catalyst for solid oxide fuel cells operating on H_2S-containing syngas, *Chem. Mater.* 22 (2010) 1032–1037.

[92] J. W. Fergus, Oxide anode materials for solid oxide fuel cells, *Solid State Ionics.* 177 (2006) 1529–1541.

[93] J. B. Goodenough, Y. Huang, Alternative anode materials for solid oxide fuel cells, *J. Power Sources.* 173 (2007) 1–10.

[94] C. T. G. Petit, R. Lan, P. I. Cowin, A. Kraft, S. Tao, Structure, conductivity and redox stability of solid solution $Ce_{1-x}Ca_x$ VO_4 ($0 \leq x \leq 0.4125$), *J. Mater. Sci.* 46 (2011) 316–326.

[95] A. Watanabe, Highly conductive oxides, $CeVO_4$, $Ce_{1-x}M_xVO_{4-0.5x}$ (M=Ca, Sr, Pb) and $Ce_{1-y}Bi_yVO_4$, with Zircon-type structure prepared by solid-state reaction in air, *J. Solid State Chem.* 153 (2000) 174–179.

[96] C. T. G. Petit, R. Lan, P. I. Cowin, J. T. S. Irvine, S. Tao, Novel redox reversible oxide, Sr-doped cerium orthovanadate to metavanadate, *J. Mater. Chem.* 21 (2011) 525–531.

[97] N. S. Rao, O. G. Palanna, Electrical, thermal and infrared studies of cerium(Ill) orthovanadate, *Bull. Mater. Sci.* 18 (1995) 593–597.

[98] K. Gaur, H. B. Lal, Electrical transport in light rare-earth vanadates, *J. Mater. Sci.* 20 (1985) 3167–3176.

[99] K. Gour, H. B. Lal, Electrical transport in heavy rare-earth vanadates, *J. Mater. Sci.* 21 (1986) 2289–2296.

[100] K. Gaur, H. B. Lal, Electrical transport and semiconductor-semi- metal transition in $LaVO_4$, *J. Mater. Sci.* 19 (1984) 3325–3329.

[101] Y. P. Yadava, R. A. Singh, B. M. Wanklyn, Electrical conduction in $PrVO_4$ single crystal, *J. Mater. Sci. Lett.* 4 (1985) 224–226.

[102] M. Huse, T. Norby, R. Haugsrud, Proton conductivity in acceptor-doped $LaVO_4$, *J. Electrochem. Soc.* 158 (2011) B857–B865.

[103] T. Ishihara, Perovskite oxides for solid oxide fuel cells, Springer, 2009.

[104] T. Hibino, K. Ushiki, Y. Kuwahara, Electrochemical oxygen pump using CeO_2-based solid electrolyte for NOx detection independent of O_2 concentration, *Solid State Ionics.* 93 (1997) 309–314.

[105] E. N. Naumovich, V. V Kharton, V. V Samokhval, A. V Kovalevsky, Oxygen separation using Bi_2O_3 -based solid electrolytes, *Solid State Ionics*. 93 (1997) 95–103.

[106] P. K. Moon, H. L. Tuller, Evaluation of the $Gd_2(Zr_xTi_{1-x})_2O_7$ pyrochlore system as an oxygen gas sensor, *Sens. Actuators.* B1 (1990) 199–202.

[107] H. J. M. Bouwmeester, A. J. Burggraaf, Fundamentals of inorganic membrane science and technology, Elsevier, 1996.

[108] S. S. Hashim, A. R. Mohamed, S. Bhatia, Oxygen separation from air using ceramic-based membrane technology for sustainable fuel production and power generation, *Renew. Sustain. Energy Rev.* 15 (2011) 1284–1293. doi:10.1016/j.rser.2010.10.002.

[109] V. V. Kharton, A. A. Yaremchenko, A. P. Viskup, M. V. Patrakeev, I. A. Leonidov, V. L. Kozhevnikov, et al., Oxygen Permeability and ionic conductivity of perovskite-related $La_{0.3}Sr_{0.7}Fe(Ga)O_{3-\delta}$, *J. Electrochem. Soc*. 149 (2002) E125–E135.

[110] A. L. Shaula, V. V Kharton, F. M. B. Marques, Ionic and electronic conductivities , stability and thermal expansion of $La_{10-x}(Si,Al)_6O_{26\pm\delta}$ solid electrolytes, *Solid State Ionics.* 177 (2006) 1725–1728.

[111] P. J. Gelings, H. J. M. Bouwmeester, Ion and mixed conducting oxides as catalysts, *Catal. Today.* 12 (1992) 1–105.

[112] E. C. Subbarao, Solid Electrolytes and their applications, Springer, 1980.

[113] S. Geller, Solid Electrolytes,Springer, 1977

[114] R. Ramamoorthy, P. K. Dutta, S. A Akbar, Oxygen sensors: Materials, methods , designs and applications, *J. Mater. Sci.* 38 (2003) 4271–4282.

[115] T. Hong, S. Fang, M. Zhao, F. Chen, H. Zhang, S. Wang, K. S. Brinkman, An intermediate-temperature oxygen transport membrane based on rare-earth doped Bismuth Oxide $Dy_{0.08}W_{0.04}Bi_{0.88}O_{2-\delta}$, *J. Electrochem. Soc.* 164 (2017) F347–F353.

[116] Z. Lü, R. Wang, X. Huang, C. Liu, B. Wei, W. Su, Oxygen pump method for leak rate testing of SiO_2-B_2O_3-Al_2O_3-BaO-PbO_2-ZnO glass sealant for SOFC, *Solid State Ionics*. 179 (2008) 1286–1290.

[117] A. Q. Pham, R. S. Glass, Oxygen pumping characteristics of yttria-stabilized-zirconia, *Electrochim. Acta*. 43 (1998) 2699–2708.

[118] Y. Wei, W. Yang, J. Caro, H. Wang, Dense ceramic oxygen permeable membranes and catalytic membrane reactors, *Chem. Eng. J.* 220 (2013) 185–203.

[119] V. V. Kharton, A. A. Yaremchenko, A. V. Kovalevsky, A. P. Viskup, E. N. Naumovich, P. F. Kerko, Perovskite-type oxides for high-temperature oxygen separation membranes, *J. Memb. Sci.* 163 (1999) 307–317.

[120] V. V. Kharton, E. N. Naumovich, A. V. Nikolaev, Materials of high-temperature electrochemical oxygen membranes, *J. Memb. Sci.* 111 (1996) 149–157.

[121] F. T. Ciacchi, S. P. S. Badwal, V. Zelizko, Tubular zirconia–yttria electrolyte membrane technology for oxygen separation, *Solid State Ionics.* 152-153 (2002) 763–768.

[122] A. B. Stambouli, E. Traversa, Solid oxide fuel cells (SOFCs): A review of an environmentally clean and efficient source of energy, *Renew. Sustain. Energy Rev*. 6 (2002) 433–455.

[123] M. Irshad, K. Siraj, R. Raza, A. Ali, P. Tiwari, B. Zhu, et al., A brief description of high temperature solid oxide fuel cell's operation, materials, design, fabrication technologies and performance, *Appl. Sci*. 6 (2016) 75.

[124] C. Sun, U. Stimming, Recent anode advances in solid oxide fuel cells, *J. Power Sources*. 171 (2007) 247–260.

[125] J. W. Fergus, R. Hui, X. Li, D. P. Wilkinson, J. Zhang, Solid Oxide Fuel Cells, Materials, Properties and Performance, CRC Press, 2009.

[126] J. W. Fergus, Electrolytes for solid oxide fuel cells, *J. Power Sources.* 162 (2006) 30–40.

CHAPTER 2

INFLUENCE OF MAGNESIUM-DOPING ON SOME ZIRCON-TYPE RARE-EARTH ORTHOVANADATES: STRUCTURAL AND ELECTRICAL CHARACTERIZATION

Undoped $LnVO_4$ and Mg-doped $Ln_{0.95}V_{0.95}Mg_{0.10}O_{4-\delta}$ (Ln = Pr, Sm, Gd, Dy and Er) orthovanadates were synthesized by solid state method and characterized by XRD, SEM/EDS, electrical conductivity measurements, and determination of oxygen-ion transference numbers by modified e.m.f. technique. XRD analysis showed the formation of phase-pure materials. Trace amounts of MgO and Mg-V-O phases revealed by SEM/EDS suggest that the solid solubility of Mg cations in $LnVO_4$ lattice is somewhat lower than the nominal doping level, and that Mg substitutes preferentially into V sublattice. $LnVO_4$ and $Ln_{0.95}V_{0.95}Mg_{0.10}O_{4-\delta}$ show semiconducting behavior under oxidizing conditions at 450-950°C and are predominantly oxygen-ionic conductors, except $PrVO_4$ which is a mixed conductor. In $LnVO_4$ series, electrical conductivity is highest for $PrVO_4$ and $SmVO_4$ (~4×10^{-4} S/cm at 800°C) and decreases with increasing atomic number of rare-earth cation for other compositions. Additions of Mg results in a drop of electrical conductivity, by 1.5-2 times for most of compositions. Interstitial oxygen diffusion is discussed as a prevailing mechanism of ionic transport in undoped $LnVO_4$, whilst Mg doping suppresses the formation of interstitial oxygen ions. Humidified atmosphere has rather negligible impact on the electrical properties of substituted ceramics, indicating only minor (if any) protonic contribution to the total electrical transport of the studied orthovanadates.

T. H. Gayathri, A. A. Yaremchenko, J. Macías, P. Abhilash, S. Ananthakumar, "Magnesium-doped zircon-type rare-earth orthovanadates: structural and electrical characterization", Ceram. Int, 44 (2018) 96-103.

2.1. Introduction

Over the past few decades, significant research efforts have spent into the development of ionically conducting solids, particularly oxygen ion conductors. The importance of these materials has generated extensive scientific and technological concern and there have been a continued drive for their application in crucial areas such as solid electrolytes in solid oxide fuel cells, oxygen pumps, gas sensors, oxygen permeable catalysts, batteries, electrochromics and displays etc.[1-5] The necessity of highly conducting solid materials for higher temperature applications outlines the importance of alternatives. This challenge can be overcome either by improving already existing materials i.e., by choosing suitable dopants or by searching for new classes of materials.[6] Acceptor-type doping probably leads to a charge imbalance and is compensated by introduction of oxygen vacancies. This leads to oxide ion conductivity depending on vacancy concentration and oxide ion mobility.[3,6] Conventional categories of solid oxide ionic conductors include fluorite type or perovskite type oxides as the superior candidates, with yttria stabilized zirconia (YSZ) as the widely used electrolyte for practical applications.

Recently, there has been a huge attraction for ionic conductivity in oxides of other structural types.[7,8] $REXO_4$ (where RE is the rare-earth elements including lanthanoids from La to Lu as well as Y and Sc, and X is a pentavalent cation) compounds are considered as potential candidates for a number of existing and emerging technologies. Rare-earth orthovanadates ($REVO_4$) and particularly lanthanide orthovanadates ($LnVO_4$) belong to the large family of $REXO_4$ have attracted significant research interest in the last two decades due to their versatile physical properties such as luminescence, Jahn-Teller phase transitions, magnetic and electronic properties, catalytic activity etc.[9-13] These materials show diverse application in various fields such as host materials for phosphors

and high power lasers, counter electrodes in electrochromic devices, gas sensors, components of oxide fuel cell anodes, oxidative dehydrogenation of light alkanes thermophosphors for remote temperature measurements, birefringent materials, optical polarizers, X-ray and γ-ray scintillators for medical imaging applications, chemically durable materials for waste disposal etc.[13-17] Under ambient pressure, $LnVO_4$ orthovanadates crystallize in two polymorphs, either tetragonal zircon-type ($ZrSiO_4$) or monoclinic monazite-type ($CePO_4$) structure with space groups $I4_1/amd$ and $P2_1/n$, respectively. Larger La cation favors stabilization of monazite-type structure[18], while orthovanadates based on other rare-earth cations belong to zircon-type structural family[9,12,13,19-21] Tetragonal zircon-type structure is composed of four formula units per unit cell and can be viewed as a network of alternating edge-sharing LnO_8 dodecahedra and VO_4 tetrahedra forming chains parallel to the c-axis, while for monazite structure LnO_9 polyhedra are edge-shared with VO_4 tetrahedra along the c-axis.[13,18,22]

In the last ten years mixed metal vanadates have attracted huge attention as a prospective material for electrochemical applications such as Li ion batteries[23,24] and solid oxide fuel cells (SOFCs).[16,25-30] One important advantage of $LnVO_4$-derived components of SOFC anodes is their good resistance to carbon deposition and sulphur-poisoning[27,30-32]which is critical for hydrocarbon-fueled SOFCs. Inspection of available literature shows that the most studied system among $LnVO_4$ series is cerium orthovanadate, $CeVO_4$.[16,19,20,29,33-35]

So far the impact of alkaline earth ion such as Mg on the electrical properties of zircon-type $LnVO_4$ has not been explored in detail. Mg is known to have moderately good stability and is considered to be an appropriate candidate which will not reduce the substituent ion and thus admits for the study of its effect on the electrical properties of the material.[28,36]

Assuming common oxygen vacancy diffusion mechanism of ionic transport, acceptor-type substitution, e.g. by magnesium, in either sublattice of $LnVO_4$ may be expected to increase the concentration of oxygen vacancies in zircon-type structure, thus improving ionic conduction. Aliovalent doping by magnesium is frequently used to enhance oxygen-ionic conductivity in variety oxide ceramics materials such as LSGM solid electrolytes, perovskite-type titanates or fluorite-type ceria-based solid solutions. The ionic radius of Mg^{2+} cations is intermediate between that of octacoordinated Ln^{3+} and tetracoordinated V^{5+} implying that theoretically magnesium cations may substitute in each of sublattices. Many reports are available on the studies of acceptor-type Mg substitution on different cationic sites of ceramic oxides aiming to improve the transport properties of the material.[28,37-42] Li et al.[39]reported an increase of ionic conductivity on Mg doping in the Ti site of ferroelectric perovskite $Na_{0.5}Bi_{0.5}TiO_3$. In addition to the enhancement of ionic conductivity of the system, Mg doping reduced the sintering temperature and improved the electrolyte stability in reducing atmosphere. Enhancement of total oxide ion conductivity of well known oxide ion conductor $La_{1-x}Sr_xGa_{1-y}Mg_yO_{3-\delta}$ (LSGM) on excess doping of Mg on Ga site was reported by Zhao et al.[42] Higher ionic conductivity was due to the higher concentration of mobile ions generated by the excess Mg. Improvement of conductivity of Mg-excess sample was explained on the basis of dopant-vacancy association formation mechanism and also the formation of more conductive grain-boundary phase composition at higher temperature by the re-dissolution of Mg rich phase along the grain boundaries. Kinoshita et al.[38] studied the effect of Mg substitution on the oxide ion conductivity of apatite-type lanthanum silicate ($La_{9.33}Si_6O_{26}$). The partial replacement of La by Mg decreased the conductivity, whereas substitution for Si increased the conductivity with the amount of Mg and dual doping resulted in slight improvement of conductivity. In this background we have chosen

tetragonal zircon-type $LnVO_4$ (Ln = Pr, Sm, Gd, Dy and Er) as our host lattice and investigated the effect of substitution of a third cation such as Mg on the structural, microstructural and electrical properties of the system (present study).

2.2. Influence of Magnesium-substitution on some Zircon-type rare-earth orthovanadates: Structural and electrical characterization

The present work is focused on the impact of acceptor-type doping by magnesium on the electrical properties of zircon-type $LnVO_4$ (Ln = Pr, Sm, Gd, Dy, Er) orthovanadates. The nominal cation composition of doped orthovanadates was formulated as $Ln_{0.95}V_{0.95}Mg_{0.10}O_{4-\delta}$ ($\equiv(Ln_{0.95}Mg_{0.05})(V_{0.95}Mg_{0.05})O_{3.90}$) in order to elucidate the mechanism of substitution.

2.2.1. Experimental

2.2.1.1. Solid state reaction route for ceramics synthesis

A conventional solid state reaction technique was adopted for the synthesis of $LnVO_4$ (Ln = Pr, Sm, Gd, Dy, Er) and $Ln_{0.95}V_{0.95}Mg_{0.10}O_{4-\delta}$ samples in the present work.

Solid state ceramic route is one of the most widely accepted and easiest approaches for the preparation of polycrystalline ceramic materials. Direct reaction of the starting materials in solid state is occurring in this method. Generally the solids do not react together at room temperature over normal time scales. For the reaction to takes place at a considerable rate, it is necessary to heat the materials to high temperature. The steps involved in the preparation process of ceramic materials are represented in fig. 2.1.

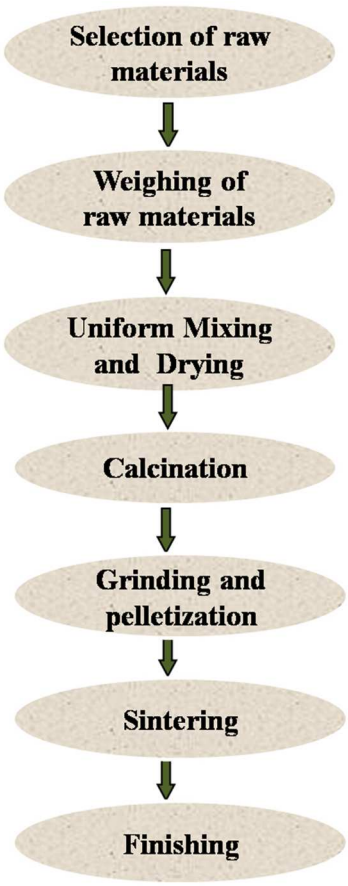

Figure 2.1: Flowchart showing the steps involved in solid state reaction method

High purity ceramic oxides/carbonates are taken as the raw materials. In the present work $Mg_5(CO_3)_4(OH)_2*5H_2O$ (99.0%, Sigma-Aldrich), Pr_6O_{11}, Sm_2O_3, Gd_2O_3, Dy_2O_3, Er_2O_3 (99.0%, IRE, India), V_2O_5, (99.6+%, Sigma-Aldrich) were used as the starting materials. In order to obtain maximum homogeneity, dried powders of the starting reagents were weighed stoichiometrically, mixed thoroughly in appropriate proportions and ball-milled for 24 hours in ethanol medium using yttria stabilized zirconia balls. The slurry was then kept in hot air oven for drying pre-calcined at 650°C and 750°C for 6 hours in air at each temperature with intermediate grindings, and then calcined at 1000°C for 30 hours with several re-grindings. Calcined powders were then ground well in to fine powders and mixed with the binder, 4 wt. % polyvinyl alcohol, PVA (average molecular weight 72,000, BDH Lab suppliers, Poole, U.K.), dried and ground well again. These powders were pressed uniaxially at 100 MPa into disk-shaped compacts and sintered in

air for 6 hours at 1300°C for $LnVO_4$ and 1250°C for Mg-doped materials in air with an intermediate soaking at 600°C to expel the binder. During sintering, the pellets were properly covered by the powders of the same cation composition to minimize possible high-temperature losses. Optimization of sintering conditions was considered to reduce porosity. The density of sintered samples was calculated from the mass and geometric dimensions.

X-ray diffraction (XRD) patterns of the prepared ceramic materials were recorded using PANalytical X'pert Pro diffractometer (Ni-filtered Cu-Kα radiation). Refinement of the XRD data was conducted using X'pert Highscore Plus software in order to elucidate the lattice parameters and calculate theoretical density. Microstructural analysis of the sintered, polished and thermally etched samples coated with palladium–gold mixture was performed with the aid of a scanning electron microscope (SEM, JEOL JSM-5600 LV). Determination of possible minor phase impurities was performed using SEM (Hitachi SU-70 microscope) coupled with energy dispersive spectroscopy (EDS, Bruker Quantax 400 detector).

For electrical measurements, porous Pt electrodes were painted onto flat surfaces of polished ceramic samples and sintered at 950°C for 30 min. The electrical conductivity (σ) was studied in controlled atmospheres using impedance spectroscopy (Agilent 4284A precision LCR meter, frequency range 20 Hz-1 MHz). The measurements were performed in temperature range 400-900°C in cooling regime with equilibration at each temperature step. In the course of electrical studies, oxygen partial pressure and relative humidity in the gas flow were continuously monitored by the yttria-stabilized zirconia solid-electrolyte sensor and by Jumo humidity transducer, respectively. The relative humidity in air (supplied by air compressor with drying unit) corresponded to ≤ 10% (at room temperature). The term "wet" air refers to a gas humidified by bubbling through

distilled water at room temperature. The average oxygen-ion transference numbers ($\overline{t_O}$) for selected materials were determined by the modified electromotive force (e.m.f.) technique employing air,Pt | oxide | Pt,O_2 oxygen concentration cells and taking electrode polarization into account.[43,44]

2.2.2. Characterization Techniques

2.2.2.1. Structural and Microstructural characterization

2.2.2.1.1. Powder X-ray Diffraction

X-ray powder diffraction (XRD) is an instrumental technique primarily used for revealing the crystal structure. It is more useful for qualitative analysis rather than quantitative analysis. Monochromatic X-ray beam which incident on the crystalline sample will either be transmitted or scattered by the electrons of the atoms in the material. Generally, the scattered waves will interfere destructively with each other. Though, in special orientations the waves interfere constructively where Bragg's Law ($n\lambda = 2d\sin\theta$) is satisfied. The direction and intensity of the diffracted beam depends on the crystal orientation with respect to the incident beam. The crystal lattice consists of parallel rows of atoms which are separated by a particular distance known as inter planar spacing or simply d-spacing (d), which are able to diffract the X-rays. The wavelength (λ) of the characteristic spectrum of X-rays can be comparable to d-spacing. Intense reflected beam will be produced when the path difference between the reflections from these successive planes is equal to the whole number multiple of the wavelength and the sharp intense maxima observed at a specific direction in the diffraction spectrum is the direct proof for the crystallinity of the material. The powdered samples provides random orientation of particles in all possible directions so that the complete idea about the crystal structure can be available by the precise analysis of the diffraction pattern.[45]

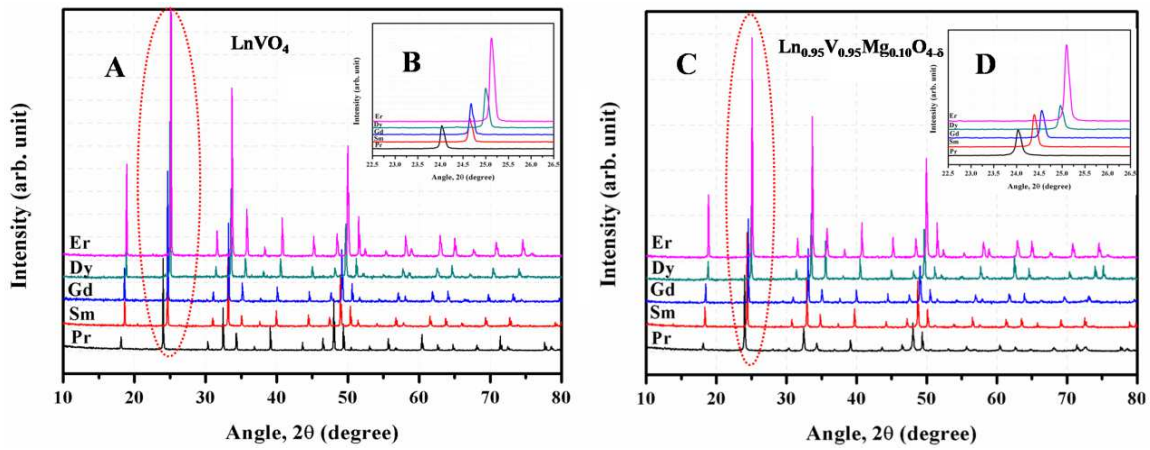

Figure 2.2: XRD patterns of as-prepared (A) $LnVO_4$ and (C) $Ln_{0.95}V_{0.95}Mg_{0.10}O_{4-\delta}$ ceramics. Insets show expanded view of (200) reflection for (B) $LnVO_4$ and (D) $Ln_{0.95}V_{0.95}Mg_{0.10}O_{4-\delta}$.

Fig. 2.2 (A and C) demonstrates the XRD patterns of as prepared $LnVO_4$ and $Ln_{0.95}V_{0.95}Mg_{0.10}O_{4-\delta}$ samples. XRD analysis indicates that the entire patterns are highly crystalline in nature. All the reflections can be indexed in space group $I4_1/amd$ characteristic for tetragonal zircon-type structure, in agreement with the reference data for undoped orthovanadates [ICDD PDF #01-082-1970 (Pr), 01-074-8274 (Sm), 01-086-0996 (Gd), 01-074-8276 (Dy), 01-078-5264 (Er)]. No impurity peaks were observed in XRD patterns of Mg-doped samples (fig. 2.2.C) point towards a complete solid solution formation of the samples upon Mg addition. An expanded view of XRD patterns in the range $2\theta = 22.5\text{-}26.5°$ can be seen from the insets in fig. 2.2. (B and D). The intense 200 reflection shifts to a higher angle with increasing atomic number of Ln cation, in correlation with the decrease of its ionic radius.[46] This observation is common for both $LnVO_4$ and $Ln_{0.95}V_{0.95}Mg_{0.10}O_{4-\delta}$ series.

2.2.2.1.2. Rietveld refinement

Structural refinement using Rietveld analysis is one of the best technique that have been developed for extracting structural details from powder diffraction data. The method make use of a trial structure for starting the refinement process and then calculate its powder diffraction profile and finally compare it with the measured profile. Modification

of the trial structure can be done by varying the refineable parameters such as lattice parameters, site occupancies, atomic positions, peak shape parameters etc. until the measured pattern will form a best-fit match with the trial structure. The consistency of the outcome of the refinement result not only depends on the starting model to be refined but also on the data quality, on the integrity of the description of the observed profile by the analytical function and on the refinement approach. The entire diffraction profile is calculated (model) and is then compared with the observed step profile and finally the adjustment of the parameters of the model is done by least square method. The process of refinement will continue until we get a best fit. The progress of refinement is monitored by several criteria of fit, among them the quality of fitting between the observed and calculated profile is evaluated by various residual parameters or R values like profile factor (R_p), weighted profile factor (R_{wp}) and expected weight profile factor (R_{exp}) and Goodness of Fit (GOF, χ^2).[47-49]

$$R_p = \frac{100\sum_{i=1}^{n}|y_i - y_{c,i}|}{\sum_{i=1}^{n} y_i} \qquad 2.1$$

where y_i, $y_{c,i}$ and n indicates the experimental, calculated and total number of points respectively.

$$R_{wp} = 100\left[\frac{\sum_{i=1}^{n}\omega_i|y_i - y_{c,i}|^2}{\sum_{i=1}^{n}\omega_i y_i^2}\right]^{1/2} \qquad 2.2$$

Here ω_i is the reciprocal of the variance of observation y_i

$$R_{exp} = 100\left[\frac{n-p}{\sum_{i=1}^{n}\omega_i y_i^2}\right]^{\frac{1}{2}} \qquad 2.3$$

Here $(n-p)$ represents the number of degrees of freedom (n is the total number of experimental points and p is the number of refined parameters

$$\chi^2 = \left[\frac{R_{wp}}{R_{exp}}\right]^2 \qquad 2.4$$

Detailed analysis on the obtained XRD data in the current work was performed by Rietveld simulation and refinement using X'Pert Highscore Plus software so as to elucidate the structural modification resulted from Mg substitution. The standard ICDD pattern similar to the observed peak profile and the stoichiometry anticipated for the preparation of the system were considered to make starting models for the simulation. In this way, the reference data for tetragonal zircon-type $LnVO_4$ with space group $I4_1/amd$ (no. 141) and respective rare-earth cations (explained in section 2.2.2.1.1.) were used as starting model for Rietveld refinement. In zircon-type structure, rare-earth cations, vanadium cations and oxygen ions occupy 4a(0,3/4,1/8), 4b(0,1/4,3/8) and 16h(x,y,z) sites, respectively. Magnesium cations may be expected to be distributed equally between 4a and 4b positions, or to substitute preferentially into one of the sublattices. The latter must be accompanied either by the formation of cation vacancies in second sublattice or segregation of secondary phase(s) in order to maintain the lattice conservation condition. The refinements based on all three possibilities (substitution in Ln sublattice, V sublattice, or equally in both sublattices) were carried out. Pseudo-Voigt peak shape function was used for profile fitting. Even though all these models produced satisfactory results, the model based on magnesium cations distribution in both 4a and 4b sites yielded a better fit. Structural refinement results for the $Ln_{0.95}V_{0.95}Mg_{0.10}O_{4-\delta}$ samples are summarized in Table 2.1. Corresponding data for $LnVO_4$ series are given in Table 2.2.

Table 2.1: Rietveld refinement parameters for $Ln_{0.95}V_{0.95}Mg_{0.10}O_{4-\delta}$

Ln	Pr	Sm	Gd	Dy	Er
Structure	Zircon	Zircon	Zircon	Zircon	Zircon
Unit cell	Tetragonal	Tetragonal	Tetragonal	Tetragonal	Tetragonal
Space group	*I4₁/amd*	*I4₁/amd*	*I4₁/amd*	*I4₁/amd*	*I4₁/amd*
Lattice constant, Å					
a	7.3629(4)	7.2646(2)	7.2099(3)	7.1438(4)	7.0974(2)
c	6.4655(4)	6.3869(2)	6.3496(3)	6.3108(4)	6.2742(4)
R_{exp}	15.32	12.19	9.43	8.98	8.73
R_p	15.16	12.95	7.99	8.28	9.32
R_{wp}	18.69	16.37	10.07	11.20	11.37
GOF	1.49	1.80	1.14	1.55	1.82

Table 2.2: Rietveld refinement parameters for $LnVO_4$

Ln	Pr	Sm	Gd	Dy	Er
Structure	Zircon	Zircon	Zircon	Zircon	Zircon
Unit cell	Tetragonal	Tetragonal	Tetragonal	Tetragonal	Tetragonal
Space group	*I4₁/amd*	*I4₁/amd*	*I4₁/amd*	*I4₁/amd*	*I4₁/amd*
Lattice constant, (Å)					
a					
c	7.3622(3)	7.2696(1)	7.2127(1)	7.1477(2)	7.0977(2)
	6.4644(3)	6.3912(2)	6.3485(1)	6.3096(2)	6.2753(2)
R_{exp}	10.36	12.65	9.49	8.33	8.61
R_p	10.53	11.89	7.47	7.30	8.44
R_{wp}	13.79	15.10	9.54	9.24	10.68
GOF	1.77	1.43	1.01	1.23	1.54

In both cases, the lattice parameters show a linear variation with the ionic radius of rare-earth cations, as shown in fig. 2.3; both a and c lattice constants reasonably decrease

with decreasing ionic radius of Ln^{3+}. Doping with magnesium has rather negligible effect of the lattice parameters.

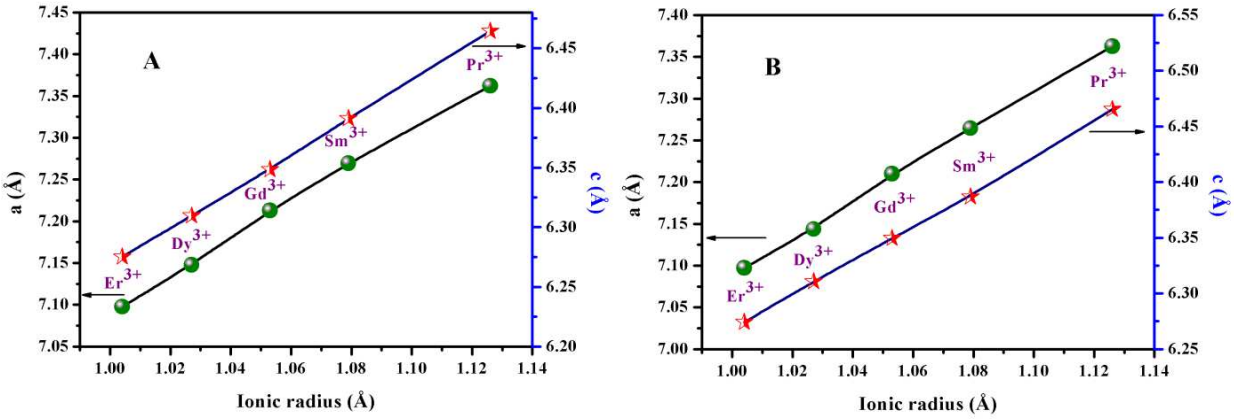

Figure 2.3: Dependence of lattice parameters of (A) $LnVO_4$ and (B) $Ln_{0.95}V_{0.95}Mg_{0.10}O_{4-\delta}$ on ionic radius of Ln^{3+} cation. Ionic radii are taken from Ref. [46]

The quality of the fit between the observed and calculated XRD pattern can be examined on the basis of different R-factors such as profile factor (R_p), expected weight profile factor (R_{exp}), weighted profile factor (R_{wp}) and goodness of fit (GOF) values[49]. In the present study, all the samples show GOF values <2, indicating a good agreement between the calculated and observed profile within the limits of experimental error. Fig. 2.4, fig. 2.5, fig. 2.6 shows the representative spectra of Rietveld refinement of XRD patterns of $GdVO_4$, $Gd_{0.95}V_{0.95}Mg_{0.10}O_{4-\delta}$ and $Er_{0.95}V_{0.95}Mg_{0.10}O_{4-\delta}$ samples respectively showing experimental, calculated and the difference profiles.

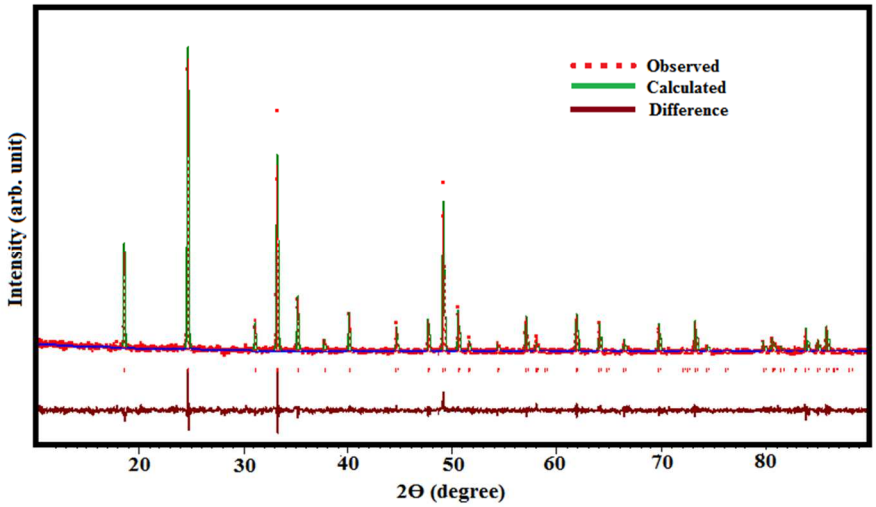

Figure 2.4: Rietveld refinement spectrum for the sample $GdVO_4$

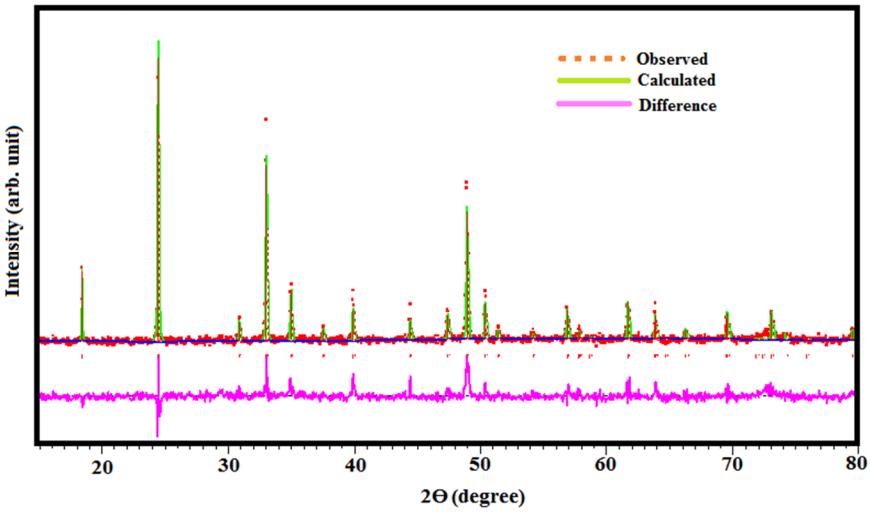

Figure 2.5: Rietveld refinement spectrum for the sample $Gd_{0.95}V_{0.95}Mg_{0.10}O_{4-\delta}$

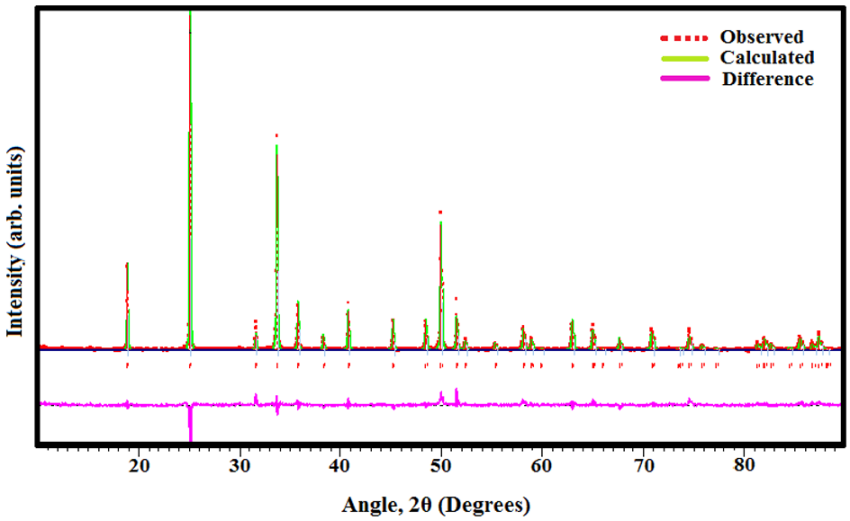

Figure 2.6: Rietveld refinement spectrum for the sample $Er_{0.95}V_{0.95}Mg_{0.10}O_{4-\delta}$.

2.2.2.1.3. Scanning Electron Microscopy (SEM)

Scanning electron microscope is a type of electron microscope in which images are produced by electron mapping of the specimen and is capable of producing high resolution images of a sample surface. SEM uses electrons rather than visible light to form high resolution (1 nm to 20 nm) images. In SEM an electron beam is focused on to a small area on the specimen and is then scanned across the surface to create a two dimensional image. One of the major advantages of SEM over other traditional microscope is that it has large depth of field which offers more of a specimen to be in focus at one time.[50] SEM is mainly used for the study of surface morphology of the specimens. The interaction of primary electron with the specimen will generate secondary electrons, characteristic X-rays and backscattered electrons. The primary use mode in SEM is secondary electron imaging (SEI), which produces the surface morphology of the sample. In the present investigation, sintered ceramic samples prepared by proper polishing and thermal etching were used for SEM analysis.

2.2.2.1.4. Energy Dispersive X-ray (EDX) Spectroscopy

Energy dispersive x-ray analysis is an analytical technique used in combination with SEM or transmission electron microscope (TEM) primarily for the elemental analysis or micro chemical characterisation of a sample. The elemental analysis can be done by analysing the developed X-rays during the interaction of the specimen with the primary electron. When a primary beam of electron hit on the specimen it will results in the ejection of inner shell electrons from the sample. An outer shell electron will take its place releasing X-ray signal whose energy can be related its nuclear mass and the energy difference between the two electron orbits involved. These X-rays are characteristics of the material and can be detected and analysed by the energy dispersive X-ray spectrometer. The constituent elements of the samples can thus be determined by

analysing these characteristic X-rays. The characteristic X-ray signal is detected using detector and is converted in to electrical signals. The energy of the detected X-ray is then compared with the energy of the known samples in the system and creates characteristics peaks at different energy levels corresponding to the elements present. The area under the peak corresponds to the amount of each element present in the sample. EDS is useful for detecting impurities in the sample and also for determining the chemical composition of the material.

In the present case, as magnesium doping level is low and XRD is not sensitive to small amounts of phase impurities, ceramic samples were further inspected by SEM coupled with EDS to identify possible minor secondary phases. Microscopic analysis detected inclusions of periclase MgO phase and another phase belonging to Mg-V-O system. Representative examples of SEM/EDS results are shown in fig. 2.7. These results suggest two conclusions. First, solid solubility of magnesium in zircon lattice is below the nominal doping level. Limited solubility is caused probably by mismatch between the ionic radius of Mg^{2+} and both A-site ($r^{VIII}(Sm^{3+})$ = 1.079 Å, $r^{VIII}(Er^{3+})$ = 1.004 Å and $r^{VIII}(Mg^{2+})$ = 0.89 Å)[46] and B-site cations ($r^{IV}(V^{5+})$ = 0.355 Å and $r^{IV}(Mg^{2+})$ = 0.57 Å) in host lattices. Secondly, magnesium prefers to substitute into vanadium sublattice, and this is compensated by segregation of Mg-V-O phase to maintain the A:B = 1:1 cation ratio.

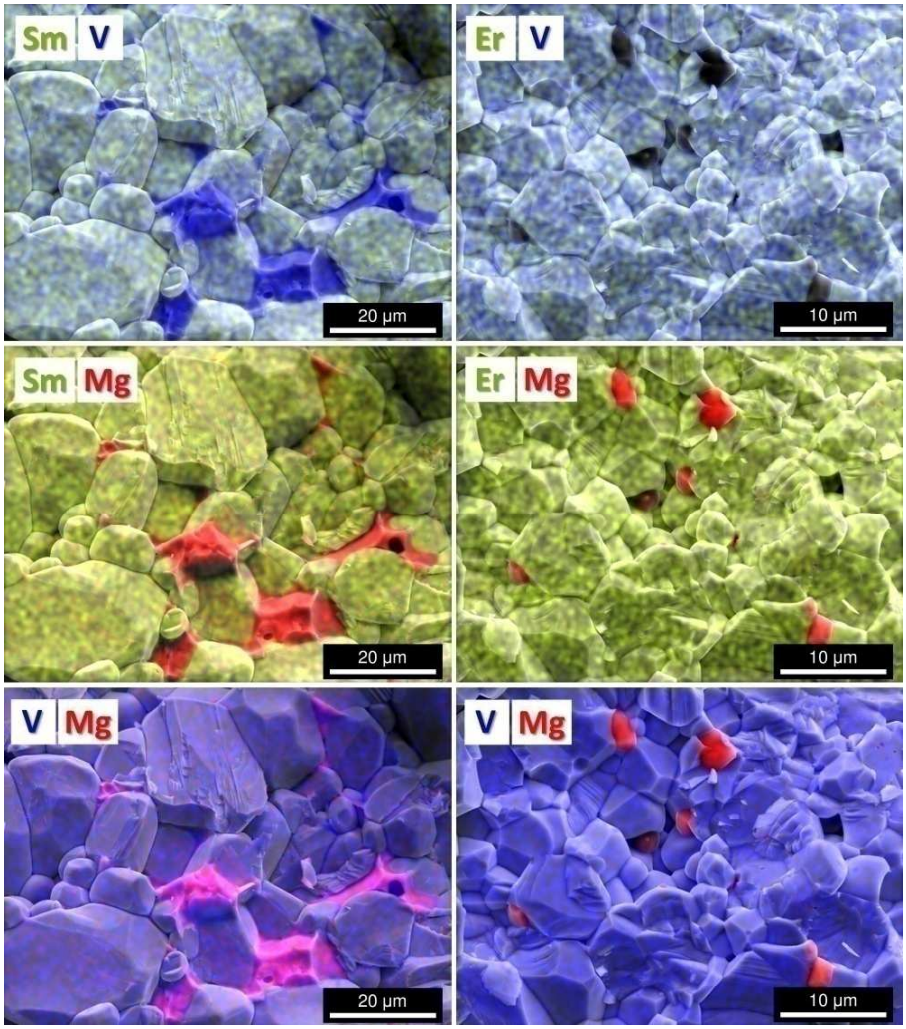

Figure 2.7: SEM micrograph of fractured $Ln_{0.95}V_{0.95}Mg_{0.10}O_{4-\delta}$ ceramics with overlaid EDS elemental maps showing the inclusions of Mg-V-O phase (left column) and periclase MgO phase (right column).

Experimental and relative densities of sintered ceramic samples are given in Table 2.3. $PrVO_4$ and $SmVO_4$ ceramics were comparatively porous, whereas other samples had relative density around 90% or higher. Doping with magnesium apparently improves sinterability. This can be attributed to the presence of traces of Mg-V-O phase with low melting temperature (melting temperatures of $Mg_2V_2O_7$ and $Mg_3(VO_4)_2$ correspond to ~1135 and ~1212°C, respectively [51,52]).

Table 2.3: Density and relative density of sintered ceramics

$LnVO_4$			$Ln_{0.95}V_{0.95}Mg_{0.10}O_{4-\delta}$		
Ln	Density, g/cm^3	Relative density, %	Ln	Density, g/cm^3	Relative density, %
Pr	4.03	83	Pr	4.21	90
Sm	4.21	81	Sm	4.64	92
Gd	4.93	90	Gd	4.88	92
Dy	4.94	87	Dy	5.17	94
Er	5.34	90	Er	5.22	91

Note: theoretical density of Mg-doped ceramics was estimated assuming $(Ln_{0.95}Mg_{0.05})(V_{0.95}Mg_{0.05})O_{3.9}$ composition of the zircon phase and neglecting phase impurities.

Representative SEM images of $LnVO_4$ and $Ln_{0.95}V_{0.95}Mg_{0.10}O_{4-\delta}$ polycrystalline ceramic samples are given in fig. 2.8. The grain size varies in the range from 1 to 25-35 μm. Magnesium doping seems to promote the grain growth, probably due to the presence of trace amount of low-melting phase impurities.

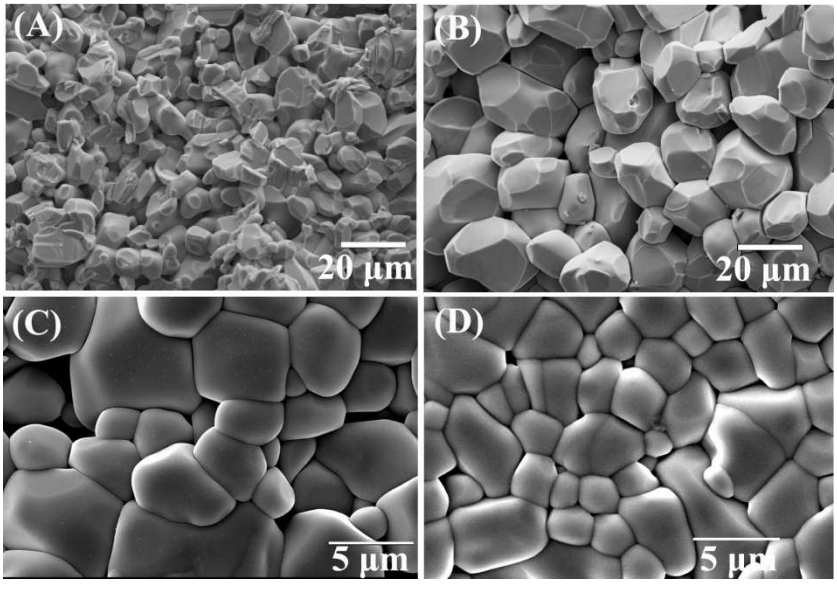

Figure 2.8. SEM micrographs: fractured (a) $PrVO_4$ and (b) $Pr_{0.95}V_{0.95}Mg_{0.10}O_{4-\delta}$ ceramics; polished and thermally etched surface of (c) $GdVO_4$ and (d) $Gd_{0.95}V_{0.95}Mg_{0.10}O_{4-\delta}$ ceramics.

2.2.2.2. Electrical properties

2.2.2.2.1. Impedance analysis

One of the most important studies that are used to characterize the bulk resistance of a crystalline solid material is A. C. conductivity measurements. Different techniques are employed for the measurement of A. C. conductivity. The most commonly used technique is the electrochemical impedance spectroscopy (EIS). EIS is a widely accepted tool to study the electrical properties of solid electrolytes and is used for understanding the grain, grain boundary and electrode contribution to the overall ionic conductivity with electronically conducting electrodes. This study also give information about the dynamics of mobile or bound charge carriers in the bulk or interfacial regions of any type of solid or liquid material such as ionic, semiconducting, mixed electronic-ionic and even insulators (dielectrics). EIS is a useful technique to investigate any intrinsic property that influences the conductivity of an electrode–materials system, or an external stimulus.[53] In EIS, the a.c. conductivity measurement is based on the studies made on the measurement of cell impedance over a range of temperatures and frequencies and analysing them in complex impedance plane (Cole-Cole plot or Nyquist plot).[54] EIS is also a useful method for the study of batteries, fuel cells, corrosion etc.

In general, the electric response of polycrystalline ceramic materials arises due to intra-grain, inter-grain and electrode effects. The movement of charges could be occurred by charge displacement, dipole reorientation, space charge formation, hoping and other mechanisms. For proper understanding of electrical properties of the given materials, the ceramic grain, the grain boundary and the electrode contributions must be separated. The inter-grain boundaries present in ceramic materials are defective regions as well as the place of segregated impurities or dopants. Hence, from the electrical point of view, it can be supposed that the grain bulk and the grain boundary regions have different dielectric as well as conductive properties. Apart from this, the ceramic region in contact with the

electrodes has to be “modified” with respect to the inner part of the bulk region: different Fermi levels of the two materials in contact will form Schottky barriers, imperfect conductivity of the electrodes creates a screening region varying the potential distribution in their neighbourhood and the metallic ions might diffuse in to the ceramic material creating a doped interface region. In any of these cases, the dielectric and conductive properties at the contact electrode-ceramics might be different with respect to the rest of the material. The complex impedance analysis method has confirmed as an effective tool for separating these contributions.[55]

In order to execute the electrical measurements to assess the electrochemical behaviour of electrode and/or electrolyte materials are typically prepared with cells having two identical electrodes applied to the faces of a samples in the form of a circular cylinder or rectangular parallelepiped. The common method is to apply a known voltage or current to the electrodes and observe the response. The most common and standard approach of EIS is to measure impedance by applying a single-frequency voltage or current to the interface and measuring the phase shift and amplitude, or real and imaginary parts, of the resulting current at that frequency by means of either analog circuit or fast Fourier transform (FFT) analysis of the response. Commercial instruments are accessible which measure the impedance as a function of frequency automatically in the frequency ranges of about 1 mHz to 1 MHz and are simply connected to laboratory microcomputers. In general, the parameters that can be derived from impedance spectra can be come in two categories: (a) those relevant only to the material itself, such as conductivity, dielectric constant, mobilities of charges, equilibrium concentrations of the charged species, and bulk generation–recombination rates; and (b) those relevant to an electrode–material interface, such as adsorption–reaction rate constants, capacitance of the interface region, and diffusion coefficient of neutral species in the electrode itself.[53]

Impedance spectroscopy is mainly characterized by the measurement and analysis of some or all of the four impedance-related functions: Impedance (Z), Admittance (Y), Modulus function (M), and Dielectric permittivity (ε) and the plotting of these functions in the complex plane. Impedance measurements usually creates numerical results, as real Z′ and imaginary Z″ impedances or modulus |Z| and phase angle θ as a function of frequency.[53].

$$Re\,(Z) \equiv Z' = |Z|\cos\theta \qquad 2.5$$

and

$$Im(Z) \equiv Z'' = |Z|sin\theta \qquad 2.6$$

With the phase angle

$$\theta = tan^{-1}(Z''/Z') \qquad 2.7$$

and the modulus

$$|Z| = [(Z')^2 + (Z'')^2]^{\frac{1}{2}} \qquad 2.8$$

EIS data for the electrochemical cells such as fuel cells are commonly represented in terms of Nyquist plots. Nyquist plot depicts the imaginary impedance (Z″), which is indicative of the capacitive and inductive character of the cell, versus the real impedance (Z′) of the cell. This type of graphical representation is also known as Cole-Cole plot or a complex impedance plane plot. Cole-Cole plots have the advantage that activation controlled processes with distinct time-constants appear as unique impedance arcs and the shape of the curve contributes insight into possible mechanism or governing phenomena.[56] Conventional EIS measures the Z as a function of ν or ω over a wide frequency range. Hence, from the resulting plot of Z(ω) vs ω response that one can determines information about the electrical properties of the full electrode–material system. Equivalent circuit modelling of the EIS data is used to extract physically reasonable properties of the electrochemical system by modelling the impedance data in

terms of an electrical circuit composed of components such as ideal resistors (R), capacitors (C) and inductors (L). Even though, real systems do not essentially behave ideally with processes occur distributed in time and space, specialized circuit elements can be used for equivalent circuit modelling.[53]

A typical Cole-Cole plot for the polycrystalline sample consists of three semicircular arcs. In ideal cases, the frequency response of electrical conductivity of the polycrystalline ceramics can be modelled by simple parallel RC circuit, with the resistor (R) corresponding to conduction and the capacitor (C) corresponding to the charge accumulation effects. But in some cases instead of capacitor, a constant phase element (CPE) is used to model the experimental data.[57,58] Since the capacitance values are related to the charge accumulation, by calculating the capacitance value associated with a particular arc will give an idea about where it happens, i.e., whether it is within the bulk of grains, in the grain boundaries or in the sample electrode surface. For grain conduction the capacitance values are in picofarads (pF) order whereas for grain boundary conduction the capacitance values falls in the nanofarads (nF). In latter case there are bigger chances of charge polarization and therefore the relaxation associated with grain boundaries falls in lower frequency region whereas for grains relaxation happens in higher frequencies.[58] With respect to the range of measurement frequency and the difference in relaxation frequencies between grain and grain boundary phenomena, the semicircle may appear as merged or incomplete. The intercept of an impedance semicircle with the real axis would yield the ohmic resistances such as grain resistance (R_g) and grain boundary resistance (R_{gb}) offered by the material against the conduction process associated with it. Total resistance (R_T) can be calculated from the sum of grain and grain boundary resistances.

$$R_T = R_g + R_{gb} \qquad 2.9$$

The total conductivity can be calculated from the sample thickness (l) and the electroding area (A) using the equation

$$\sigma = \frac{l}{R_T A} \qquad 2.10$$

As the grain and grain boundary semicircles were not always well-resolved, only their total resistance was considered for calculating the conductivity at different temperatures. The temperature dependence of conductivity can be described generally by the Arrhenius equation (Eq. (1.3) Chapter 1).

Electrical conductivity in air

Fig. 2.9 demonstrates typical examples of impedance spectra of $LnVO_4$-based ceramics in air. For all compositions, impedance spectra comprised two major contributions. High-frequency semicircle was assigned to the bulk resistance, while low-frequency contribution with estimated capacitance of order of μF/cm was attributed to the electrode process. The presence of electrode semicircle implies an ionic contribution to the electrical transport in these orthovanadates.

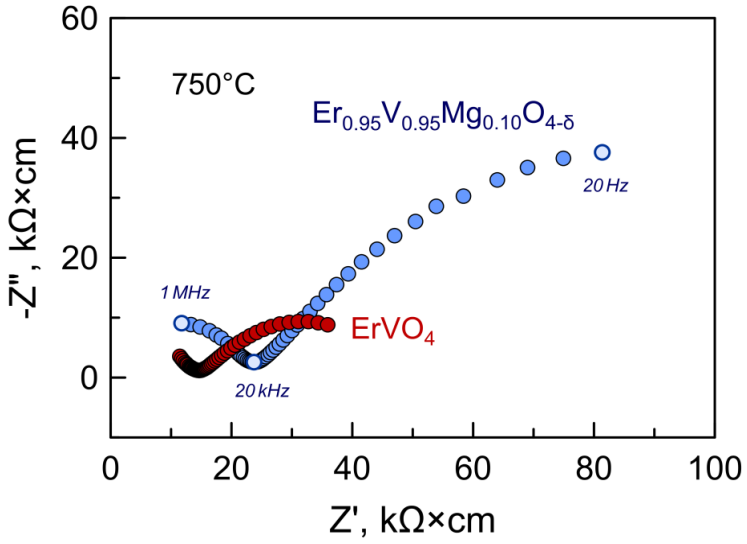

Figure 2.9: Impedance spectra of $ErVO_4$ and $Er_{0.95}V_{0.95}Mg_{0.10}O_{4-\delta}$ collected in air at 750°C.

Temperature dependence of electrical conductivity of the prepared samples was studied and is shown in fig. 2.10. All studied materials exhibit semiconducting behaviour

in air (fig. 2.10); the values of activation energy of electrical conductivity are listed in Table 2.4. Activation energies for the samples were calculated using Arrhenius equation. $PrVO_4$ and $SmVO_4$ ceramics show the highest conductivity in the studied temperature range. Also, the conductivity of praseodymium orthovanadate ceramics measured in this work is ~2 orders of magnitude higher compared to the values reported for $PrVO_4$ single crystals.[59]

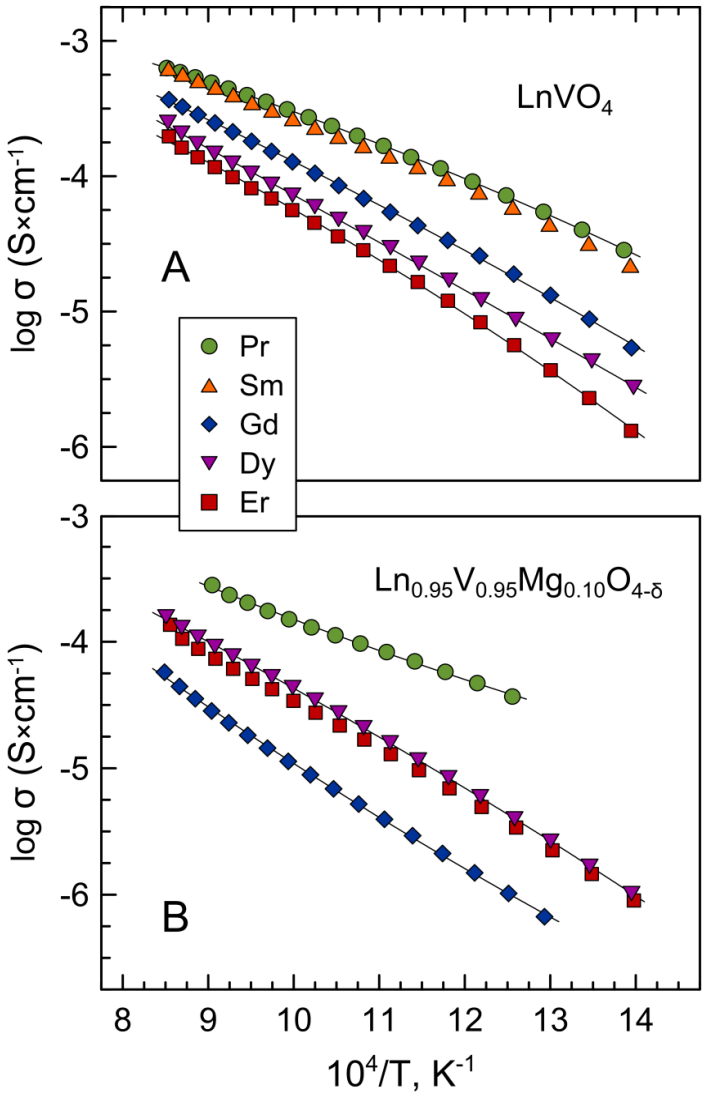

Figure 2.10. Temperature dependence of electrical conductivity of (A) $LnVO_4$ and (B) $Ln_{0.95}V_{0.95}Mg_{0.10}O_{4-\delta}$ ceramics in air.

The conductivity decreases with increasing atomic number of rare-earth cation in the series Gd – Dy – Er. Doping with magnesium results in a drop of electrical

conductivity, by 1.5-2 times in most cases. Noteworthy, for both series of compositions, the activation energy tends to increase with decreasing σ values (Table 2.4).

Table 2.4: Activation energy of electrical conductivity of $LnVO_4$-based ceramics in air

$LnVO_4$			$Ln_{0.95}V_{0.95}Mg_{0.10}O_{4-\delta}$		
Ln	T, °C	E_A, kJ×mol^{-1}	Ln	T, °C	E_A, kJ×mol^{-1}
Pr	450-900	55.1 ± 0.5	Pr	520-850	53.1 ± 0.5
Sm	440-900	57.7 ± 0.4	Sm	-	-
Gd	445-900	75.8 ± 0.3	Gd	500-900	89.0 ± 0.9
Dy	440-900	74.9 ± 0.3	Dy	440-900	83.3 ± 0.5
Er	440-900	81.8 ± 0.8	Er	440-900	82.0 ± 0.5

Note: Activation energy was calculated using Arrhenius model $\sigma = \frac{A_0}{T}\exp\left(-\frac{E_A}{RT}\right)$; given errors are standard errors.

2.2.2.2.2. Modified e.m.f. technique for the measurement of oxygen ion transference number

The classical e.m.f. technique is based on the measurement of the open-circuit voltage of a cell having a membrane with two reversible electrodes and placed under a chemical potential gradient. For an oxygen concentration cell with negligible polarization resistance of electrodes, the average oxygen ion transference number ($\overline{t_O}$) can be calculated from the ratio of the measured e.m.f. (E_{exp}) to theoretical Nernst voltage (E_{th}).[60,61]

$$\overline{t_O} = \frac{E_{exp}}{E_{th}} \qquad 2.11$$

Where

$$E_{th} = \frac{RT}{4F}\ln\frac{p_2}{p_1} \qquad 2.12$$

p_1 and p_2 are the values of oxygen partial pressure, $p(O_2)$, at the electrodes and E_{th} was determined using YSZ oxygen sensor. The electrode polarization can cause experimental errors in the determination of the ion transference numbers by the e.m.f. method. [60,61]

Most of the errors can be avoided by a proper selection of experimental set-up and working conditions, non-negligible polarization resistance of the electrodes signifies a more serious problem, particularly at reduced temperatures, in cases of reaction between electrode and electrolyte materials, and at low partial pressures of electrochemically active components.[60]

In order to prevent an effect of the electrode polarization resistance on measured transference numbers, Gorelov's modification of the e.m.f. method was employed, which refers to studying e.m.f. of the concentration cells as a function of resistance of the external load closing the circuit.[44,62] Gorelov[43] proved that the electrode polarization resistance affects the measured e.m.f. of electrochemical cells with mixed ionic-electronic conductors, as illustrated by fig. 2.11 (A). The electric current (I) flowing through such a cell can be expressed by the formula:

$$I = \frac{E_{th} - \eta}{R_o + R_e} = \frac{E_{exp}}{R_e} \qquad 2.13$$

where η is the sum of the electrode overpotentials, R_o and R_e are the partial oxygen ionic and electronic resistances of the mixed conductors, respectively.

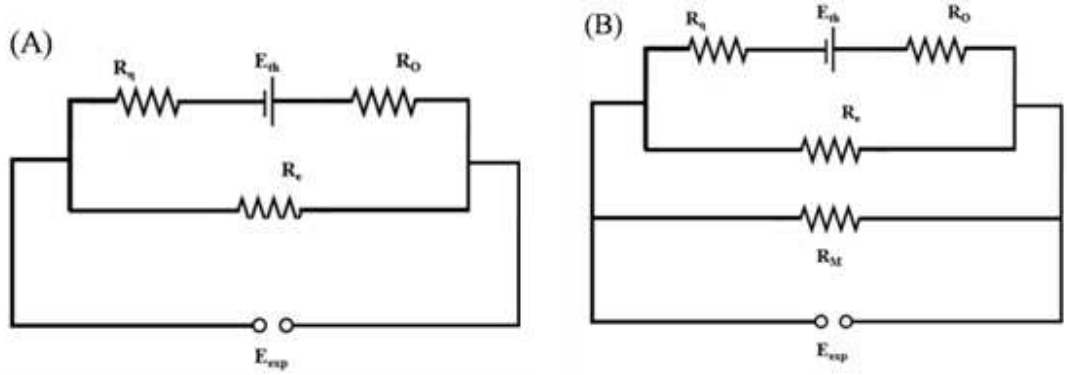

Figure 2.11: Equivalent circuit of (A) a mixed conductor placed under oxygen chemical potential gradient, and (B).the cell for the transference number measurements

At lower overpotentials, when the overpotential – current dependence is linear

$$\eta = IR_\eta \qquad 2.14$$

where R_η is the total polarization resistance.

Oxygen transference number can be expressed using the quantities R_o and R_e as

$$\overline{t_O} = \frac{\sigma_O}{\sigma_O+\sigma_e} = \frac{R_e}{R_O+R_e} \quad 2.15$$

where σ_O and σ_e are the partial oxygen ionic and electronic conductivities respectively. By substituting equations 2.15 and 2.14 into 2.13 it is found that

$$E_{exp} = \overline{t_O} \cdot E_{th} \cdot \left[1 + \frac{R_\eta}{R_O+R_e}\right]^{-1} \quad 2.16$$

So the determination of oxygen transference number of mixed ionic-electronic conductors as a ratio of measured and theoretical e.m.f. values may result in the underestimated ion transference number values due to the presence of the electrode polarization resistance. Gorelov[43] proposed to connect a variable resistor to the electrodes as illustrated in fig. 2.11 (B) and to study the e.m.f. as a function of its resistance (R_M). In this approach

$$\frac{E_{th}}{E_{exp}} - 1 = \left(R_O + R_\eta\right) \cdot \left[\frac{1}{R_e} + \frac{1}{R_M}\right] \quad 2.17$$

Thus, the value of R_e can be calculated from a linear dependence fit.

$$\frac{E_{th}}{E_{exp}} - 1 = A \cdot \left(\frac{1}{R_M}\right) + B \quad 2.18$$

Where A and B are the regression parameters,

$$A = R_O + R_\eta \quad 2.19$$

$$B = \frac{R_O+R_\eta}{R_e} = \frac{A}{R_e} \quad 2.20$$

One should notice that

$$R_e = \frac{A}{B} \quad 2.21$$

Therefore, the oxygen ion transference number were calculated as

$$\overline{t_O} = 1 - t_e = 1 - \frac{R_{total}}{R_e} \quad 2.22$$

where t_e is the electron transference number, and R_{total} is the overall resistance of the sample measured independently by impedance spectroscopy.[44,60-62]

In the present case, for determining the nature of electrical transport in the studied orthovanadates, oxygen-ion transference numbers of selected compositions were studied by the modified e.m.f. technique. The results (Table 2.5) indicate that both undoped $LnVO_4$ and magnesium-doped orthovanadates are predominantly oxygen-ionic conductors under oxidizing conditions. Note that studied $LnVO_4$ are expected to be oxygen stoichiometric (except probably $PrVO_4$), with all regular oxygen sites in zircon structure occupied.

Table 2.5: Average oxygen-ion transference numbers determined by the modified e.m.f. technique, ($p(O_2)$ gradient: 1.00 atm/0.21 atm).

Composition	T, °C	$\overline{t_O}$
$PrVO_4$	900	0.67
	800	0.72
$Pr_{0.95}V_{0.95}Mg_{0.10}O_{4-\delta}$	900	0.985
	800	0.978
$SmVO_4$	900	0.982
	800	0.981

Li et al. studied related zircon-type $EuVO_4$ and assumed that oxygen ions may diffuse through interstitial sites along c axis between the chains formed by alternating edge-sharing EuO_8 dodecahedra and VO_4 tetrahedra.[63] Interstitial mechanism for the oxygen diffusion in the structural prototype, zircon $ZrSiO_4$, is supported by the theoretical calculations.[64] Oxygen transport via interstitial diffusion mechanism was also suggested for zircon-type $CeVO_{4+\delta}$ and $Ce_{1-x}A_xVO_{4+\delta}$ (A = Ca, Sr) orthovanadates.[29,65] Cerium orthovanadate-based phases are believed however to be oxygen overstoichiometric; oxygen excess is formed to compensate the affinity of cerium cations to 4^+ oxidation state

under oxidizing conditions and is accommodated in the form of interstitial oxygen ions. Similar situation can be expected for $PrVO_4$ orthovanadate as praseodymium has mixed 3+/4+ oxidation state in the binary oxides in air at temperatures below 1200°C ([66] and references therein). This would explain also relatively high electronic contribution (Table 2.5) to the total conductivity of this material assuming that electronic transport occurs via electron-hole hopping between Pr^{3+} and Pr^{4+} cations. In the case of other $LnVO_4$ (Ln = Sm, Gd, Dy and Er) orthovanadates, the formation of interstitial oxygen ions may be expected to occur via intrinsic Frenkel disorder (using Kröger-Vink notation):

$$O_O^{\times} \xleftrightarrow{K_F} V_O^{\bullet\bullet} + O_i'' \qquad 2.23$$

where K_F is the temperature-dependent equilibrium constant. On the other hand, substitution by magnesium in either sublattice should be compensated by formation of oxygen vacancies:

$$2[Mg_{Ln}'] = [V_O^{\bullet\bullet}] \qquad 2.24$$

$$2[Mg_V'''] = 3[V_O^{\bullet\bullet}] \qquad 2.25$$

thus shifting the equilibrium in Eq.(2.23) to the left and suppressing the formation of mobile interstitial oxygen ions. This can reasonably explain the drop of conductivity in magnesium-doped ceramics assuming that mobility of oxygen vacancies in zircon-type structure of $LnVO_4$ is lower compared to that of interstitial oxygen.

Effect of oxygen partial pressure on electrical transport

Fig. 2.12 shows total conductivity of selected $LnVO_4$-based ceramics measured in atmospheres with different oxygen partial pressure. It turns out that the studied materials may exhibit different dependence of electrical conductivity on $p(O_2)$ determined by the concentration of dominant point defects in the zircon lattice. The behavior of $PrVO_4$ ceramics seems to support the hypothesis that the average oxidation state of

praseodymium cations in this material is higher than 3+ and that this orthovanadate is slightly oxygen overstoichiometric. Reducing $p(O_2)$ results in a decrease of total electrical conductivity (fig. 2.12A) caused, most likely by reduction of Pr cations and oxygen release from the lattice:

$$2[Pr_{Pr}^{\bullet}] + [O_i''] \leftrightarrow 2[Pr_{Pr}^{\times}] + 0.5O_2 \qquad 2.26$$

(where $Pr_{Pr}^{\bullet} \equiv Pr^{4+}$ and $Pr_{Pr}^{\times} \equiv Pr^{3+}$) leading to a decrease of concentrations of both electronic and ionic charge carriers. On the contrary, oxygen release from the $Pr_{0.95}V_{0.95}Mg_{0.10}O_{4-\delta}$ lattice is expected to increase the concentrations of oxygen vacancies and *n*-type electronic charge carriers:

$$O_O^{\times} \leftrightarrow V_O^{\bullet\bullet} + 0.5O_2 + 2e' \qquad 2.27$$

and results in a minor increase of total electrical conductivity when oxygen partial pressure is reduced. Note that the results on oxygen-ion transference numbers and $p(O_2)$ dependencies of electrical conductivity seems to indicate that, contrary to $PrVO_4$, praseodymium cations in Mg-doped $Pr_{0.95}V_{0.95}Mg_{0.10}O_{4-\delta}$ remains in 3+ oxidation state; available data are however insufficient to explain this difference.

Contrary to $PrVO_4$, total electrical conductivity of $SmVO_4$ remains essentially independent of oxygen partial pressure in the studied $p(O_2)$ range (fig. 2.12C). On the one hand, Sm cations has stable oxidation state 3+, and variations of oxygen partial pressure may have comparatively minor effect of the concentration of defects in this compound in the studied range of conditions. On the other hand, a minor increase of electronic conductivity on reducing $p(O_2)$ (Eq.(2.27)) may be compensated by a simultaneous minor decrease of ionic conductivity due to the shift of equilibrium of reaction Eq.(2.23) to the left. Whatever the mechanism, total electrical conductivity of $SmVO_4$ remains unchanged, within the limits of experimental uncertainty.

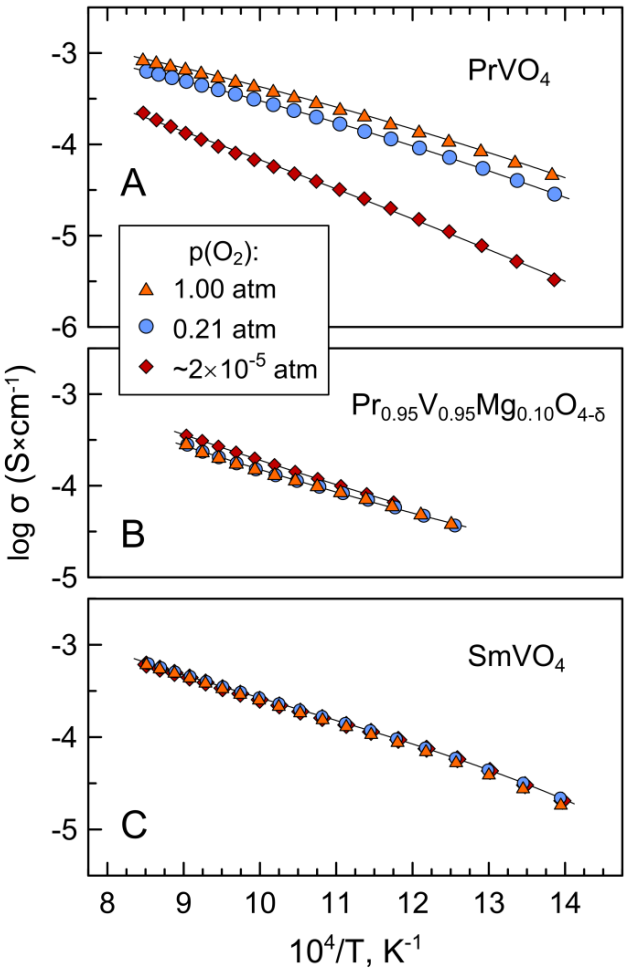

Figure 2.12: Temperature dependence of electrical conductivity of (A) $PrVO_4$, (B) $Pr_{0.95}V_{0.95}Mg_{0.10}O_{4-\delta}$ and (C) $SmVO_4$ ceramics in controlled atmospheres with different oxygen partial pressure.

Assessment of possible protonic contribution

As mentioned in introduction chapter (section 1.4.1), acceptor-doped $La_{0.99}Ca_{0.01}VO_{4-\delta}$ orthovanadate with monazite-type structure was reported to be a pure ionic conductor under oxidizing conditions, with protonic conductivity dominating in the low-temperature range under wet conditions.[67]

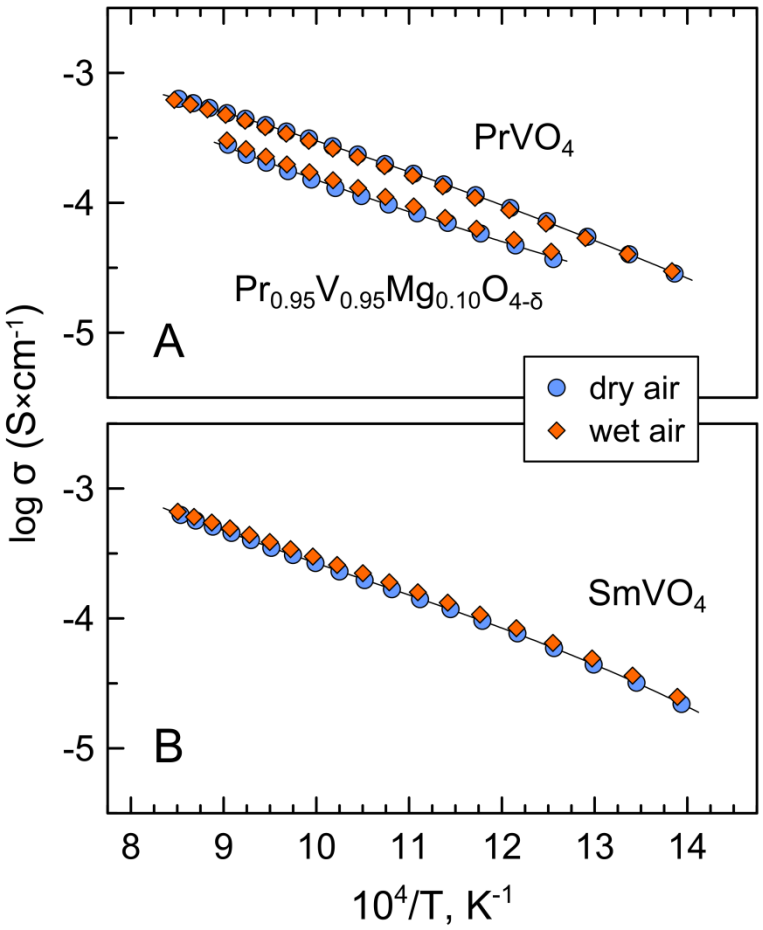

Figure 2.13. Electrical conductivity of $PrVO_4$ (A), $Pr_{0.95}V_{0.95}Mg_{0.10}O_{4-\delta}$ (A) and $SmVO_4$ (B) ceramics measured in dry and wet air. $p(H_2O)$ in dry and wet atmospheres was $\leq 3\times10^{-3}$ and $\sim2.8\times10^{-2}$ atm, respectively.

Therefore, in the present study, electrical conductivity of selected orthovanadates was studied comparatively under dry and wet air in order to identify possible protonic contribution to the total electrical transport in these ceramic materials. It was found that, contrary to $La_{0.99}Ca_{0.01}VO_{4-\delta}$, humidity has rather negligible effect of the transport properties of the studied $LnVO_4$-based zircons (fig. 2.13). Electrical conductivity of $PrVO_4$ remained essentially unchanged in both dry and wet air at 450-900°C (fig. 2.13A). Minor increase, ~10%, of electrical conductivity was observed in the case of $Pr_{0.95}V_{0.95}Mg_{0.10}O_{4-\delta}$ (fig. 2.13A) and $SmVO_4$ (fig. 2.13B) at temperatures < 800°C.

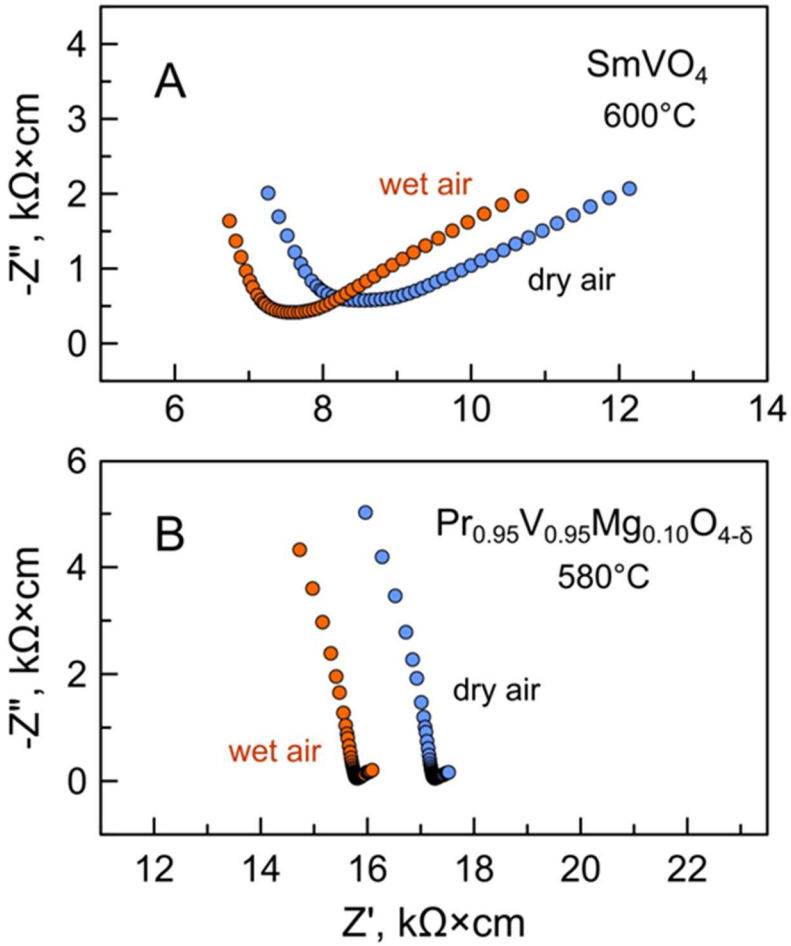

Figure 2.14. Comparison of impedance spectra of (A) $SmVO_4$ and (B) $Pr_{0.95}V_{0.95}Mg_{0.10}O_{4-\delta}$ ceramics collected in dry and wet air.

Fig. 2.14 illustrates examples of impedance spectra collected in dry and wet atmospheres. The impedance spectra for the samples $SmVO_4$ and $Pr_{0.95}V_{0.95}Mg_{0.10}O_{4-\delta}$ are shown. Thus, protonic transport has rather negligible contribution to the total electrical conductivity of the studied orthovanadates under applied conditions.

2.2.3. Conclusions

- Undoped $LnVO_4$ and Mg-doped $Ln_{0.95}V_{0.95}Mg_{0.10}O_{4-\delta}$ (Ln = Pr, Sm, Gd, Dy, Er) orthovanadates were prepared by solid state reaction method.
- XRD analysis showed the formation of single-phase materials with tetragonal zircon-type structure.
- SEM/EDS studies of doped ceramics revealed the presence of inclusions of MgO and Mg-V-O phases indicating that solid solubility of magnesium cations in $LnVO_4$ lattice is below the doping level and that magnesium cations prefer to substitute into vanadium sublattice.
- All orthovanadates show semiconducting behavior at 450-900°C under oxidizing conditions.
- The results of transference numbers measurements indicate that the studied materials are predominantly oxygen-ion conductors, except $PrVO_4$ which is a mixed ionic-electronic conductor.
- In $LnVO_4$ series, electrical conductivity is highest for $PrVO_4$ and $SmVO_4$ and decreases with increasing atomic number of rare-earth cation for other compositions.
- Additions of magnesium results in a drop of electrical conductivity, by 1.5-2 times for most of compositions.
- Interstitial oxygen diffusion is suggested as a prevailing mechanism of ionic transport in undoped $LnVO_4$, whilst acceptor-type magnesium doping suppresses the formation of interstitial oxygen ions.
- Humidified atmosphere has rather negligible impact on the electrical properties of substituted ceramics, indicating only minor (if any) protonic contribution to the total electrical transport of the studied orthovanadates.

2.3. References

[1] I. Abrahams, F. Krok, Defect chemistry of the BIMEVOXes, *J. Mater. Chem.* 12 (2002) 3351–3362.

[2] T. Esaka, R. Tachibana, S. Takai, Oxide ion conduction in the Sm-substituted $PbWO_4$ phases, *Solid State Ionics*. 92 (1996) 129–133.

[3] N. Jalarvo, O. Gourdon, Z. Bi, D. Gout, M. Ohl, M. P. Paranthaman, Atomic-scale picture of the ion conduction mechanism in a tetrahedral network of lanthanum barium gallate, *Chem. Mater.* 25 (2013) 2741–2748.

[4] Q. F. Fang, F. J. Liang, X. P. Wang, G. G. Zhang, Z. J. Cheng, Anelastic and dielectric studies of $La_2Mo_2O_9$-based oxide-ion conductors, *Mater. Sci. Eng. A.* 442 (2006) 43–48.

[5] R. V. Kumar, Application of rare earth containing solid state ionic conductors in electrolytes, *J. Alloys Compd.* 250 (1997) 501–509.

[6] P. Lacorre, The LPS concept, a new way to look at anionic conductors, *Solid State Sci.* 2 (2000) 755–758.

[7] V. V. Kharton, F. M. B. Marques, A. Atkinson, Transport properties of solid oxide electrolyte ceramics: a brief review, *Solid State Ionics.* 174 (2004) 135–149.

[8] A. Najib, J. E. H. Sansom, J. R. Tolchard, P. R. Slater, M. S. Islam, Doping strategies to optimise the oxide ion conductivity in apatite-type ionic conductors., *Dalton Trans.* 19 (2004) 3106–3109.

[9] S. Mahapatra, G. Madras, T. N. G. Row, Synthesis, characterization and photocatalytic activity of lanthanide (Ce, Pr and Nd) orthovanadates, *Ind. Eng. Chem. Res.* 46 (2007) 1013–1017.

[10] B. C. Chakoumakos, M. M. Abraham, L. A. Boatner, Crystal structure refinements of zircon- type MVO_4 (M=Sc, Y , Ce, Pr, Nd, Tb, Ho, Er, Tm, Yb, Lu), *J. Solid State Chem.* 109 (1994) 197–202.

[11] D. Errandonea, R. Perales, J. Fuertes, A. Segura, S. N. Achary, A. K. Tyagi, High-pressure structural investigation of several zircon-type orthovanadates, *Phys. Rev. B.* B 79 (2009) 184104.

[12] A. B. Garg, K. V. Shanavas, B. N. Wani, S. M. Sharma, Phase transition and possible metallization in $CeVO_4$ under pressure, *J. Solid State Chem.* 203 (2013) 273–280.

[13] V. Panchal, S. Moreno, D. Perez, D. Errandonea, F. J. Manjon, P. Hernandez, A. Muñoz, S. N. Achary, A. K. Tyagi, Zircon to monazite phase transition in $CeVO_4$: X-ray diffraction and Raman-scattering measurements, *Phys. Rev. B.* B84 (2011) 024111.

[14] V. Panchal, D. Errandonea, A. Segura, P. Hernandez, A. Muñoz, S. Moreno, M. Bettinelli, The electronic structure of zircon-type orthovanadates: Effects of high-pressure and cation substitution, *J. Appl. Phys.* 110 (2011) 043723.

[15] N. Deligne, V. Gonze, D. Bayot, M. Devillers, Yttrium, lanthanide and mixed Y-Ln vanadates prepared from molecular precursors based on EDTA, *Eur. J. Inorg. Chem.* 2008 (2008) 896–902.

[16] E. V. Tsipis, V. V. Kharton, N. P. Vyshatko, A. L. Shaula, J. R. Frade, Stability and oxygen ionic conductivity of zircon-type $Ce_{1-x}A_xVO_{4+\delta}$ (A=Ca, Sr), *J. Solid State Chem.* 176 (2003) 47–56.

[17] M. Dorogova, A. Navrotsky, L. A. Boatner, Enthalpies of formation of rare earth orthovanadates, $REVO_4$, *J. Solid State Chem.* 180 (2007) 847–851.

[18] X. Cheng, D. Guo, S. Feng, K. Yang, Y. Wang, Y. Ren, Y. Song, Structure and stability of monazite- and zircon-type $LaVO_4$ under hydrostatic pressure, *Opt. Mater.* 49 (2015) 32–38.

[19] C. T. G. Petit, R. Lan, P. I. Cowin, A. Kraft, S. Tao, Structure, conductivity and redox stability of solid solution $Ce_{1-x}Ca_xVO_4$ ($0 \leq x \leq 0.4125$), *J. Mater. Sci.* 46 (2011) 316–326.

[20] C. T. G. Petit, R. Lan, P. I. Cowin, S. Tao, Structure and conductivity of strontium-doped cerium orthovanadates $Ce_{1-x}Sr_xVO_4$ ($0 \leq x \leq 0.175$), *J. Solid State Chem.* 183 (2010) 1231–1238.

[21] C. Yu, M. Yu, C. Li, C. Zhang, P. Yang, J. Lin, Spindle-like lanthanide orthovanadate nanoparticles: Facile synthesis by ultrasonic irradiation, characterization, and luminescent properties, *Cryst. Growth Des.* 9 (2009) 783–791.

[22] R. J. Finch, J. M. Hanchar, Structure and chemistry of Zircon and Zircon-group minerals, *Rev. Mineral. Geochemistry.* 53 (2003) 1–25.

[23] M. Yi, S. Park, C. Seong, Y. Piao, T. Yu, The general synthesis and characterization of rare earth orthovanadate nanocrystals and their electrochemical applications, *J. Alloy. Compd.* 693 (2017) 825–831.

[24] H. Zhan, J. Shu, X. Wei, K. Wang, J. Chen., Cerium vanadate nanoparticles as a new anode material for lithium ion batteries, *RSC Adv.* 3 (2013) 7403–7407.

[25] L. Adijanto, V. B. Padmanabhan, K. J. Holmes, R. J. Gorte, J. M. Vohs, Physical and electrochemical properties of alkaline earth doped, rare earth vanadates, *J. Solid State Chem.* 190 (2012) 12–17.

[26] L. Adijanto, V. B. Padmanabhan, K. Rainer, R. J. Gorte, J. M. Vohs, Transition metal-doped rare earth vanadates : A regenerable catalytic material for SOFC anodes, *J. Mater. Chem.* 22 (2012) 11396–11402.

[27] N. Danilovic, J. Luo, K.T. Chuang, A. R. Sanger, $Ce_{0.9}Sr_{0.1}VO_x$ (x=3, 4) as anode materials for H_2S-containing CH_4 fueled solid oxide fuel cells, *J. Power Sources.* 192 (2009) 247–257.

[28] T. H. Gayathri, A. A. Yaremchenko, K. Zakharchuk, J. James, Effect of magnesium addition on the structural , microstructural and electrical properties of YVO_4, *J. Alloy. Compd.* 672 (2016) 549–557.

[29] E. V. Tsipis, M. V. Patrakeev, V. V. Kharton, N. P. Vyshatko, J. R. Frade, Ionic and p-type electronic transport in zircon-type $Ce_{1-x}A_xVO_{4\pm\delta}$ (A = Ca, Sr), *J. Mater. Chem.* 12 (2002) 3738–3745.

[30] C. Peng, J. Luo, A. R. Sanger, K. T. Chuang, Sulfur-tolerant anode catalyst for solid oxide fuel cells operating on H_2S-containing syngas, *Chem. Mater.* 22 (2010) 1032–1037.

[31] J. W. Fergus, Oxide anode materials for solid oxide fuel cells, *Solid State Ionics.* 177 (2006) 1529–1541.

[32] J. B. Goodenough, Y. Huang, Alternative anode materials for solid oxide fuel cells, *J. Power Sources.* 173 (2007) 1–10.

[33] A. Watanabe, Highly conductive oxides, $CeVO_4$, $Ce_{1-x}M_xVO_{4-0.5x}$ (M=Ca, Sr, Pb) and $Ce_{1-y}Bi_yVO_4$, with Zircon-type structure prepared by solid-state reaction in air, *J. Solid State Chem.* 153 (2000) 174–179.

[34] C. T. G. Petit, R. Lan, P. I. Cowin, J. T. S. Irvine, S. Tao, Novel redox reversible oxide, Sr-doped cerium orthovanadate to metavanadate, *J. Mater. Chem.* 21 (2011) 525–531.

[35] N. S. Rao, O. G. Palanna, Electrical, thermal and infrared studies of cerium(Ill) orthovanadate, *Bull. Mater. Sci.* 18 (1995) 593–597.

[36] N. H. Zainol, S. M. Samin, L. Othman, K. B. Isa, W. G. Chong, Z. Osman, Magnesium ion-based gel polymer electrolytes: Ionic conduction and infrared spectroscopy studies, *Int. J. Electrochem. Sci.* 8 (2013) 3602–3614.

[37] G. C. Yin, H. Yin, L. H. Zhong, M. L. Sun, J. K. Zhang, X. J. Xie, et al., Crystal structure and ionic conductivity of Mg-doped apatite-type lanthanum silicates $La_{10}Si_{6-x}Mg_xO_{27-x}$ (x = 0–0.4), *Chin. Phys. B.* 23 (2014) 048202

[38] T. Kinoshita, T. Iwata, E. Béchade, O. Masson, I. Julien, E. Champion, et al., Effect of Mg substitution on crystal structure and oxide-ion conductivity of apatite-type lanthanum silicates, *Solid State Ionics*. 181 (2010) 1024–1032.

[39] M. Li, M. J. Pietrowski, R. A. De Souza, H. Zhang, I. M. Reaney, S. N. Cook, et al., A family of oxide ion conductors based on the ferroelectric perovskite $Na_{0.5}Bi_{0.5}TiO_3$, *Nature Materials* 13 (2014) 31–35.

[40] N. Jaiswal, D. Kumar, S. Upadhyay, O. Parkash, Effect of Mg and Sr co-doping on the electrical properties of ceria-based electrolyte materials for intermediate temperature solid oxide fuel cells, *J. Alloy. Compd.* 577 (2013) 456–462.

[41] F. Wang, S. Chen, Q. Wang, S. Yu, S. Cheng, Study on Gd and Mg co-doped ceria electrolyte for intermediate temperature solid oxide fuel cells, *Catal. Today* 97 (2004) 189–194.

[42] X. Zhao, X. Li, N. Xu, K. Huang, Beneficial effects of Mg-excess in $La_{1-x}Sr_xGa_{1-y}Mg_{y+z}O_{3-\delta}$ as solid electrolyte, *Solid State Ionic.* 214 (2012) 56–61.

[43] V. P. Gorelov, Transport number determinations in ionic conductors using EMF measurements with active load, *Sov. Electrochem.* 24 (1988) 1380–1381.

[44] V. V. Kharton, A. A. Yaremchenko, A. P. Viskup, G. C. Mather, E. N. Naumovich, F. M. B. Marques, Ionic and p-type electronic conduction in $LaGa(Mg,Nb)O_{3-\delta}$ perovskites, *Solid State Ionics*. 128 (2000) 79–90.

[45] B.D. Cullity, Elements of X-ray Diffraction, Addison-Wesley, 1956.

[46] R. D. Shannon, Revised effective ionic radii and systematic studies of interatomic distances in halides and chalcogenides, *Acta Cryst.* A32 (1976) 751–767.

[47] B. H. Toby, R factors in Rietveld analysis: How good is good enough?, *Powder Diffr*. 21 (2006) 67–70.

[48] L. B. McCusker, R. B. V. Dreele, D. E. Cox, D. Loue, P. Scardi, Rietveld refinement guidelines, *J. Appl. Cryst.* 32 (1999) 36–50.

[49] P. Abhilash, M. T. Sebastian, S. K. Peethambharan, Structural, thermal and dielectric properties of rare earth substituted eulytite for LTCC applications, *J. Eur. Ceram. Soc.* 36 (2016) 1939-1944.

[50] L. Reimer, Scanning Electron Microscopy, Physics of Image Formation and Microanalysis, Springer, 1998.

[51] E. I. Speranskaya, *Izv. Akad. Nauk. SSSR, Neorg. Mater*. 7 (1971) 1804–1807.

[52] A. A. Fotiev, B. V. Slobodin, M. Y. Khodos, Vanadates. Composition, synthesis, structure, properties, Moscow, Nauka, 1988.

[53] E. Barsoukov, J. R. Macdonald, Impedance Spectroscopy Theory, Experiment, and Applications, Wiley, 2005.

[54] R. P. Suvarna, K. R. Rao, K. Subbarangaiah, A simple technique for a. c. conductivity measurements, *Bull. Mater. Sci.* 25 (2002) 647–651.

[55] L. Mitoseriu, C. E. Ciomaga, I. Dumitru, L. P. Curecheriu, F. Prihor, A. Guzu, Study of the frequency-dependence of the complex permittivity in $Ba(Zr,Ti)O_3$

ceramics: evidences of the grain boundary phenomena, *J. Optoelectron. Adv. Mater.* 10 (2008) 1843–1846.

[56] M.E. Orazem, B. Tribollet, Electrochemical Impedance Spectroscopy,Wiley, 2008.

[57] Y. K. Yadav, M. P. K. Sahoo, R. N. P. Choudhary, Electrical properties of Bi_2TiO_5 ceramic, *J. Alloy. Compd*. 490 (2010) 589–593.

[58] Z. Liu, J. Ouyang, K. Sun, Improvement of electrical conductivity of trivalent rare-earth cation-doped neodymium zirconate by co-doping gadolinium and ytterbium, *Fuel Cells*. 10 (2010) 1050–1056.

[59] Y. P. Yadava, R. A. Singh, B. M. Wanklyn, Electrical conduction in $PrVO_4$ single crystal, *J. Mater. Sci. Lett.* 4 (1985) 224–226.

[60] V.V. Kharton, F.M.B. Marques, Interfacial effects in electrochemical cells for oxygen ionic conduction measurements I. The e.m.f. method, *Solid State Ionics.* 140 (2001) 381–394.

[61] J. Martínez, D. López, J. C. Morales, P. Núñez, Determination of the ionic transport numbers of lanthanum gallate materials by impedance spectroscopy and modified EMF method, *Bol. Soc. Esp. Ceram. V.* 47 (2008) 153–158.

[62] A. A. Yaremchenko, V. V. Kharton, E. N. Naumovich, F. M. B. Marques, Physicochemical and transport properties of BICUVOX-based ceramics, *J. Electroceramics*. 4 (2000) 233–242.

[63] L. Li, G. Li, Y. Xue, H. Inomata, Structure, luminescence, and transport properties of $EuVO_4$, *J. Electrochem. Soc*. 148 (2001) J45–J49.

[64] J. P. Crocombette, Theoretical study of point defects in crystalline zircon, *Phys. Chem. Miner.* 27 (1999) 138–143.

[65] E. V. Tsipis, V. V. Kharton, N. P. Vyshatko, A. L. Shaula, J. R. Frade, Stability and oxygen ionic conductivity of zircon-type $Ce_{1-x}A_xVO_{4+\delta}$ (A=Ca, Sr), *J. Solid State Chem.* 176 (2003) 47–56.

[66] A. Netz, W. F. Chu, V. Thangadurai, R. A. Huggins, W. Weppner, Investigations of praseodymium oxide electrodes in lithium concentration cells, *Ionics* 5 (1999) 426–433.

[67] M. Huse, T. Norby, R. Haugsrud, Proton conductivity in acceptor-doped $LaVO_4$, *J. Electrochem. Soc.* 158 (2011) B857–B865.

CHAPTER 3

IMPACT OF MAGNESIUM SUBSTITUTION ON ELECTRICAL TRANSPORT PROPERTIES OF ZIRCON-TYPE $EuVO_4$

Magnesium-substituted europium vanadate ceramics, $Mg_xEuVO_{4\pm\delta}$ (x = 0-0.5), were prepared by solid state method and characterized by XRD, SEM/EDS, dilatometry, UV-visible spectroscopy, impedance spectroscopy, and measurements of oxygen-ion transference numbers ($\overline{t_O}$). Magnesium was found to substitute preferentially into vanadium sublattice of zircon-type $EuVO_4$ with limited solubility of 5 at.%. Additions of magnesium increase slightly coefficients of thermal expansion (3.2-6.0 ppm/K at 150-400°C) and have a negligible effect on the optical properties. Undoped $EuVO_4$ is predominantly an oxygen-ionic conductor with $\overline{t_O}$ = 0.96-0.99 at 700-900°C under oxidizing conditions. Acceptor-type substitution suppresses total conductivity and oxygen-ionic transport. The variations of electrical transport properties are discussed in terms of interstitial oxygen diffusion in parent $EuVO_4$ and oxygen vacancy diffusion in Mg-substituted vanadate. Humidified atmosphere has a negligible impact on the electrical properties of substituted ceramics but results in increased electrical conductivity of $EuVO_4$ indicating a protonic contribution to the total electrical transport.

T. H. Gayathri, A. A. Yaremchenko, K. Zakharchuk, P. Abhilash, S. Ananthakumar "Impact of acceptor-type substitution on electrical transport properties of zircon-type $EuVO_4$", J. Eur. Ceram. Soc. 38 (2018) 145-151.

3.1. Introduction:

Rare-earth orthovanadates, generally represented as AVO_4 (A is usually a trivalent metal ion) comprise an important class of multifunctional materials which are extensively studied for a variety of applications: phosphors, luminescent materials, scintillators, catalysts, counterelectrodes for electrochromic devices etc.[1-7] Usually, these materials show polymorphism and may crystallize in two forms such as monoclinic (m-) monazite ($CePO_4$) type and tetragonal (t-) zircon ($ZrSiO_4$) type.[3,4,8,9] Commonly, larger lanthanide ion favors the crystallization in monazite-type structure, while smaller lanthanide ions prefer zircon-type structure at ambient pressure.[10] In addition to their vast potential applications in renewable energy and alternative green technology, currently, zircon type orthovanadate nanoparticles pay attention towards the biomedical applications also due to their luminescent properties, chemical stability and non toxicity.[5] Recently, $LnVO_4$ orthovanadates attracted attention as prospective materials for electrochemical applications such as Li-ion batteries[11,12]and solid oxide fuel cells.[13-17] Despite intensive investigations, until now, the information on high-temperature electrical properties of $LnVO_4$ compounds remains comparatively limited.

Even though, the properties of $LnVO_4$ have been explored in various fields, only a few of them are well studied in terms of electrical conductivity. In this concern, from the available literature data on electrical characterization, a well established system is $CeVO_4$. Watanabe et al.[18] reported the electrical conductivity of $CeVO_4$ and $Ce_{1-x}M_xVO_{4-0.5x}$ (M= Ca, Sr and Pb) and $Ce_{1-y}Bi_yVO_4$ systems. The incorporation of divalent cations not only induces the electrical conductivity of $CeVO_4$ but also increases the number of oxygen vacancies. They concluded the compound $CeVO_4$ as a p-type semiconductor based on Seebeck coefficient data. The effect of alkaline earth metals such as Ca and Sr on $CeVO_4$ have been studied with different dopant concentrations. According to this

report, oxygen ionic conductivity is essentially independent of A-site dopant concentration. Ionic transport was discussed in terms of interstitial oxygen diffusion mechanism. Contrary to the ionic conductivity, p-type electronic transport was found to be dependent on divalent cation concentration.[15,16] Petit et al.[10] studied Sr^{2+} substitution in $CeVO_4$ systems and disclosed the increased conductivity values both in air and in reduced atmospheres. They confirmed that substitution by Sr^{2+} increases electrical conductivity in $Ce_{1-x}Sr_xVO_4$ series within the solid solution formation limits. The higher conductivity of doped samples is attributed to the smaller lattice parameters which enabled the easy jumping of charge carriers.

As an important member of $LnVO_4$ family, europium vanadate $EuVO_4$ has been extensively studied in a large variety of fields. At ambient temperature and pressure, $EuVO_4$ is known to crystallize in tetragonal zircon-type structure (space group $I4_1/amd$). A reversible structural transformation from the zircon-type structure into a denser tetragonal scheelite-type (space group= $I4_1/a$) phase occurs at high pressure near 8 GPa.[5,19,20] To date, many research efforts have been dedicated to investigate the luminescent and the structural properties of $EuVO_4$ as well as the Eu-doped systems. Recently, Kim et al.[21] reported the synthesis of red emitting $EuVO_4$ phosphor by the solution combustion method and studied the effect of annealing temperature on its emission properties. Several groups have also reported the biological importance of these materials. By virtue of its binding and fluorescence properties, $EuVO_4$ can be used as a biomonitor to track biological systems.[22] Mesoporous silica-coated luminescent europium-doped gadolinium vanadate ($GdVO_4:Eu^{3+}@mSiO_2$) nanoparticles may serve not only as an imaging nanoprobe for fluorescence imaging and magnetic resonance imaging (MRI), but also as an anti-cancer drug delivery vehicle.[23] $YVO_4:Eu$[24] and $EuVO_4$ nanoparticles have been reported to act as a good sensor materials for H_2O_2 detection.[25]

The literature data on electrical properties of $EuVO_4$ are scarce and contradictory, as discussed below.

3.2. Impact of magnesium substitution on electrical transport properties of zircon-type $EuVO_4$

The present work focussed to study the effect of substitution by a third cation such as divalent Mg ion on the properties of the host lattice of tetragonal zircon type $EuVO_4$ with the emphasis on electrical transport. Synthesis of the materials was carried out by adopting conventional solid state route. Solid state route is chosen because, compared to the other ceramic oxide preparation methods like chemical synthesis, the former needs only less amount of solvents, simple operation, low cost and predominantly give high yields of the required products.[26] The nominal composition of the prepared materials was formulated as $Mg_xEuVO_{4\pm\delta}$ (x = 0.0, 0.1, 0.2, 0.3 and 0.5) in order to elucidate the mechanism of substitution. In addition to electrical measurements, structural, microstructural, dilatometric and optical properties of the materials were also studied.

3.2.1. Experimental

$Mg_xEuVO_{4\pm\delta}$ (x = 0.0, 0.1, 0.2, 0.3, 0.4 and 0.5) ceramic powders were synthesized using solid state reaction method starting from $Mg_5(CO_3)_4(OH)_2*5H_2O$ (99.0%, Sigma-Aldrich), Eu_2O_3 (99.0%, IRE, India) and V_2O_5, (99.6+%, Sigma-Aldrich). Stoichiometric amount of the starting materials were weighed precisely as per the formula, mixed in appropriate proportions and ball-milled for 24 hour in ethanol medium. The milled precursors were then pre-reacted in air at 650°C and 750°C for six hours with intermediate grindings. The resultant mixtures were further calcined at 1000°C for 20 hours with several re-grindings. Calcined powders were mixed with 4 wt.% of polyvinyl alcohol (PVA, average molecular weight 72,000, BDH Lab suppliers, Poole, U.K.) as a binder and compacted uniaxially at 100 MPa into cylindrical disks. The compacts were

sintered in air for 6 hours at 1300°C and 1200°C for $EuVO_4$ and $Mg_xEuVO_{4\pm\delta}$ (x = 0.1-0.5), respectively, with an intermediate soaking time of 600°C to expel the binder. In the course of sintering, the pellets were covered by the powders of the same cation composition in order to minimize possible high-temperature losses. Optimization of sintering conditions was considered to decrease porosity. Shrinkage characteristics of compacts (green pellets with Ø ~ 8 mm and thickness ~ 10 mm) were measured using a horizontal dilatometer (Netzsch DIL 402 PC) from room temperature to 1200°C with a heating rate of 10°C/min. The density of sintered specimens was determined by Archimedes method using deionized water as immersion medium.

X-ray diffraction (XRD) patterns were collected by means of PANalytical X'pert Pro and Rigaku D/Max-B diffractometers (Cu-K_α radiation). The calculations of lattice constants and semi-quantification of phase fractions were conducted using X'pert Highscore Plus software. Microstructural characterization (SEM) coupled with energy dispersive spectroscopy (EDS) for elemental mapping was performed by Hitachi SU-70 microscope with Bruker Quantax 400 detector. Photoluminescence (PL) measurements of the samples were performed on a Shimadzu UV-2401 PC UV–visible spectrophotometer using $BaSO_4$ as a reference for the wavelengths within the range of 200–800 nm. Thermomechanical analyzer (TMA/SS7300, SII Nano Technology Inc.) was used to determine the coefficients of thermal expansion (CTE) of ceramics materials in air between room temperature and 400°C.

Electrical conductivity (σ) was determined employing impedance spectroscopy (Agilent 4284A precision LCR meter, frequency range 20 Hz - 1 MHz) using two-electrode arrangement and disk-shaped sintered samples (thickness ~ 2 mm, Ø ~ 10 mm) with porous Pt electrodes painted onto flat surfaces and sintered at 950°C. The measurements were performed as function of temperature in controlled atmospheres. The

average oxygen-ion transference numbers ($\overline{t_O}$) under $p(O_2)$ gradients were determined by the modified electromotive force (e.m.f.) technique taking electrode polarization into account.[27,28] In the course of measurements, oxygen partial pressure and relative humidity in the gas flow was monitored by yttria-stabilized zirconia solid electrolyte sensor and by Jumo humidity transducer, respectively. Unless indicated otherwise, the relative humidity in air (supplied by air compressor) corresponded to ~10% (at room temperature). The terms of "dry" and "wet" air refer to a gas additionally passed through silica-gel dryer or humidified by a bubbling through distilled water at room temperature respectively.

3.2.2. Results and Discussion

3.2.2.1. Phase relationships and crystal structure

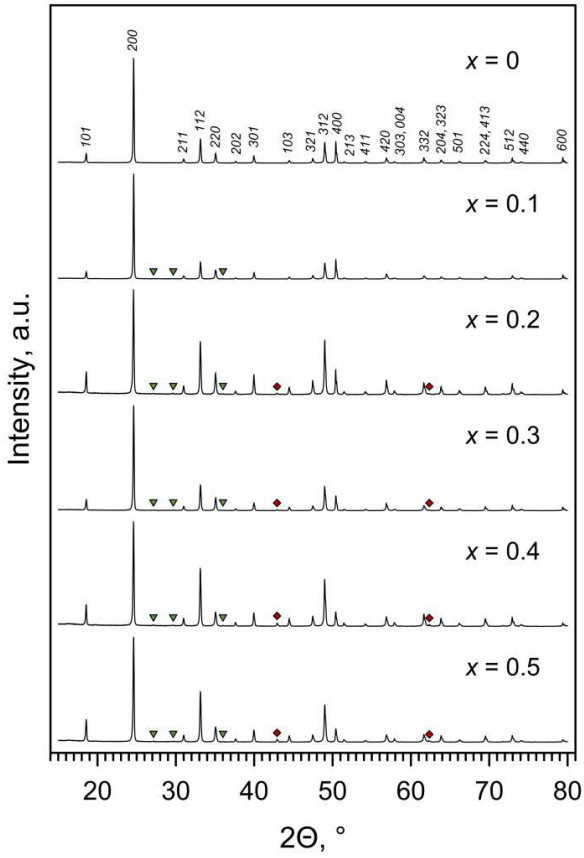

Figure 3.1: XRD patterns of as-prepared $Mg_xEuVO_{4\pm\delta}$ ceramics. Reflections are indexed in the *$I4_1/amd$* space group. Triangles and diamonds mark the peaks of $Mg_3(VO_4)_2$ (ICDD PDF #01-73-0207) and MgO (ICDD PDF #01-89-4248) secondary phases, respectively.

Powder X-ray diffraction was the prime tool to interpret the crystal structure and to understand the maximum feasibility of solid solution formation of the synthesized materials. The crystalline nature of the samples could be clearly figured out from the sharp reflections recorded in the diffraction pattern. Fig. 3.1 shows XRD patterns of as-prepared $Mg_xEuVO_{4\pm\delta}$ ceramic materials. In all cases, the patterns can be indexed in space group $I4_1/amd$ characteristic for tetragonal zircon-type structure, in agreement with ICDD PDF #01-086-0995.

While parent $EuVO_4$ ceramics was phase-pure, XRD spectra of other compositions demonstrated the presence of minor impurity peaks on the background level. For better illustration, fig. 3.2 shows a magnified section of XRD pattern of ceramics with x = 0.1. The impurity peaks were assigned to magnesium orthovanadate $Mg_3(VO_4)_2$ and periclase MgO secondary phases.

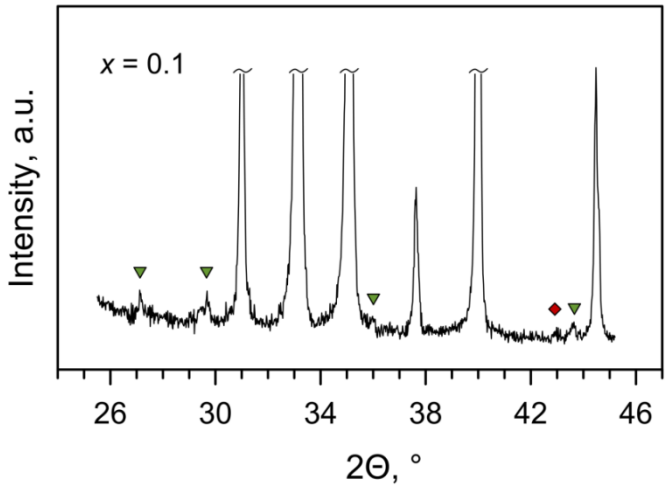

Figure 3.2: Magnified section of XRD pattern of $Mg_xEuVO_{4\pm\delta}$ (x = 0.1) ceramics. Triangles and diamond mark the reflections of $Mg_3(VO_4)_2$ (ICDD PDF #01-73-0207) and MgO (ICDD PDF #01-89-4248), respectively.

Roughly estimated weight fractions of impurity phases are listed in Table 3.1. The fraction of $Mg_3(VO_4)_2$ remains approximately constant for all prepared materials, whereas amount of MgO impurity increases with doping.

Table 3.1: Lattice parameters and phase composition of $Mg_xEuVO_{4\pm\delta}$ ceramics

x	Lattice parameters, Å (± 0.001)		Phase impurities, wt.% *	
	a	*c*	$Mg_3(VO_4)_2$	MgO
0.0	7.235	6.367	-	-
0.1	7.234	6.366	3.0	0.1
0.2	7.235	6.364	4.2	2.1
0.3	7.235	6.366	3.2	3.3
0.4	7.235	6.365	3.9	6.4
0.5	7.234	6.365	3.0	6.7

* Semi-quantification in the course of XRD data refinement assuming $EuVO_4$, $Mg_3(VO_4)_2$ and MgO phases (ICDD PDF#01-086-0995, 01-73-0207 and 01-89-4248, respectively).

Inspection of sintered ceramics by SEM coupled with EDS analysis confirmed these observations. The periclase phase was found to segregate in the form of small grains at the grain boundaries or inside larger grains of the main zircon-type $EuVO_4$-based phase. Inclusions of MgO are rare in $x = 0.1$ ceramics, but its amount clearly increases with *x* for other doped materials. Secondary orthovanadate $Mg_3(VO_4)_2$ phase, which has melting temperature close to the sintering conditions (1210-1212°C)[29,30], agglomerates between the grains of the main zircon-type phase. As an example, fig. 3.3 shows a cross-section of $x = 0.2$ ceramics with corresponding EDS elemental mapping.

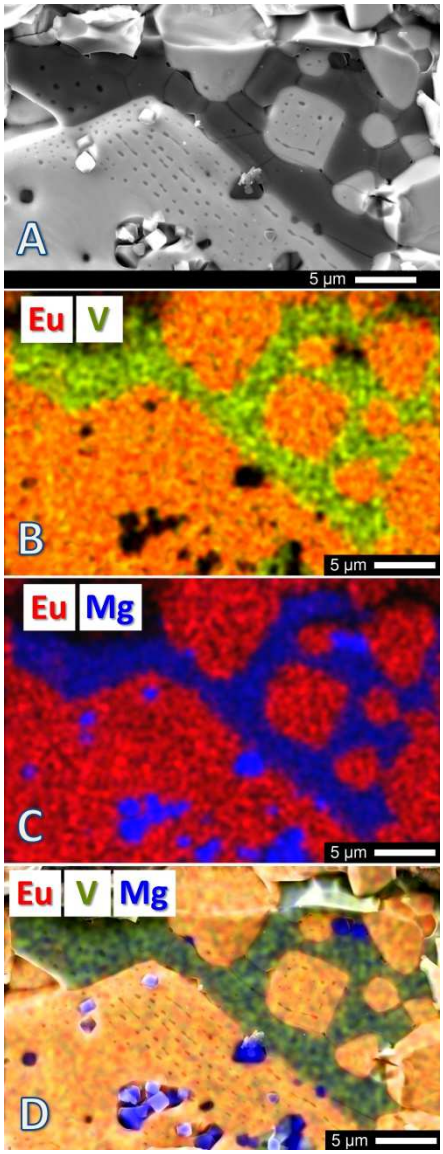

Figure 3.3: (A) SEM micrograph of fractured $Mg_xEuVO_{4\pm\delta}$ (x = 0.2) ceramics; (B-C) corresponding EDS elemental maps; (D) SEM micrograph with overlaid EDS elemental maps

Formula unit $Mg_xEuVO_{4\pm\delta}$ implies that the substitution by magnesium (if any) may occur either equally in both sublattices or preferably in one of sublattices. In the latter case, the substitution should be accompanied by a segregation of Eu- or V-based phases to maintain the mass balance. Taking into account the segregation of approximately similar amounts of $Mg_3(VO_4)_2$ for all doped compositions and monotonically increasing fraction of MgO for compositions with x>0.1, one may conclude that solubility of

magnesia in $EuVO_4$ is very limited and occurs preferably into vanadium sites. The overall reaction can be written therefore as:

$$x\mathrm{MgO} + \mathrm{EuVO_4} \rightarrow (\mathrm{EuMg}_a)_A(\mathrm{V}_{1-b}\mathrm{Mg}_{a+b})_B\mathrm{O}_{(4-\delta)(1+a)} + 0.5b\mathrm{Mg_3(VO_4)_2} + c\mathrm{MgO} \quad (3.1)$$

where $x = 2a + 2.5b + c$, and A and B indicate europium and vanadium sublattices, respectively. The estimations based on approximate secondary phase fractions suggested that, in fact, a $\rightarrow 0$ and b should be close to 0.04-0.06. In other words, substitution by magnesium occurs preferentially into vanadium sublattice and is limited to ~ 5% of B sites. This explains nearly constant fraction of $Mg_3(VO_4)_2$ phase, segregated to maintain overall mass balance of europium and vanadium cations, in all doped ceramics.

Thus, it turns out that it is easier for zircon-type structure to tolerate the substitution of B-site cations by larger magnesium ions ($r^{IV}(V^{5+}) = 0.355$ Å and $r^{IV}(Mg^{2+}) = 0.57$ Å[31]) than the substitution of A-site cations by smaller Mg^{2+} ($r^{VIII}(Eu^{3+}) = 1.066$ Å and $r^{VIII}(Mg^{2+}) = 0.89$ Å) ions. At the same time, it is known that zircon-type structures tend to be adopted by ABO_4 compounds with B-site cations smaller than Ge^{4+} ($r^{IV} = 0.39$ Å).[32] The effective radius of Mg^{2+} in 4-fold coordination significantly exceeds this threshold and is also 60% larger compared to V^{5+}. This results in a very limited solid solubility of magnesium in vanadium sublattice of $EuVO_4$. The calculated lattice parameters of zircon-type phase (Table 3.1) are in good agreement with previous reports.[33,34] As one may expect, minor substitution by magnesium has a negligible effect on the lattice constants; both parameters remain constant within the limits of experimental error.

3.2.2.2. Sintering and microstructure

The sintering process is one of the crucial steps in ceramic processing and powder metallurgy. Sintering is associated with changes that arise in materials during the course of firing, together with variation of grain size and shape and also the changes in pore

morphology and size. All these processes are accompanied by volume changes, i.e. shrinkage. Sintering in dilatometers has the advantage to enable continuous monitoring of specimen shrinkage, by following the change of length in a particular direction as a function of temperature without any stress imposed other than the sample's mass. So this method is frequently used in ceramic technology to determine sintering behaviour of powder compacts. For a shrinkage curve, at a low temperature only thermal dilatation of the green body is recorded. When a particular temperature is reached the sintering process begins and the material starts to shrink. As long as the temperature increases the thermal dilatation also continues. During the dwell time at the sintering temperature the thermal dilatation is stopped, but shrinkage originated by the sintering process still continues.[35]

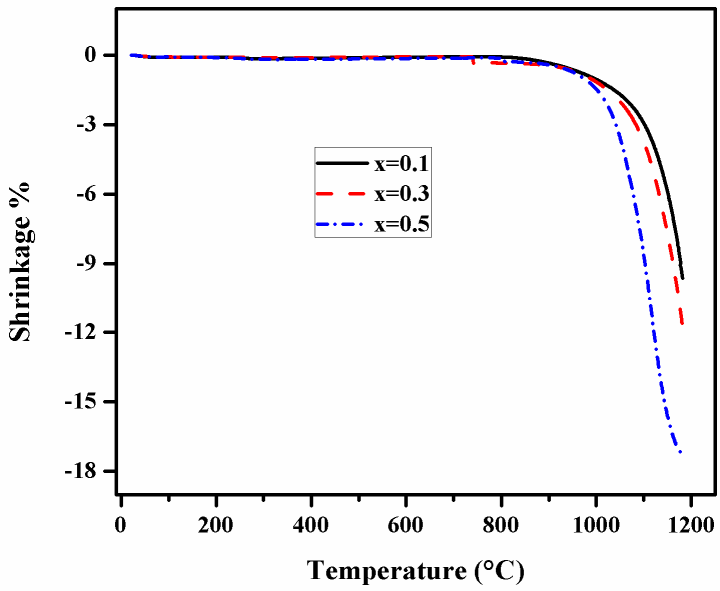

Figure 3.4: Shrinkage curves for $Mg_xEuVO_{4\pm\delta}$ compacts on heating.

Fig. 3.4 illustrates the shrinkage characteristics of $Mg_xEuVO_{4\pm\delta}$ (x = 0.1, 0.3 and 0.5) green compacts on heating in air. It is evident from this plot that for all the compositions the onset of shrinkage is found to be above 600°C. So, all the samples were kept at 600°C for 30 minutes during the sintering process in order to remove the binder prior to densification. The onset of shrinkage corresponds to ~ 900-1000°C, and sintering of Mg-doped compositions is likely to be assisted by the presence of $Mg_3(VO_4)_2$

secondary phase with comparatively low melting temperature (as mentioned above). As a result, $Mg_xEuVO_{4\pm\delta}$ ceramics sintered at 1200°C had much lower porosity compared to undoped $EuVO_4$ sintered at 1300°C (Table 3.2).

Table 3.2: Density and coefficients of thermal expansion of $Mg_xEuVO_{4\pm\delta}$ ceramics

X	Density, g/cm^3	Relative density, %	Average CTE, ppm/K (150-400°C)
0.0	4.52	85.0	3.2
0.1	4.97	95.8	3.6
0.2	4.91	96.1	4.5
0.3	4.89	95.8	4.7
0.4	4.84	96.5	5.1
0.5	4.78	95.0	6.0

* Note: theoretical density of Mg-doped ceramics was estimated assuming $EuV_{0.95}Mg_{0.05}O_{3.925}$ composition of the zircon phase and using fractions of impurity phases given in Table 3.1. The densities of $Mg_3(VO_4)_2$ and MgO phases were taken from ICDD PDF# 01-73-0207 and 01- 89-4248, respectively.

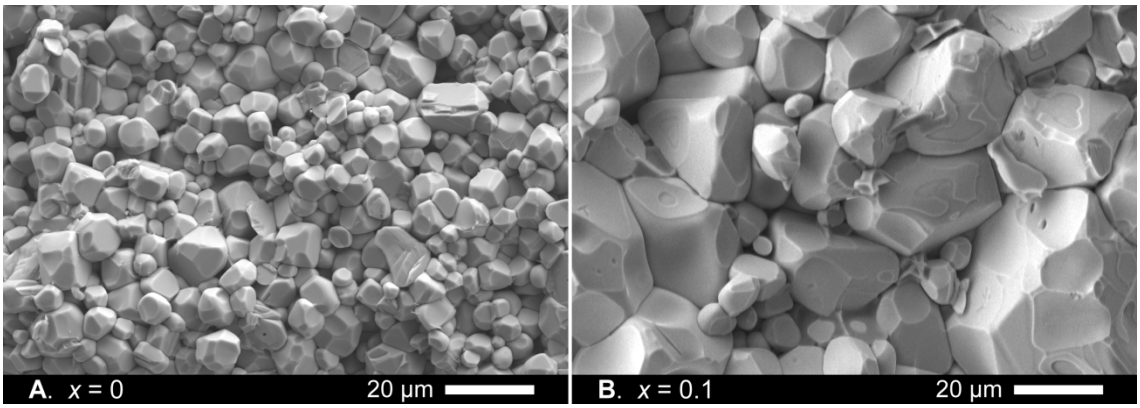

Figure 3.5: SEM micrographs of fractured $Mg_xEuVO_{4\pm\delta}$ ceramics: (A) *x* = 0.0, and (B) *x* = 0.1.

Two representative SEM images illustrating the microstructure of sintered $Mg_xEuVO_{4\pm\delta}$ ceramics are shown in fig. 3.5. Additions of magnesia and the presence of low-melting impurity phase significantly promoted the grain growth. While the grain size

of undoped $EuVO_4$ varied in the range 3-15 μm, the ceramics with x = 0.1 consisted of grains in the range of 5-60 μm.

3.2.2.3. Thermal expansion

The coefficient of linear thermal expansion (CTE or α) is a material property which indicates the extent up to which a material expands upon heating. CTE can be defined as the measure of change in length or volume of a material for a unit change in temperature. The CTE data is calculated by taking the ratio of change in length to the quantity of the length at room temperature multiplied by the change of temperature and can be expressed by the formula

$$\alpha = \frac{\Delta l}{l_0 \Delta T} \qquad 3.1$$

Where Δl is the change in sample length on heating through the temperature (T) range of ΔT and l_0 is the initial sample length. Materials expand because as the temperature increases the thermal vibration of atoms in the materials also increases which in turn results in the increase of average separation distance between adjacent atoms. In the present study a Thermomechanical Analyzer (TMA) is used for the CTE measurement. TMA consists of a specimen holder and a probe that transmits changes in length to the transducer that translates the movements of the probe in to electrical signal.[36]

Fig. 3.6 demonstrates the dilatometric curves of $Mg_xEuVO_{4\pm\delta}$ ceramics recorded from room temperature to 400°C. The average values of coefficient of thermal expansion (CTE) are listed in Table 3.2. The calculated CTE of undoped $EuVO_4$, 3.2 ppm/K, is in good agreement with the previous literature reports on other zircon-type ABO_4 vanadates.[15-17,38] Thermal expansion of $Mg_xEuVO_{4\pm\delta}$ ceramics tends to increase with magnesium content from 3.6 ppm/K for x = 0.1 to 6.0 ppm/K for x = 0.5 in the same temperature range. This can be attributed to the effect of partial substitution of vanadium by larger magnesium cations, in agreement with the general trends characteristic for the

oxides with zircon-type structure[37] combined with increasing fraction of MgO secondary phase which has CTE = 11-13 ppm/K at 30-600°C.[39]

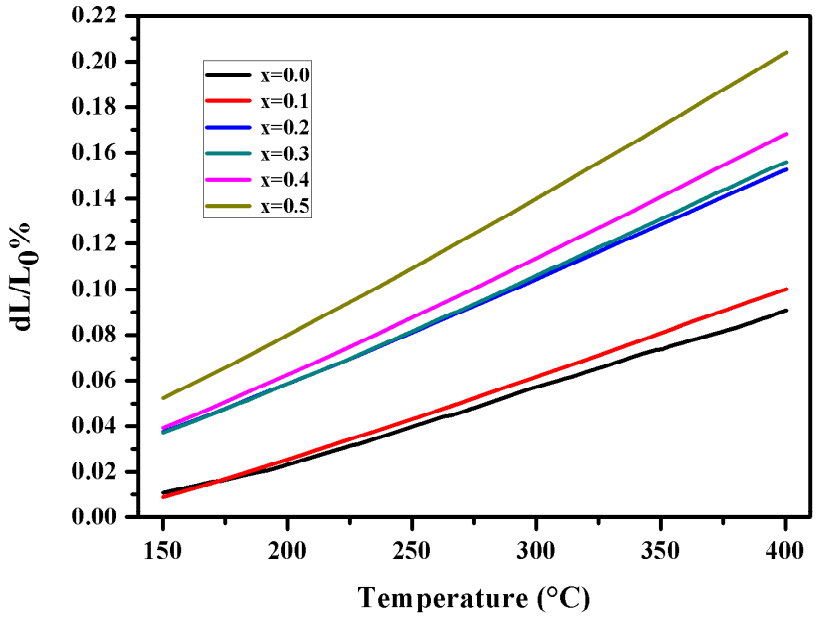

Figure 3.6: Dilatometric curves $Mg_xEuVO_{4\pm\delta}$ ceramics.

3.2.2.4. Optical Properties

Fig. 3.7 shows the PL emission spectra of $Mg_xEuVO_{4\pm\delta}$ ceramics heat-treated at 1000°C for 20 hours. Emission characteristics of all the samples showed almost similar behavior; no noticeable changes are observed except the variation in emission intensities. Each emission spectrum comprises four groups of emission lines in 575-725 nm range which can be attributed to the characteristic red emission due to the transitions from the excited $^5D_0$-^7F_J (J = 1, 2, 3 and 4) levels of Eu^{3+} ions. The emission intensities of all these transitions generally depend on the local symmetry of the crystal field of Eu ions. The emission spectrum is dominated by the red $^5D_0$-$^7F_2$ transition centered at 619 nm and caused by the forced electric dipole transition of the Eu^{3+} ions.[21,22]

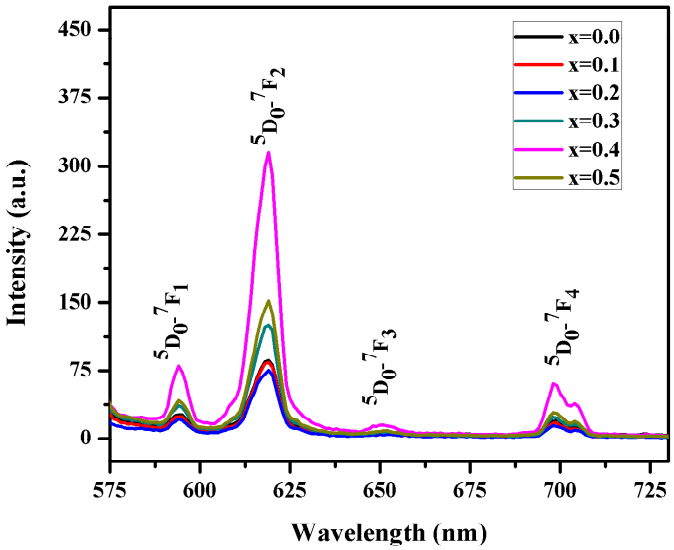

Figure 3.7: PL emission spectra of $Mg_xEuVO_{4\pm\delta}$ ceramics calcined at 1000°C for 20h (λ_{ex}=360 nm)

3.2.2.5. Electrical conductivity and ionic transport

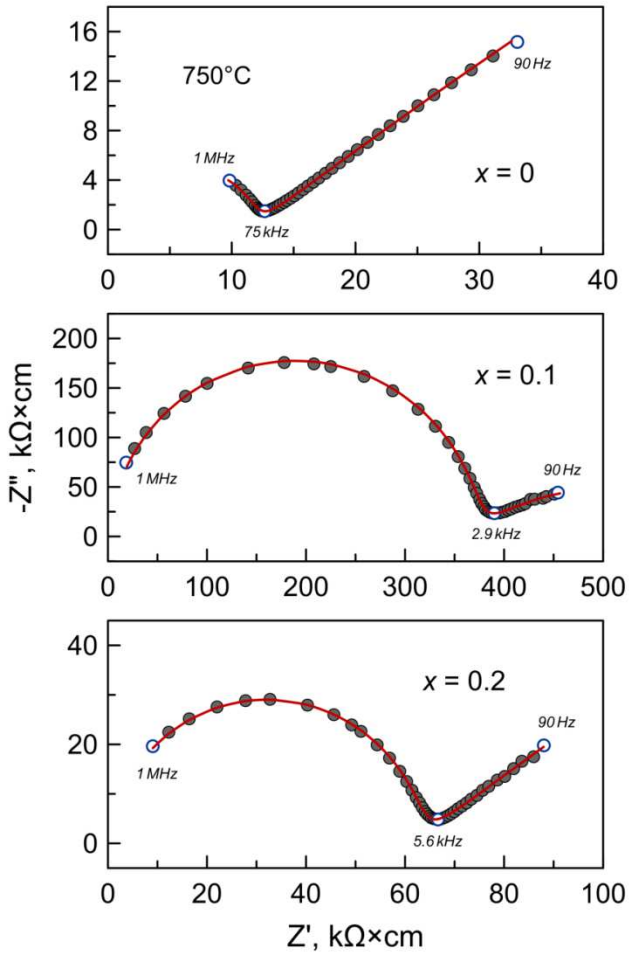

Figure 3.8: Impedance spectra of $Mg_xEuVO_{4\pm\delta}$ ceramics collected in air at 750°C. Solid lines correspond to the fitting results. Calculated capacitance values: C_{HF} = (4-32)×10^{-12} F/cm and C_{LF} = (4-27)×10^{-7} F/cm.

Analysis of impedance spectroscopy data showed that grain boundaries have a negligible contribution to the total resistivity of $Mg_xEuVO_{4\pm\delta}$ ceramics at temperatures ≥ 600°C. Typical examples of impedance spectra are given in fig. 3.8. Each spectrum comprises two semicircles and was fitted using a simple $(R_{HF}//CPE_{HF})+(R_{LF}//CPE_{LF})$ model. High-frequency (HF) contribution was attributed to the bulk resistance and low-frequency (LF) semicircle was assigned to the electrode process.

Undoped $EuVO_4$ exhibits semiconducting behavior in air (fig. 3.9) with activation energy of 63-84 kJ/mol in the studied temperature range (Table 3.3). Note that earlier reports on the electrical conductivity of zircon-type $EuVO_4$ provide contradictory results. Gaur and Lal[40,41] reported electrical conductivity data for the $LnVO_4$ (Ln = Ce-Yb) series, including europium orthovanadate, measured using pressed pellets. For all compositions, Arrhenius plots of conductivity showed unusual behavior with multiple changes of slope and a sharp increase of conductivity in the temperature range between approximately 600 and 850°C, in vicinity of melting point of V_2O_5 (T_{melt} = 681°C). One may suspect therefore that these data may be strongly affected by the presence of unreacted vanadium pentoxide, its melting/evaporation and accompanying dimensional changes on temperature cycling. Prasad et al.[42] reported electrical conductivity of $EuVO_4$ single crystals measured perpendicular to the *c* axis. The conductivity was ~ 1 order of magnitude lower compared to the results obtained in this work and exhibited higher activation energy (92 kJ/mol at 430-730°C). Finally, Li et al.[19] studied low-temperature electrical conductivity of zircon-type $EuVO_4$ samples obtained by thermal treatment of scheelite-type $EuVO_4$ in air at 600°C. However, the values of conductivity discussed in the text and given in a plot (Fig. 5 [19]) differ by 4 orders of magnitude, and it is not possible to figure out which values are correct.

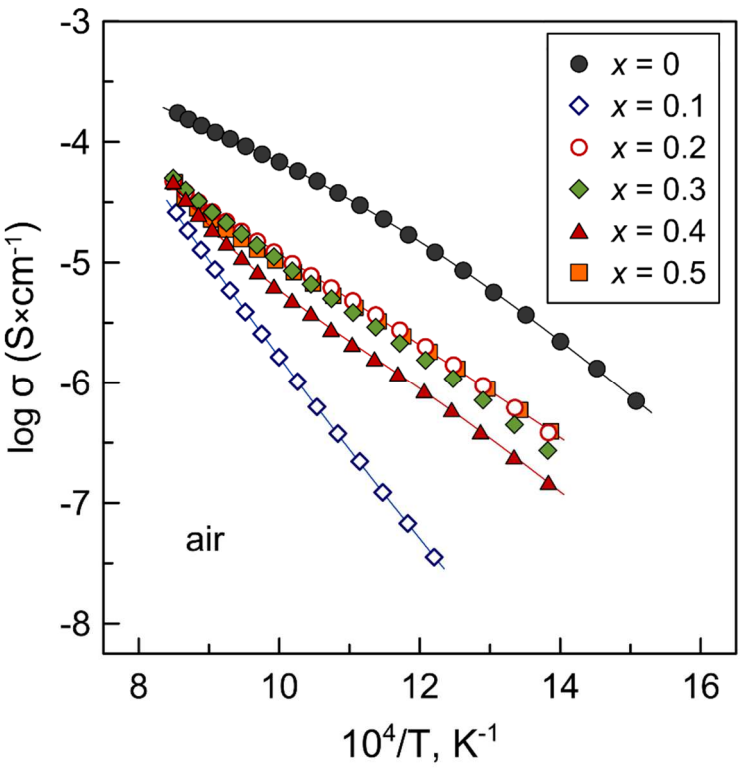

Figure 3.9: Total electrical conductivity of $Mg_xEuVO_{4\pm\delta}$ ceramics

Table 3.3: Activation energy of total electrical conductivity in air

X	T, °C	E_A, kJ×mol^{-1}
0.0	650-900	63
	400-650	84
0.1	550-900	157
0.2	450-880	80
0.3	450-880	86
0.4	450-880	92
0.5	450-860	76

Note: Activation energy was calculated using Arrhenius model $\sigma = \frac{A_0}{T}\exp\left(-\frac{E_A}{RT}\right)$.

In order to confirm the nature of electrical transport in the studied materials, oxygen-ion transference numbers (Table 3.4) were measured by modified e.m.f.

technique. Note that $\overline{t_O}$ values determined by this technique are higher compared to the simple E_{obs}/E_{theor} ratios, thus suggesting significant effect of electrode polarization on the observed e.m.f. values under open-circuit conditions.[28]

Table 3.4: Average transference number $\overline{t_O}$ determined by modified e.m.f. technique

x	$p(O_2)$ gradient	T, °C	E_{obs}/E_{theor}	$\overline{t_O}$
0.0	1.00 atm / 0.21 atm	900	0.67	0.952
		800	0.78	0.977
		700	0.75	0.990
0.1	1.00 atm / 0.21 atm	900	0.06	0.417
		800	0.04	0.448
	0.21 atm / 10^{-3}atm	900	0.04	0.424

The results (Table 3.4) indicate that undoped $EuVO_4$ is predominantly oxygen-ionic conductor under oxidizing conditions; the contribution of electronic transport to the total conductivity corresponds to 1-5% at 700-900°C. Note that $EuVO_4$ is expected to be oxygen-stoichiometric, with all regular oxygen sites in zircon-type lattice completely filled. Li et al.[19]assumed that oxygen ions may move through interstitial sites along c axis between the chains formed by alternating edge-sharing VO_4 tetrahedra and EuO_8 dodecahedra. Interstitial oxygen diffusion mechanism was suggested for related $CeVO_{4+\delta}$ and $Ce_{1-x}A_xVO_{4+\delta}$ (A = Ca, Sr).[15,16] Interstitial mechanism for the diffusion of oxygen in a structural analog, zircon $ZrSiO_4$, is also supported by the theoretical calculations.[43] Contrary to $CeVO_{4+\delta}$, which is believe to be slightly oxygen overstoichiometric due to tendency of cerium cation to higher oxidation state (4+) under oxidizing conditions[15,16],

formation of interstitial oxygen in oxygen-stoichiometric $EuVO_4$ may be expected to occur via Frenkel disorder:

$$O_O^{\times} \xleftrightarrow{K_F} V_O^{\bullet\bullet} + O_i'' \qquad 3.2$$

where K_F is the temperature-dependent equilibrium constant.

Acceptor-type substitution by magnesium results in a drop of total conductivity of $Mg_xEuVO_{4\pm\delta}$ (x = 0.1) ceramics (fig. 3.9) and an increase of activation energy (Table 3.3). Further additions of magnesia lead to a decrease of E_A. As a result, conductivity of $Mg_xEuVO_{4\pm\delta}$ (x = 0.2-0.5) in a low-temperature range is higher compared to the composition with x = 0.1, but tends to similar values when temperature increases. Furthermore, electrical conductivity and activation energy values show comparatively minor changes with composition for ceramics with $x \geq 0.2$.

These observations imply that acceptor-type substitution suppresses the concentration of charge carriers and/or their mobility. The results of transference numbers measurements indicate that substitution by magnesium deteriorates, in particularly, oxygen-ionic transport: $\overline{t_O}$ values under oxidizing conditions drop to ~0.4 (Table 3.4). Such behavior seems to be reasonable if the mobility of interstitial oxygen ions substantially exceeds the mobility of oxygen vacancies in zircon-type $EuVO_4$ lattice. Partial substitution of V^{5+} by Mg^{2+} is compensated by formation of oxygen vacancies to maintain the electroneutrality:

$$3[Mg_V'''] = 2[V_O^{\bullet\bullet}] \qquad 3.3$$

and should shift the equilibrium of reaction (3.2) to the left, thus suppressing the formation of interstitial oxygen ions. This reduces the ionic conductivity which is expected to occur preferentially via oxygen vacancy diffusion mechanism in $Mg_xEuVO_{4\pm\delta}$ (x = 0.1) ceramics. Further additions of MgO result in a moderate initial increase of oxygen deficiency and, therefore, ionic transport until the solubility limits of magnesium

cations in $EuVO_4$ is reached. The variations of electrical conductivity of ceramics with $x \geq 0.2$ are caused mainly by fractions and distribution of secondary phases.

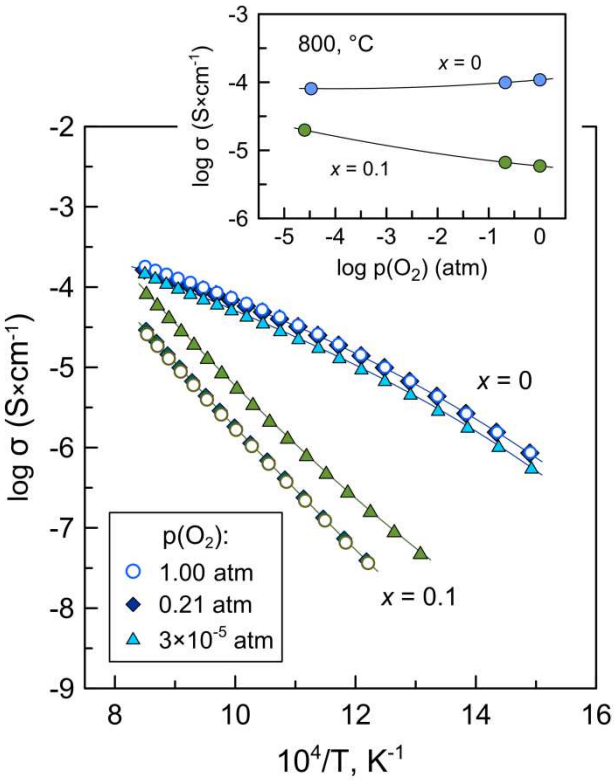

Figure 3.10: Total electrical conductivity of $Mg_xEuVO_{4\pm\delta}$ (x = 0.0 and 0.1) ceramics in different atmospheres (oxygen, air and argon). Inset shows electrical conductivity at 800°C plotted vs oxygen partial pressure.

Fig. 3.10 shows the total conductivity of undoped $EuVO_4$ and $Mg_xEuVO_{4\pm\delta}$ (x = 0.1) ceramics measured in atmospheres with different $p(O_2)$. Electrical transport in parent europium vanadate tends to decrease with reducing oxygen partial pressure. In contrast, electrical conductivity of $Mg_xEuVO_{4\pm\delta}$ (x = 0.1) demonstrate an opposite tendency and increases when $p(O_2)$ is reduced. For better illustration, these trends are emphasized in inset in fig.3.10. Different behavior further confirms different prevailing mechanisms of ionic transport in undoped and acceptor-doped $EuVO_4$. In first case, oxygen release from the lattice on reduction decreases the concentration of mobile interstitial oxygen ions

$$O_i'' \leftrightarrow 0.5O_2 + 2e' \qquad 3.4$$

and, consequently, ionic conductivity. In the case of Mg-substituted vanadate, oxygen losses from the lattice on reducing $p(O_2)$ increase the concentration of oxygen vacancies:

$$O_O^{\times} \leftrightarrow V_O^{\bullet\bullet} + 0.5O_2 + 2e' \qquad 3.5$$

and, therefore, oxygen-ionic transport. In both cases, this should be accompanied by increasing n-type electronic contribution. The latter is in agreement with a rather negligible variation of oxygen transference number of x = 0.1 ceramics on reduction (Table 3.4).

It was reported recently that acceptor-doped $La_{0.99}Ca_{0.01}VO_{4-\delta}$ with related monazite-type structure is a pure ionic conductor under oxidizing conditions with protonic conductivity dominating in the low-temperature range under wet conditions.[44] Therefore, electrical conductivity of $EuVO_4$ and $Mg_xEuVO_{4\pm\delta}$ (x = 0.1) was measured under dry and humidified air in order to identify possible protonic transport in this materials under wet conditions. The results are shown in fig. 3.11. It was found that, contrary to $La_{0.99}Ca_{0.01}VO_{4-\delta}$, humidity has rather negligible effect of transport properties of acceptor-substituted $EuVO_4$. Although the bulk resistance tends to decrease slightly under wet air, as demonstrated by impedance spectra (fig. 3.11C), electrical conductivity remains nearly unchanged in the studied temperature range (fig. 3.11A). At the same time, undoped $EuVO_4$ ceramics demonstrates 1.5 times lower resistivity under wet air in the entire studied temperature range (fig.3.11A and B). This suggests a protonic contribution to the total electrical conductivity of $EuVO_4$ in humidified atmosphere, and that the protonic transport in this material is also associated with the interstitial diffusion mechanism.

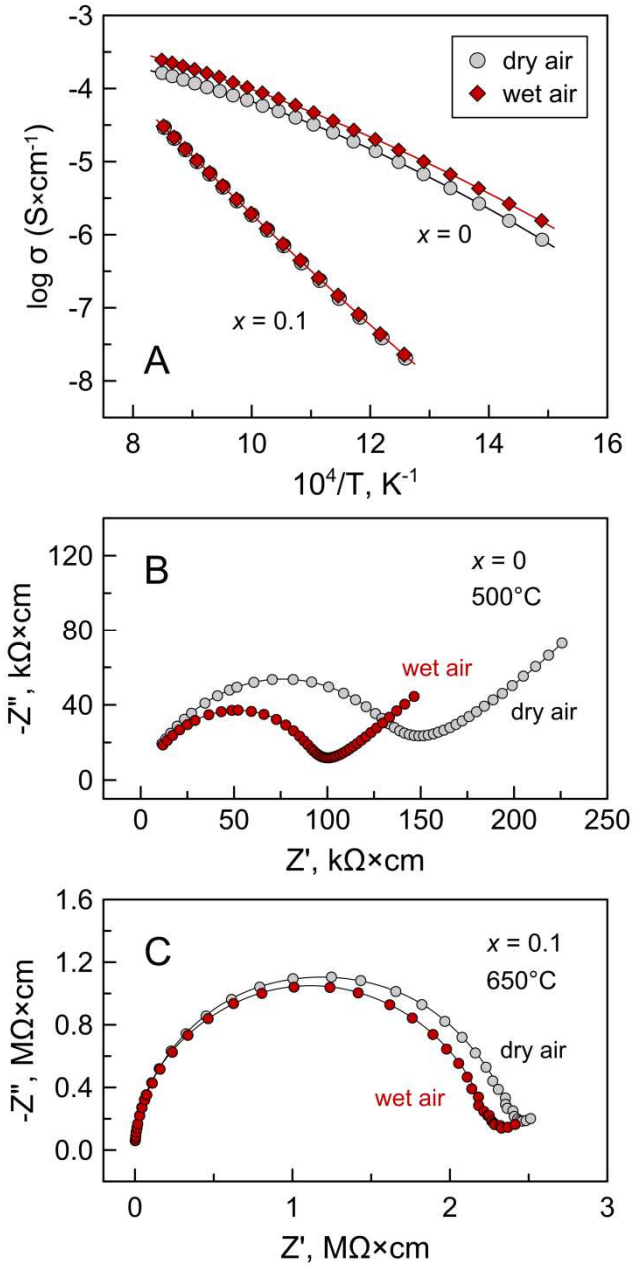

Figure 3.11: (A) Total electrical conductivity of $Mg_xEuVO_{4\pm\delta}$ (x = 0.0 and 0.1) ceramics in dry and wet air; examples of corresponding impedance spectra: (B) x = 0.0, 500°C and (C) x = 0.1, 650°C. p(H_2O) in dry and wet atmospheres was < 2×10^{-3} and ~2.5×10^{-2}atm, respectively.

3.2.3. Conclusions

- Magnesium-substituted $Mg_xEuVO_{4-\delta}$ (x = 0 - 0.5) ceramics were prepared by solid state synthesis method.
- XRD analysis in combination with SEM/EDS indicate that magnesium substitutes preferentially into vanadium sublattice and has a low solid solubility limit close to ~5% in B sublattice.
- The substitution is compensated by segregation of $Mg_3(VO_4)_2$ phase and is accompanied by increasing fraction of MgO impurity for $x \geq 0.2$.
- Magnesium additions increase slightly coefficients of thermal expansion, which vary in the range 3.2-6.0 ppm/K at 150-400°C,
- Magnesium additions have a rather negligible effect on the optical properties.
- Undoped $EuVO_4$ is predominantly oxygen-ionic conductor with oxygen transference numbers in the range 0.96-0.99 at 700-900°C under oxidizing conditions.
- Acceptor-type substitution by magnesium suppresses total electrical conductivity and, in particular, oxygen-ionic transport.
- The variations of electrical transport properties suggest a change of prevailing mechanism of ionic transport from interstitial oxygen diffusion in parent $EuVO_4$ to oxygen vacancy diffusion in Mg-substituted vanadate.
- Humidified atmosphere has negligible impact on the electrical properties of substituted ceramics.
- Under wet conditions, electrical conductivity of undoped europium vanadate increased by 1.5 times indicating a protonic contribution to the total electrical transport in this material.

3.3. References

[1] M. Moussa, M. Djermouni, S. Kacimi, M. Azzouz, A. Dahani, A. Zaoui, First-principles calculations of structural, magnetic phase stability and electronic properties of RVO_4 compounds, *Comput. Mater. Sci.* 68 (2013) 361–366.

[2] R. Kalai Selvan, A. Gedanken, P. Anilkumar, G. Manikandan, C. Karunakaran, Synthesis and characterization of rare earth orthovanadate (RVO_4; R= La, Ce, Nd, Sm, Eu and Gd) nanorods/nanocrystals/nanospindles by a facile sonochemical method and their catalytic properties, *J. Clust. Sci.* 20 (2009) 291–305.

[3] C. Yu, M. Yu, C. Li, C. Zhang, P. Yang, J. Lin, Spindle-like lanthanide orthovanadate nanoparticles: Facile synthesis by ultrasonic irradiation, characterization, and luminescent properties, *Cryst. Growth Des.* 9 (2009) 783–791.

[4] W. Fan, X. Song, S. Sun, X. Zhao, Microemulsion-mediated hydrothermal synthesis and characterization of zircon-type $LaVO_4$ nanowires, *J. Solid State Chem.* 180 (2007) 284–290.

[5] A. B. Garg, D. Errandonea, High-pressure powder x-ray diffraction study of $EuVO_4$, *J. Solid State Chem.* 226 (2015) 147–153.

[6] G. Picardi, F. Varsano, F. Decker, U. Opara-Krasovec, A. Surca, B. Orel, Electrochemical characterization of optically passive $CeVO_4$ counterelectrodes, *Electrochim. Acta.* 44 (1999) 3157–3164.

[7] C. T. Au, W. D. Zhang, H. L. Wan, Preparation and characterization of rare earth orthovanadates for propane oxidative dehydrogenation, *Catal. Lett.* 37 (1996) 241–246.

[8] Z. Xu, C. Li, Z. Hou, C. Peng, J. Lin, Morphological control and luminescence properties of lanthanide orthovanadate $LnVO_4$ (Ln = La to Lu) nano-/ microcrystals via hydrothermal process, *CrystEngComm*. 13 (2011) 474–482.

[9] Y. Oka, T. Yao, N. Yamamoto, Hydrothermal synthesis of lanthanum vanadates: Synthesis and crystal structures of Zircon-type $LaVO_4$ and a new compound LaV_3O_9, *J. Solid State Chem.* 152 (2000) 486–491.

[10] C. T. G. Petit, R. Lan, P. I. Cowin, S. Tao, Structure and conductivity of strontium-doped cerium orthovanadates $Ce_{1-x}Sr_xVO_4$ ($0 \leq x \leq 0.175$), *J. Solid State Chem.* 183 (2010) 1231–1238.

[11] M. Yi, S. Park, C. Seong, Y. Piao, T. Yu, The general synthesis and characterization of rare earth orthovanadate nanocrystals and their electrochemical applications, *J. Alloy. Compd.* 693 (2017) 825–831.

[12] H. Zhan, J. Shu, X. Wei, K. Wang, J. Chen., Cerium vanadate nanoparticles as a new anode material for lithium ion batteries, *RSC Adv.* 3 (2013) 7403–7407.

[13] L. Adijanto, V. B. Padmanabhan, K. Rainer, R. J. Gorte, J. M. Vohs, Transition metal-doped rare earth vanadates : A regenerable catalytic material for SOFC anodes, *J. Mater. Chem.* 22 (2012) 11396–11402.

[14] N. Danilovic, J. Luo, K.T. Chuang, A. R. Sanger, $Ce_{0.9}Sr_{0.1}VO_x$ (x=3, 4) as anode materials for H_2S-containing CH_4 fueled solid oxide fuel cells, *J. Power Sources.* 192 (2009) 247–257.

[15] E. V. Tsipis, V. V. Kharton, N. P. Vyshatko, A. L. Shaula, J. R. Frade, Stability and oxygen ionic conductivity of zircon-type $Ce_{1-x}A_xVO_{4+\delta}$ (A=Ca, Sr), *J. Solid State Chem.* 176 (2003) 47–56.

[16] E. V. Tsipis, M. V. Patrakeev, V. V. Kharton, N. P. Vyshatko, J. R. Frade, Ionic and p-type electronic transport in zircon-type $Ce_{1-x}A_xVO_{4\pm\delta}$ (A = Ca, Sr), *J. Mater. Chem.* 12 (2002) 3738–3745.

[17] T. H. Gayathri, A. A. Yaremchenko, K. Zakharchuk, J. James, Effect of magnesium addition on the structural , microstructural and electrical properties of YVO_4, *J. Alloy. Compd.* 672 (2016) 549–557.

[18] A. Watanabe, Highly conductive oxides, $CeVO_4$, $Ce_{1-x}M_xVO_{4-0.5x}$ (M=Ca, Sr, Pb) and $Ce_{1-y}Bi_yVO_4$, with Zircon-type structure prepared by solid-state reaction in air, *J. Solid State Chem.* 153 (2000) 174–179.

[19] L. Li, G. Li, Y. Xue, H. Inomata, Structure, luminescence, and transport properties of $EuVO_4$, *J. Electrochem. Soc*. 148 (2001) J45–J49.

[20] W. Paszkowicz, J. Solano, P. Piszora, B. Bojanowski, A. Mujica, A. Muňoz, et al., Equation of state and electronic properties of $EuVO_4$: A high -pressure experimental and computational study, *J. Alloy. Compd.* 648 (2015) 1005–1016.

[21] K.Y. Kim, S. J. Yoon, K. Park, Synthesis and photoluminescence properties of $EuVO_4$ red phosphors, *Ceram. Int.* 40 (2014) 9457–9461.

[22] Y. Zhao, M. Shao, S. Liu, Z. Zhang, H. Lin, Hydrothermal synthesis of lanthanide orthovanadate: $EuVO_4$ particles and their fluorescence application, *CrystEngComm.* 14 (2012) 8033–8036.

[23] T. Kim, N. Lee, Y. I. Park, J. Kim, J. Kim, E. Y. Lee et al., Mesoporous silica-coated luminescent Eu^{3+} doped $GdVO_4$ nanoparticles for multimodal imaging and drug delivery, *RSC Adv.* 4 (2014) 45687–45695.

[24] D. Casanova, C. Bouzigues, T. L. Nguyên, O. Ramodiharilafy, L. B. Sima, T. Gacoin, et al., Single europium-doped nanoparticles measure temporal pattern of reactive oxygen species production inside cells, *Nat. Nanotechnol.* 4 (2009) 581–585.

[25] C. Ambard, F. Pereira, D. Portehault, B. Viana, K. Valle, D. Autissier, New synthesis strategies for luminescent YVO_4 :Eu and $EuVO_4$ nanoparticles with H_2O_2 selective sensing properties, *Chem. Mater.* 27 (2015) 5198–5205.

[26] S. Cho, Synthesis and luminescence properties of $LaVO_4$: RE^{3+} (RE = Sm , Eu , Tb , Tm) phosphors, *J. Nanosci. Nanotechnol.* 13 (2013) 7546–7550.

[27] V. P. Gorelov, Transport number determinations in ionic conductors using EMF measurements with active load, *Sov. Electrochem.* 24 (1988) 1380–1381.

[28] V. V. Kharton, A. A. Yaremchenko, A. P. Viskup, G. C. Mather, E. N. Naumovich, F. M. B. Marques, Ionic and p-type electronic conduction in LaGa(Mg,Nb)$O_{3-\delta}$ perovskites, *Solid State Ionics*. 128 (2000) 79–90.

[29] E. I. Speranskaya, System MgO-V_2O_5, *Izv. Akad. Nauk. SSSR, Neorg. Mater.* 7 (1971) 1804–1807.

[30] A. A. Fotiev, B. V. Slobodin, M. Y. Khodos, Vanadates. Composition, synthesis, structure, properties, Moscow, Nauka, 1988.

[31] R. D. Shannon, Revised Effective Ionic radii and systematic studies of interatomic distances in halides and chalcogenides, *Acta Cryst.* A32 (1976) 751–767.

[32] R. J. Finch, J. M. Hanchar, Structure and chemistry of Zircon and Zircon-group minerals, *Rev. Mineral. Geochemistry.* 53 (2003) 1–25.

[33] D. F. Mullica, E. L. Sappenfield, M. M. Abraham, B. C. Chakoumakos, L. A. Boatner, Structural investigations of several $LnVO_4$ compounds, *Inorganica Chim. Acta.* 15 (1996) 85–88.

[34] D. Errandonea, R. Perales, J. Fuertes, A. Segura, S. N. Achary, A. K. Tyagi, High-pressure structural investigation of several zircon-type orthovanadates, *Phys. Rev. B*. 79 (2009) 184104-184112.

[35] K. Maca, V. Pouchly, A. R. Boccaccini, Sintering densification curve - A practical approach for its construction from dilatometric shrinkage data, *Sci. Sinter.* 40 (2008) 117–122.

[36] P. Gabbott, Principles and applications of thermal analysis, Blackwell, 2008.

[37] E. C. Subbarao, D. K. Agrawal, H. A McKinstry, C. W. Sallese, R. Roy, Thermal expansion of compounds of Zircon structure, *J. Am. Ceram. Soc.* 73 (1990) 1246-1252.

[38] S. Zhang, S. Zhou, H. Li, N. Li, Investigation of thermal expansion and compressibility of rare-earth orthovanadates using a dielectric chemical bond method, *Inorg. Chem.* 47 (2008) 7863–7867.

[39] W. Martienssen, H. Warlimont (Eds.), Springer handbook of condensed matter and materials data, Springer, 2005.

[40] K. Gaur, H. B. Lal, Electrical transport in light rare-earth vanadates, *J. Mater. Sci.* 20 (1985) 3167–3176.

[41] K. Gour, H. B. Lal, Electrical transport in heavy rare-earth vanadates, *J. Mater. Sci.* 21 (1986) 2289–2296.

[42] M. Prasad, A. K. Pandit, T. H. Ansari, R. A. Singh, B. M. Wanklyn, Electrical transport properties of $EuVO_4$ single crustal, *Phys. Lett. A.* 138 (1989) 61–64.

[43] J. P. Crocombette, Theoretical study of point defects in crystalline zircon, *Phys. Chem. Miner.* 27 (1999) 138–143.

[44] M. Huse, T. Norby, R. Haugsrud, Proton conductivity in acceptor-doped $LaVO_4$, *J. Electrochem. Soc.* 158 (2011) B857–B865.

CHAPTER 4

EFFECT OF MAGNESIUM SUBSTITUTION ON THE STRUCTURAL, MICROSTRUCTURAL AND ELECTRICAL CHARACTERIZATIONS OF YVO_4

Magnesium-substituted yttrium vanadate ceramics, $Y_{1-x/2}Mg_xV_{1-x/2}O_{4-\delta}$ (x=0.0-0.5), were prepared by solid state reaction technique and by nitrate-citrate combustion route, and were studied by XRD, SEM/EDS, TEM, EPR, dilatometry and electrical conductivity measurements. Employment of the combustion method was found to result in a significant decrease of zircon phase formation temperature, but also in a smaller grain size and somewhat lower densification on sintering. Overall solubility of Mg cations in zircon-type lattice of YVO_4 is however very limited and, independently of synthesis route, corresponds to $x \leq 0.1$. Acceptor-type substitution by magnesium is compensated by the formation of oxygen vacancies and results in a moderate increase of oxygen-ionic conductivity with respect to the parent yttrium vanadate. Combustion-synthesized ceramics showed higher conductivity compared to the samples prepared by conventional solid state reaction method.

T. H. Gayathri, A. A. Yaremchenko, K. Zakharchuk and Jose James, "Effect of magnesium addition on the structural, microstructural and electrical properties of YVO_4", J. Alloys and Compd. 672 (2016) 549-557

4.1. Introduction

Anionic conductors and more specifically oxide ion conductors receiving widespread interest and have been increasingly studied for many years because of their application in various devices with high economical attention such as solid electrolytes in solid oxide fuel cells (SOFCs), oxygen pumps, oxygen sensors, batteries, electrochromics, dense ceramic membrane for oxygen separation, membrane reactors for oxidative catalysis etc.[1-6] Oxygen sensors are crucial for combustion control whereas fuel cell is emerging as an efficient, clean and environmentally friendly electric power source. Apart from this, oxygen separation membranes are supposed to be potable oxygen source for medicine and catalytic oxidative process.[2] The scientific and technological significance of oxide ion conducting materials has increased appreciably and consequently, there have been a major thrust to conform and develop new materials that exhibit high ionic conductivity at lower temperatures. For attaining high ionic conductivity at lower temperature, it is needed to either improve the properties of the known compounds through suitable choice of effective dopants or by designing and developing new class of materials.[7] After the discovery of fast oxide conduction in YSZ, there has been a huge attraction towards the investigation of metal substitution with lower valent cations in order to create or increase charge-compensating oxygen vacancies which is considered as one the most acceptable approach for enhancing oxygen ion conductivity.[8] Because of the size and interaction of oxygen ions with the cationic network, high mobility can only be accomplished with classes of materials with appropriate structural features. The well known oxide ion conductors generally belong to fluorite, perovskite, pyrochlore, brownmillerite and aurivillius type structures.[7,9]

Recently, there has been a huge attraction for ionic conductivity in oxides of other structural types.[10,11] Significant research efforts have been carried out in the field of

zircon structured orthovanadates (AVO_4, A= trivalent metal ion) due to their large number of applications.[12] These materials show diverse application in various fields such as host materials for phosphors and high power lasers, counter electrodes in electrochromic devices, gas sensors, components of oxide fuel cell anodes, oxidative dehydrogenation of light alkanes etc.[13-15] As for the host lattice, yttrium orthovanadate (YVO_4) has been considered to be an attractive candidate for incorporation of several metal ions.[16] $YVO_4:Eu^{2+}$ is known to be a typical commercial red emitting phosphor which can be used in several places such as in cathode ray tubes, fluorescent lamps, X-ray detectors etc.[17,18] The conductivity of zircon- type $CeVO_4$ systems are well studied with different dopants.[15,19] Oxygen ion conductivity of zircon type $Ce_{1-x}A_xVO_{4+\delta}$ (A= Ca, Sr; x=0-0.2) was discussed by Tsipis et al.[15] They showed that the unusual behavior of conductivity is due to the presence of oxygen deficient CeO_2 separation while increasing the temperature to 1100°C and also reported that oxygen ionic conductivity is independent of A-site dopant content.

To date, the ionic conductivity of YVO_4 still has not been studied and reported. In this context, we have chosen YVO_4 as our parent material and explored the effect of substitution by alkaline earth ion such as magnesium on the structural, microstructural and electrical properties. The relatively good stability of Mg^{2+} allows for a study of its effects on the electrical and dielectric properties without the reduction of the substituent ion.[20] Many reports are available on the studies of acceptor-type Mg substitution on different cationic sites aiming to improve the transport properties.[21-23]

4.2. Effect of Mg substitution on the structural and electrical characterizations of YVO_4

The present work was aimed to study the effect of the addition of magnesium as a third cation into the host lattice of a tetragonal zircon type yttrium orthovanadate. The work was focused on the preparation of a new mixed ceramic oxide, viz; magnesium

yttrium vanadate ($Y_{1-x/2}Mg_xV_{1-x/2}O_{4-\delta}$, x = 0-0.5), via two synthetic procedures and a comparative study of their structural, microstructural and electrical properties

4.2.1. Experimental

Yttrium Vanadium oxide compounds (YVO_4) with different quantities of magnesium were prepared using solid state synthesis and combustion synthesis. The synthesized compositions are designated as YV and Mg_xYV, where YV stands for YVO_4 and Mg_xYV for $Y_{1-x/2}Mg_xV_{1-x/2}O_{4-\delta}$; and the numeral following Mg represents the particular amount of magnesium (x) in the $Y_{1-x/2}Mg_xV_{1-x/2}O_{4-\delta}$ (x=0-0.5) formula. The synthesis method adopted is abbreviated as SS for solid state synthesis and CS for combustion synthesis.

4.2.1.1. Solid State Synthesis (SS)

The Mg_xYV (x=0.0-0.5) samples were prepared through conventional solid state reaction method using high-purity magnesium carbonate hydroxide hydrate ($Mg_5(CO_3)_4(OH)_2$. $5H_2O$, 99.0%, Sigma-Aldrich, St. Louis, MO, USA), yttrium oxide (Y_2O_3, 99.0%, IRE, India) and vanadium pentoxide (V_2O_5, 99.6+%, Sigma-Aldrich) as the starting materials. Stoichiometric amount of the starting materials were weighed accurately, and mixed manually in acetone medium using agate mortar and pestle. The resultant mixture was then first calcined at 650°C/6h followed by calcinations at different temperatures (750-1000°C/6h) with intermediate grinding. These powders were then ground well and mixed with 4 wt% poly vinyl alcohol, PVA (molecular weight 72,000, BDH Lab suppliers, Poole, U.K), dried and ground well. Cylindrical disks of ~11 mm diameter and ~2-3 mm thickness were prepared by applying a pressure of 100 MPa by a uniaxial press. These cylindrical compacts were then sintered at 1250°C/6h with an intermediate soaking time of 600°C to expel the binder PVA.

4.2.2.2. Combustion Synthesis (CS)

The most adopted and traditionally accepted method for ceramic material preparation is solid state synthesis. But, it requires longer reaction time and high temperature firing to get complete diffusion, leading to larger average particle size and sometimes incomplete reaction. This may further lead to introduction of impurities or loss of some starting materials, during the repeated grinding and annealing, and finally to a compositional variation, affecting the properties of the materials.[24-26] Alternative synthetic routes to the traditional high temperature mixed metal oxide reaction route, such as wet chemical synthesis might be able to improve the physical properties of these materials. The citrate method (Pechini process), is one of the simple, low temperature synthetic methods that can efficiently produce many materials with very fine particles.

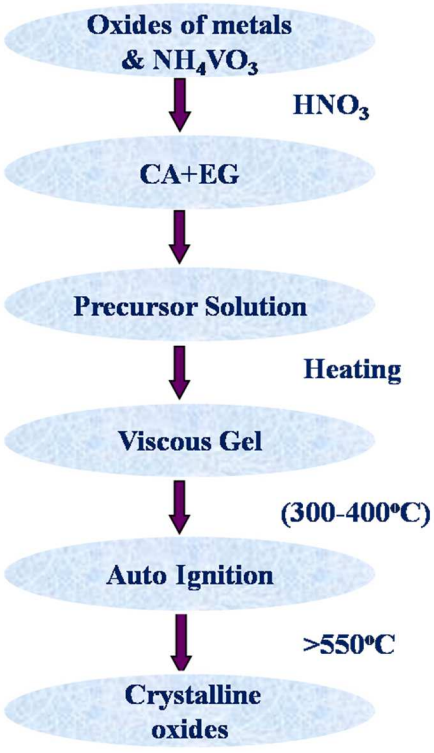

Figure 4.1: Flow chart showing the steps involved in CS method

This route involves the formation of a polymeric gel, which provide uniform mixing of metal ions at the molecular level and enable the preparation of homogeneous

multicomponent metal oxides in a nanometric scale. This method makes use of a hydroxycarboxylic acid, citric acid (CA), as the chelating agent, and a polyhydroxylalcohol, ethylene glycol (EG) for esterification. CA chelates with various cations and form a metal CA complex and its reaction with EG results in the formation of polymeric precursor resin, having the same metal stoichiometry as of the desired product. Further heating of this precursor will result in the formation of final products.[25-28] Steps involved in the preparation of ceramic materials by CS method are shown in fig. 4.1.

In the present case, a wet chemical synthetic route viz., Pechini process was adopted for the preparation of Mg_xYV (x=0-0.5). Samples were synthesized using magnesium nitrate hexahydrate ($Mg(NO_3)_2$. $6H_2O$, 98.0% from Alfa Aesar, UK), citric acid anhydrous ($C_6H_8O_7$, 99.5%, Merck specialities private limited, India), yttrium oxide (Y_2O_3, 99.0%, IRE, India), ammonium metavanadate (NH_4VO_3, 99.0%, Sigma-Aldrich, USA), and ethylene glycol ($C_2H_6O_2$, ≥99.0%, Merck, India) as the starting materials. Y_2O_3 was dissolved in nitric acid, and aqueous solutions of $Mg(NO_3)_2$. $6H_2O$ and NH_4VO_3 were added to it. Citric acid was added to the resulting aqueous solution. The solution was then heated to about 100°C under constant magnetic stirring, and ethylene glycol was added to this for esterification. During the synthesis, the solution underwent distinctive color change at different stages which was attributed to the change in oxidation states of vanadium ions. Finally, a light yellow color occurred.[29] The solution was further heated to about 300°C. During this heating the solvent evaporated and a polymeric resin containing the metal ions was formed. Subsequently this polymerized complex underwent auto ignition leading to the formation of voluminous fluffy powder with a dark color. This powder was then ground well and was calcined at various temperatures in the range 550°C-1100°C in air for 6 hours. The calcined powders were then ground well, mixed with PVA solution, dried and uniaxially pressed into cylindrical

discs of about 11 mm diameter and around ~2-3 mm thickness and sintered at 1200°C/6h in air.

The formation of required phase in the as obtained, calcined and sintered samples was studied at room temperature using X-ray powder diffractometer (X'pert PRO, PANalytical, Netherlands), using Ni filtered Cu Kα radiation. The coefficient of thermal expansion (CTE) was measured using thermomechanical analyzer (TMA/SS7300, SII Nano Technology Inc.). The microstructures of the polished and thermal etched compacts coated with palladium-gold mixture were studied using a scanning electron microscope (SEM) (JEOL-JSM, 5600 LV, Tokyo, Japan). Microstructural characterization along with elemental mapping of $Mg_{0.1}YV$ was performed by scanning electron microscopy (Hitachi SU-70) coupled with energy dispersive spectroscopy (EDS) (Bruker, Quantax 400detector). Particle shape and size of the samples prepared by CS method were studied using high resolution transmission electron microscope (HRTEM) (Tecnai G2, FEI, Netherlands). Powder samples calcined at 550°C were finely ground and dispersed in acetone by ultrasonication. A drop of this was cast onto carbon-coated copper grids for the TEM analysis. The densities of the sintered samples were obtained by Archimedes method using deionized water as the immersing medium. The oxidation state of vanadium was determined using electron paramagnetic resonance (EPR). The spectra of the samples were recorded using EPR spectrometer (Bruker EMX plus EPR spectrometer, Germany) operating at room temperature and at 9.87 GHz with 100.0 kHz field modulation. The electrical conductivity (σ) was determined by impedance spectroscopy (Agilent 4284A precision LCR meter, frequency range 20 Hz – 1 MHz) using disk-shaped sintered samples (thickness ~ 2 mm, ∅ ~ 10 mm) with porous Pt electrodes applied onto flat surfaces. The measurements were performed as function of temperature at 500-900°C in air.

4.2.2. Results and Discussion

4.2.2.1. Phase analysis and densification

X-ray diffraction study was primarily used to analyze the phase purity and crystal structure of the samples. The XRD pattern for $Mg_{0.1}YV$ (SS) and $Mg_{0.1}YV$ (CS) powder prepared by the two synthetic methods at different temperatures is given in fig. 4.2 (a) and (b) respectively.

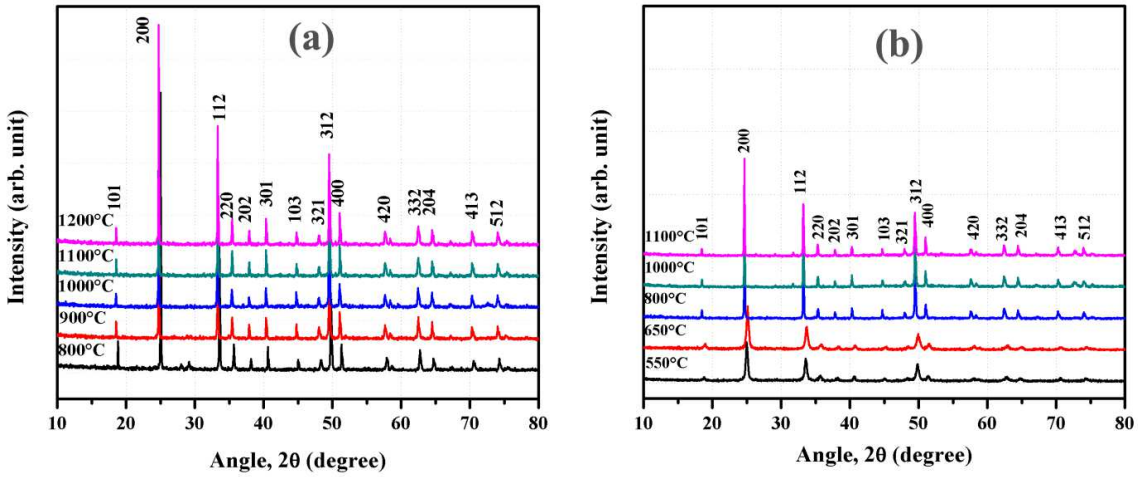

Figure 4.2: Powder X-ray pattern for $Mg_{0.1}YV$ synthesized by (a) SS (b) CS method

Fig. 4.2(a) represents the XRD pattern for SS $Mg_{0.1}YV$ samples heat-treated at a temperature range of 800°C-1200°C/6h. Complete phase formation is clearly visible starting from 1000°C. All the peaks can be indexed using tetragonal $I4_1/amd$ space group characteristic for zircon-type YVO_4 (ICDD PDF #82-1968). X-ray pattern of CS $Mg_{0.1}YV$ (Fig. 4.2(b)) consisted of amorphous like phases at lower temperatures. The XRD pattern obtained after calcination at 550°C showed the presence of zircon structured compound and no other crystalline phases coexisted, indicating the formation of a single phase material. Improved crystallinity is observed after calcinations at temperatures over 650°C. In this method metal ions are uniformly distributed in the polymeric resin and gives molecular level mixing of the elements, leading to the formation of the desired phase at lower temperatures compared to solid state route.[30]

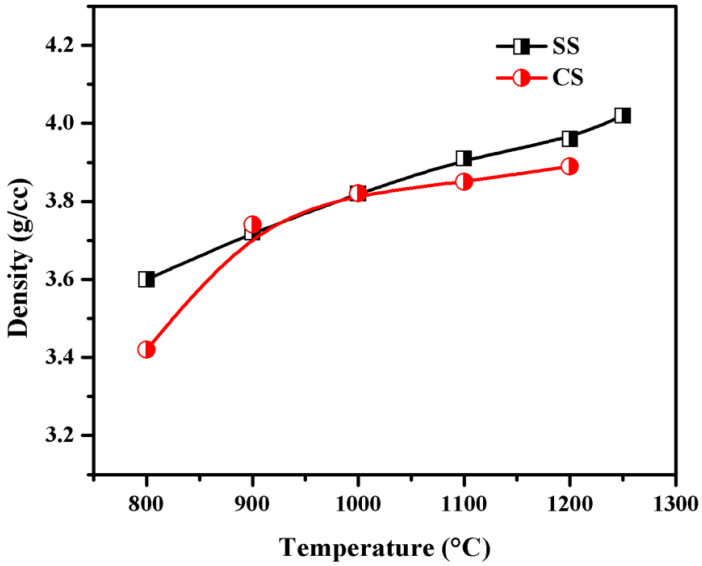

Figure 4.3: Variation of density as a function of temperature for $Mg_{0.1}YV$ synthesized by SS and CS method

Fig. 4.3 shows the density variation for $Mg_{0.1}YV$ heated at different temperatures between 800°C/6h to 1250°C/6h and 800°C/6h to 1200°C/6h for SS and CS samples respectively. For SS, the maximum density was obtained for the samples sintered at 1250°C/6h whereas for combustion synthesized it was 1200°C/6h. In both the cases, the materials showed similar trend with increasing temperature. Hence, temperature - time condition for optimum sintering was taken as 1250°C and 6 hour duration for SS and 1200°C and 6 hour for CS samples. Maximum relative density obtained for SS and CS samples were 96.9% and 93.7% respectively. The slightly lower values of density for the CS samples compared to the SS may be due to the presence of porosity arising because of the agglomerate formation by the smaller particles obtained in the former case. It is confirmed by the TEM as well as the SEM analysis shown in fig. 4.4, fig. 4.8 and fig. 4.9.

4.2.2.2. TEM analysis

Transmission electron microscope (TEM) is an analytical instrument that uses transmitted electrons instead of light to inspect the object at very fine resolutions (in nanometer range) and allowing magnifications of up to 100,000X. In TEM, a beam of

electrons is transmitted through an ultra-thin specimen, interacting with the specimen as it passes through. An image is formed from these interaction of the electrons transmitted through the specimen .This image is then magnified and focused onto an imaging device, such as a fluorescent screen, or can be detected by a CCD camera.[31]

Fig. 4.4 shows the TEM micrographs of powder samples of Mg_xYV (CS) calcined at 550°C/6h. The images showed grains of spherical morphology, with an average particle size below 50 nm. The powder samples were found to be agglomerated together even during the combustion reactions.[32]

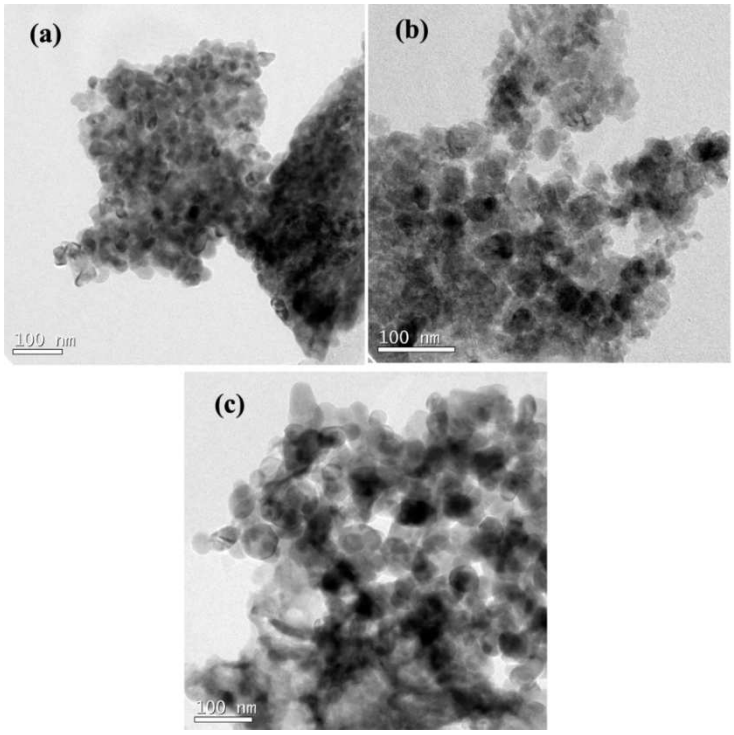

Figure 4.4: TEM images Mg_xYV (CS) samples heated at 550°C/6h
(a) x=0.0,(b) x=0.3 and (c) x= 0.5

4.2.2.3. Structural studies

Fig. 4.5 demonstrates the XRD patterns of Mg_xYV prepared by both synthetic methods. As can be seen, no evident difference is noticed in the spectra of the samples prepared by the two different approaches. The patterns for the samples prepared by SS and CS methods show single-phase compositions up to $x \leq 0.1$, and can be completely

indexed with ICDD PDF #82-1968. However, as the x value increased from 0.2 to 0.5 a minor impurity peak was observed at 2θ value of around 42°. This peak in the XRD patterns was attributed to the presence of MgO (periclase) secondary phase, and the peak intensity increased with increasing x in $Y_{1-x/2}Mg_xV_{1-x/2}O_{4-\delta}$. No obvious difference is noticed in the spectra of the samples prepared by the two different approaches.

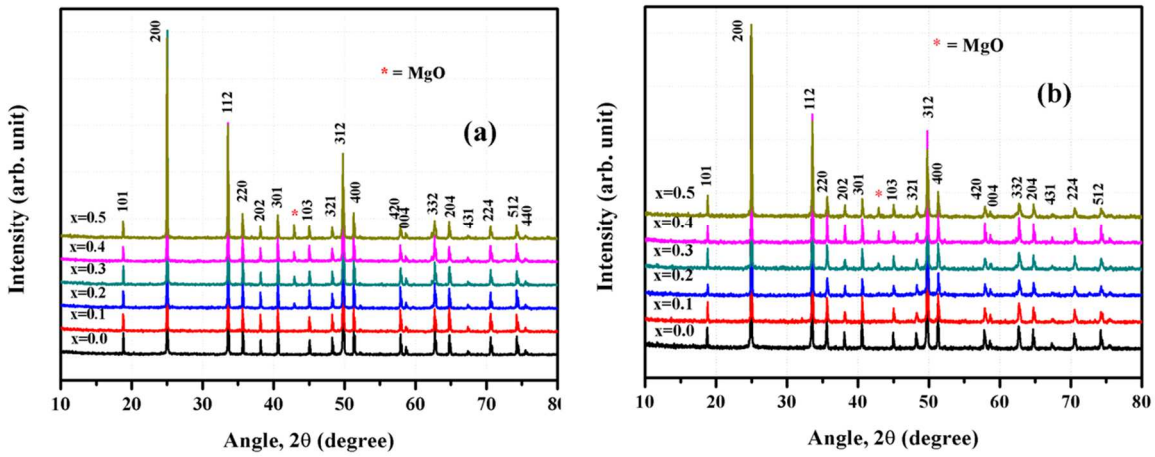

Figure 4.5 (a) & (b): Powder X-ray pattern of (a) Mg_xYV (SS) (x=0-0.5) sintered at 1250°/6h (b) Mg_xYV (CS) (x=0-0.5) sintered at 1200°C/6h

4.2.2.4. Structure refinement

Rietveld refinement of the solid state-synthesized YVO_4 and Mg-doped samples were carried out using X'pert Highscore Plus software. Refinement pattern obtained for $Mg_{0.1}YV$-SS sample is shown in fig. 4.6. The reported tetragonal zircon structure of YVO_4 with space group $I4_1/amd$ (141) was used as a starting model for the refinement. Here Y ions are at (4a: 0, ¾, ⅛) sites, V ions at (4b: 0, ¼, ⅜) sites and O is at (16h: x, y, z). Mg ions are assumed to be distributed either only in 4a or in 4b sites or between both 4a and 4b sites. Refinement of all the 3 possibilities was carried out. All of these gave results in the acceptable range. The model with Mg ion distribution in both sites (4a and 4b sites) produced a better fit. During the refinement process, oxygen was always considered with full occupancies, whereas yttrium, magnesium and vanadium occupancies were varied in accordance with the stoichiometry. Refinement parameters

obtained for YV and $Mg_{0.1}YV$ are listed in Table 4.1. The unit cell volume as well as the lattice parameters was found to decrease on substitution. This can be a consequence of insertion of Mg ions in to the lattice.

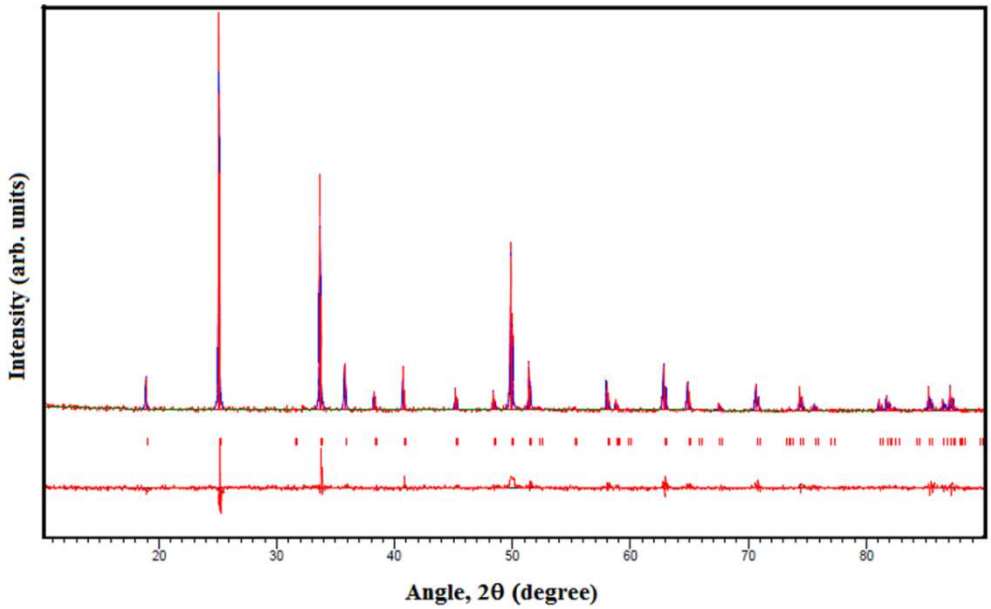

Figure 4.6: Rietveld refined XRD data for $Mg_{0.1}YV$ (SS)

Table 4.1: Crystallographic refinement parameters for $Y_{1-x/2}Mg_xV_{1-x/2}O_{4-\delta}$ (x=0.0 and 0.1)

Crystallographic parameters	**YVO_4**	**$Mg_{0.1}YV$**
Crystal System	Tetragonal	Tetragonal
Space group	$I4_1/amd$	$I4_1/amd$
Formula Sum	$Y_{4.00}V_{4.00}O_{16.00}$	$Y_{3.81}Mg_{0.38}V_{3.81}O_{16.00}$
Lattice Parameters		
a (Å)	7.1196(1)	7.1189(2)
c (Å)	6.2903(1)	6.2892(2)
V ($Å^3$)	318.84	318.73
ρ (g/cc)	4.25	4.16
R_p %	11.54	12.47
R_{wp}%	14.04	15.49
R_{exp}%	10.67	11.16
GOF	1.73	1.93

In fact, there is a considerable mismatch of ionic sizes (ionic radii: Y^{3+} (CN8) = 1.019 Å; V^{5+} (CN4) = 0.355 Å; V^{4+} (CN4) = 0.45 Å (extrapolated); Mg^{2+} (CN4) = 0.57 Å: and Mg^{2+} (CN8) = 0.89 Å[33]), so the solubility limit of Mg cations in either sublattice is expected to be limited. As per the XRD analysis (fig.4.5), the solid solution formation of

the Mg_xYV samples is found to be $x \leq 0.1$. The possible mechanisms of Mg incorporation into crystal lattice of YVO_4 may include:

$$1.\ xMgO \xrightarrow{YVO_4} (Y_{1-0.5x}Mg_{0.5x})(V_{1-0.5x}Mg_{0.5x})O_{4-x}$$

$$2.\ xMgO \xrightarrow{YVO_4} Y_{1-x}Mg_xVO_{4-0.5x} + 0.5xY_2O_3$$

$$3.\ xMgO \xrightarrow{YVO_4} YV_{1-x}Mg_xO_{4-1.5x} + 0.5xV_2O_5$$

or their combination, or segregation of some other impurities. As mentioned above, the results of refinement indicate the preference for the first mechanism within the solid solubility domain.

4.2.2.5. EPR analysis

Electron paramagnetic resonance (EPR) or otherwise known as Electron Spin Resonance (ESR) or Electron Magnetic Resonance (EMR) is a branch of spectroscopy in which radiation of microwave frequency is absorbed by molecules possessing electrons with unpaired electrons. This method is commonly used for analysing the structure of molecular ions or systems containing unpaired electrons having spin-degenerate ground states in the absence of magnetic field. In the case of solid state materials, EPR is used for understanding the symmetry of surroundings of the paramagnetic ion and the nature of its bonding to the nearest neighbouring ligands.

When a paramagnetic substance is kept in a steady magnetic field (H), the unpaired electrons in the outer shell have a tendency to align with the field. As a result the two fold spin degeneracy is removed. So the two energy levels $E_{1/2}$ and $E_{-1/2}$ are separated by $g\beta H$, where g is known as the gyro magnetic ratio which is the spectroscopic splitting factor and β is the Bohr magneton. As there is a finite chance for the transition between these two energy levels, a change in the energy can be stimulated by external radio frequency. When a microwave frequency (ν) is applied perpendicular to the direction of the field,

resonance absorption will arise between these two split spin levels. The resonance condition can be expressed as

$$h\nu = g\beta h$$

where h is the Planck's constant.

In order to satisfy the resonance condition, the values ν and H can be varied. Though, EPR studies are carried out under a constant frequency, ν, by varying H. For a free electron the g value is fixed as 2.0023. Since h and β are constants, one can calculate the g factor.

If the central metal ion also have a non-zero nuclear spin, I, then hyperfine splitting happens due to the interaction between the nuclear magnetic moment and the electronic magnetic moment. The measurement of g value and hyperfine splitting factor gives information about the electronic states of the unpaired electrons and also about the nature of the bonding between the paramagnetic ion and its surrounded ligands. The g value also has a dependence on the orientation of the molecules having the unpaired electron with respect to the applied magnetic field.[34]

Electron paramagnetic resonance (EPR) spectroscopy is useful technique for getting information about the nuclearity, elemental composition, and electronic structure of a paramagnetic centre.[35] Room temperature EPR spectra of solid state synthesized Mg_xYV consists of 8 lines with g value centered at ~1.98 and are due to V (IV) ion. Vanadium ions can have a wide range of oxidation states and among them most commonly encountered are V (IV) and V (V) states. V (V) having an outer electronic configuration $3p^63d^0$ which is diamagnetic in nature and EPR inactive, whereas the V (IV) has one unpaired electron in d orbital ($3p^63d^1$) is paramagnetic and EPR active. The strong absorption line seen in the spectra originates from the V (IV) paramagnetic centre, since the other ions present in the systems are diamagnetic in nature and will not contribute to

the EPR signals. The absorption lines arise due to the interaction of unpaired $3d^1$ electron of V (IV) with the electromagnetic field in the microwave region. V (IV) has an electronic spin of S=1/2 and magnetic nuclear spin of ^{51}V is I=7/2, there shall be an interaction between the corresponding magnetic moments leading to the hyperfine structure (hfs) in the EPR spectra. V (IV) has 2I+1=8 values of nuclear magnetic quantum numbers, m_1=-7/2, -5/2,-3/2.....+5/2,+7/2, and one can expect an hfs consisting of 8 lines corresponding to the 8 different values of m_1.[36] The existence of even a small number of paramagnetic centers should have a strong effect on the physical properties of the system which is in turn dependent on the high temperature treatment and also on the oxygen deficiencies. The reduction of V (V) may occur in the course of heat treatment as a result of oxygen losses from the lattice. The intensity of the EPR signal is an indicator of oxygen loss and has a direct relationship. The release of oxygen or the electron addition is needed for the reduction of V (V).[37] A typical EPR spectrum obtained for Mg_xYV (x=0.5) is shown in fig. 4.7. EPR studies have shown that Mg incorporation to YV lead to the reduction of V (V) to V (IV).

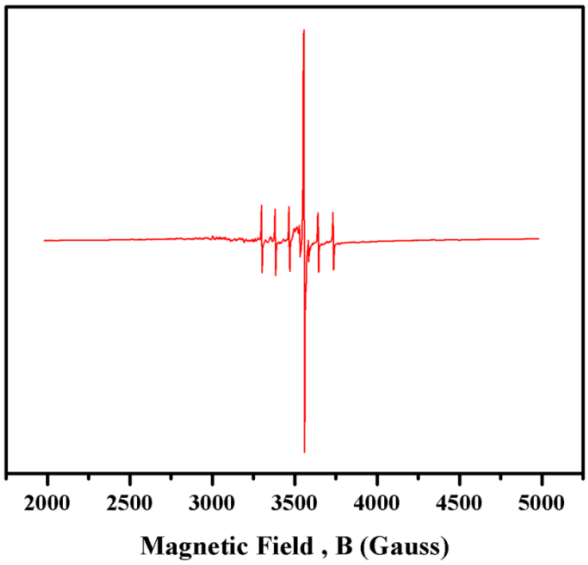

Figure 4.7: EPR spectrum of $M_{0.5}YV$ (SS) at room temperature

4.2.2.6. Surface morphology

In order to understand the microstructure of the samples, the sintered compacts were polished well and then thermally etched for 1 hour at temperature 50°C below the sintering temperature. The microstructures of the thermally etched Mg_xYV samples are shown in figs. 4.8 and 4.9. The grain sizes of all the samples were in the size range between ~2 µm and ~7 µm for CS and ~2 µm to 10 µm for SS samples. In both cases, Mg doping improved the grain growth to some extent under identical processing/sintering conditions. EDS analysis indicates the presence of some grains which are Mg enriched from $x \geq 0.2$ onwards. This confirms the presence of secondary phase (periclase) present in these samples, as indicated by the XRD data presented in fig. 4.5.

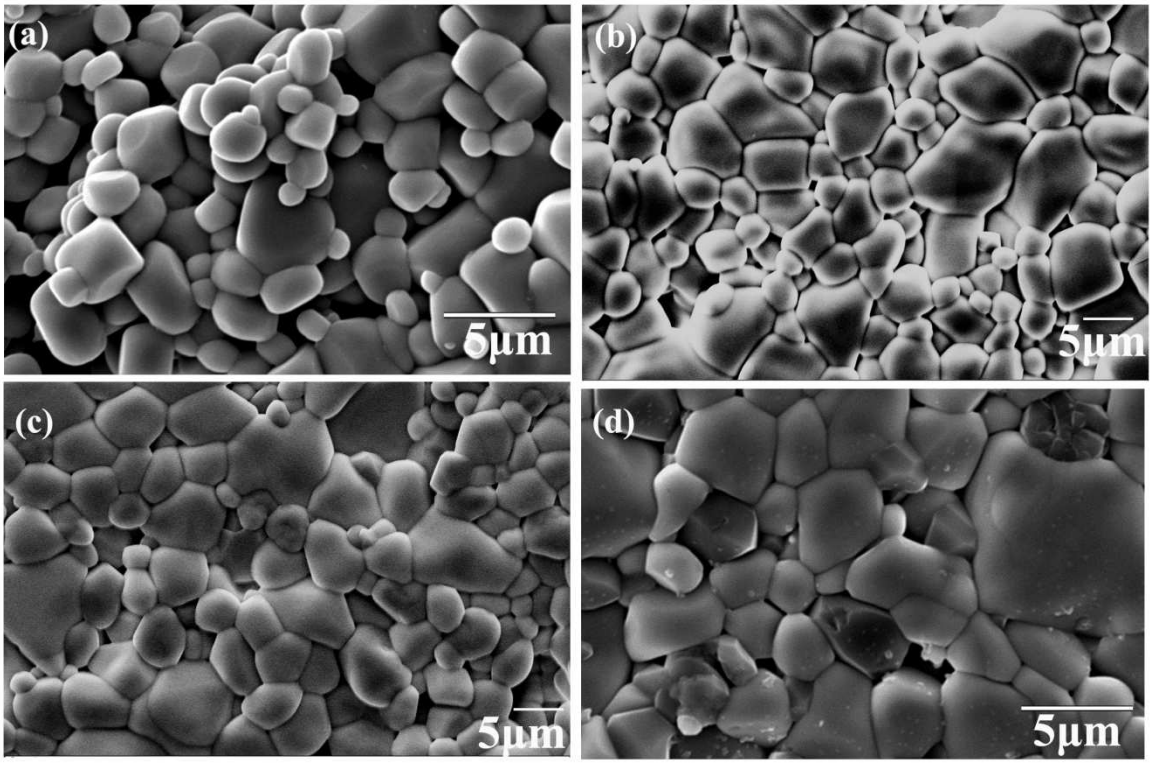

Figure 4.8: **SEM images of Mg_xYV (CS) sintered at 1200 °C/6h (a) x = 0.0, (b) x= 0.1, (c) x= 0.4, and (d) x= 0.5.**

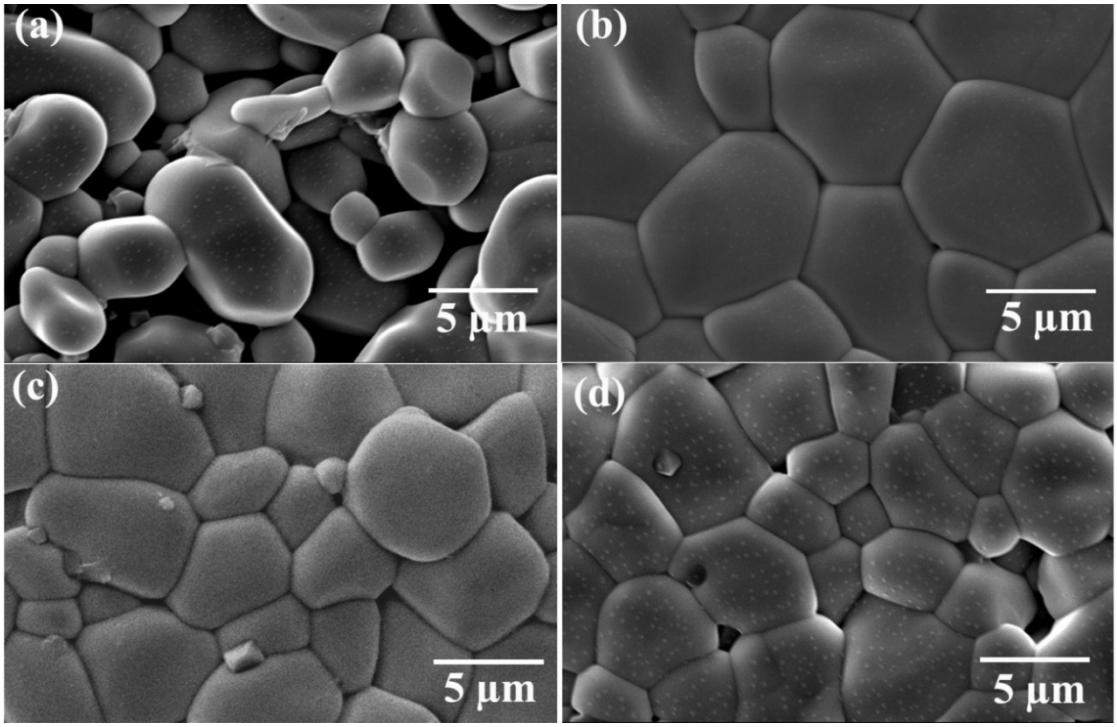

Figure 4.9: SEM images of Mg_xYV (SS) sintered at 1250 °C/6h (a) x = 0.0, (b) x= 0.1, (b) x= 0.4, and (d) x= 0.5.

The results of SEM/EDS analysis of fractured surface of $Mg_{0.1}YV$ (SS and CS) samples are shown in fig. 4.10. Elemental mapping indicated the presence of some segregation of MgO and a phase of Mg-V-O system. This indicates that even $Mg_{0.1}YV$ samples were not completely single-phase. The amount of impurity phases is however below the detection limit of XRD. EPR studies of the sample shown in fig. 4.7 also showed the presence of V in +4 oxidation state instead of +5.

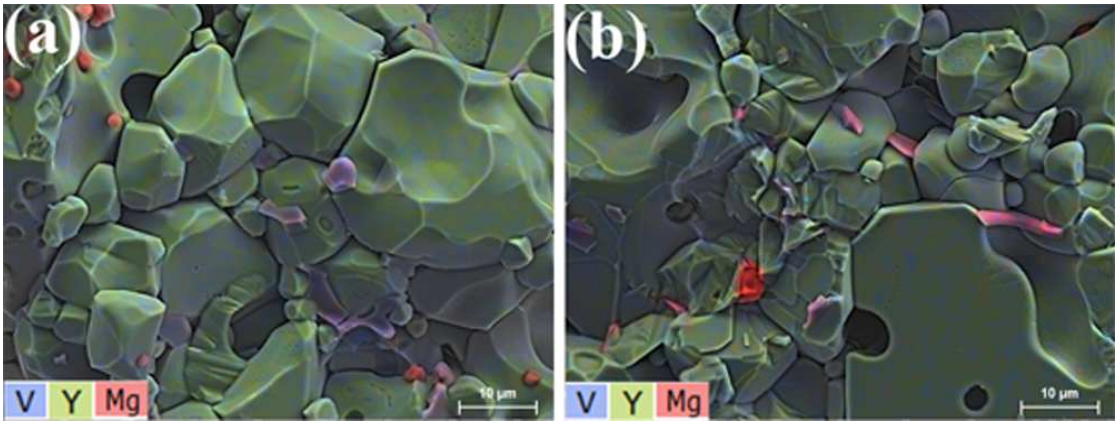

Figure 4.10: SEM micrographs with EDS elemental mapping of fractured cross sections of (a) $Mg_{0.1}YV$ (CS) (b) $Mg_{0.1}YV$ (SS)

Based on the XRD, SEM/EDS and EPR observations, one may conclude that magnesium substitutes preferably into vanadium sublattice, and, for x = 0.1, this is accompanied by a minor segregation of impurities which are not detectable by XRD. The impurity phases may include MgO and a phase of Mg-V-O system.

4.2.2.7. Density measurements

The collation of density of the sintered Mg_xYV (x=0.0-0.5) samples prepared through both processes is presented in fig. 4.11(a) and their corresponding relative density in fig. 4.11(b). Density shows a decreasing trend with increase in value of x due to the incorporation of magnesium. However, their sinterability increases as indicated by the increase in relative density (fig. 4.11(b)). Even though there is only a slight difference in the sintering temperature (1250°C/6h for SS and 1200°C/6h for CS); the densities of the samples are almost similar except for the parent YVO_4. The combustion-synthesized YVO_4 sample show somewhat lower density compared to YVO_4 prepared by solid state route, and this may be due to the highly agglomerated nature of the powders.

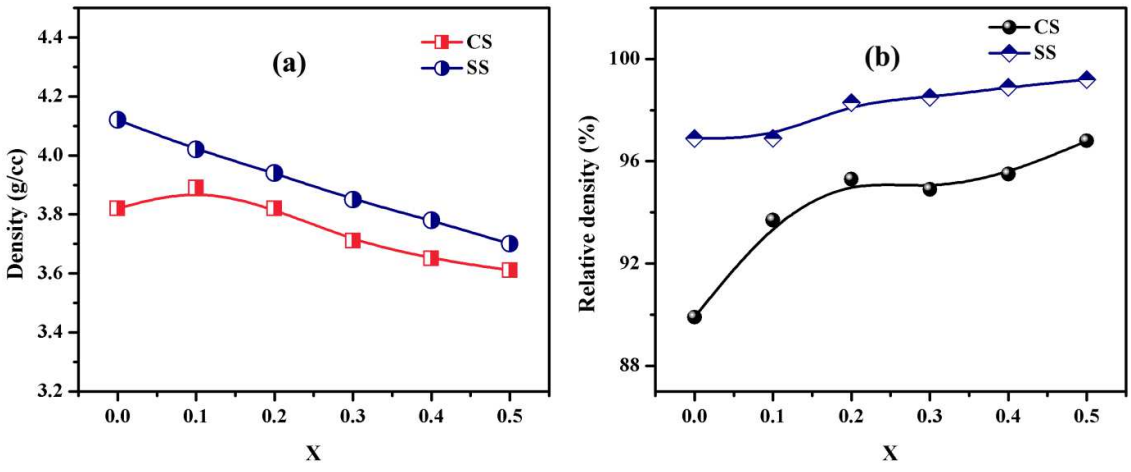

Figure 4.11: (a) Variation of density and (b) relative density as a function of x for Mg_xYV (x=0.0-0.5)

4.2.2.8. Electrical conductivity

Fig. 4.12 shows typical impedance spectra of Mg_xYV ceramics. The spectra comprised two signals: high-frequency semicircle corresponding to the bulk resistance (contributed by secondary phases) and low-frequency arc assigned to the electrode process. No grain boundary contribution could be distinguished in the studied temperature range.

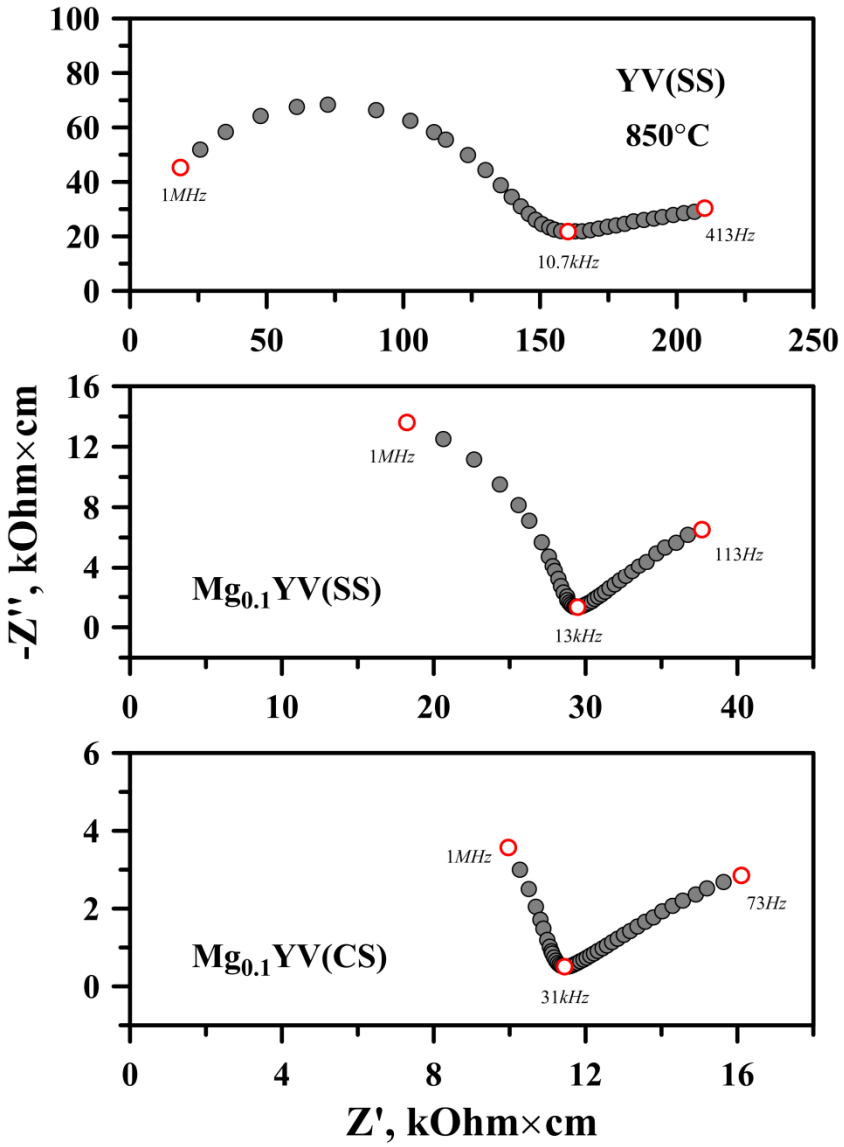

Figure 4.12: Examples of the impedance spectra of Mg_xYV ceramics collected in air at 850°C. Estimated capacitance values correspond to (4-8)×10^{-12} F/cm for the high-frequency process and increase with doping from ~3×10^{-7} to ~10^{-5} F/cm for the low-frequency arc.

Undoped YVO_4 is a semiconductor with comparatively low electrical conductivity in air, ~ 10^{-5} S/cm at 900°C (fig.4.13), and activation energy of 129 kJ/mol in the studied temperature range (Table 4.2). Although the nature of electrical transport in this material was never reported, the presence of electrode response in the impedance spectrum (fig. 4.12) implies an ionic contribution to the total electrical conductivity.

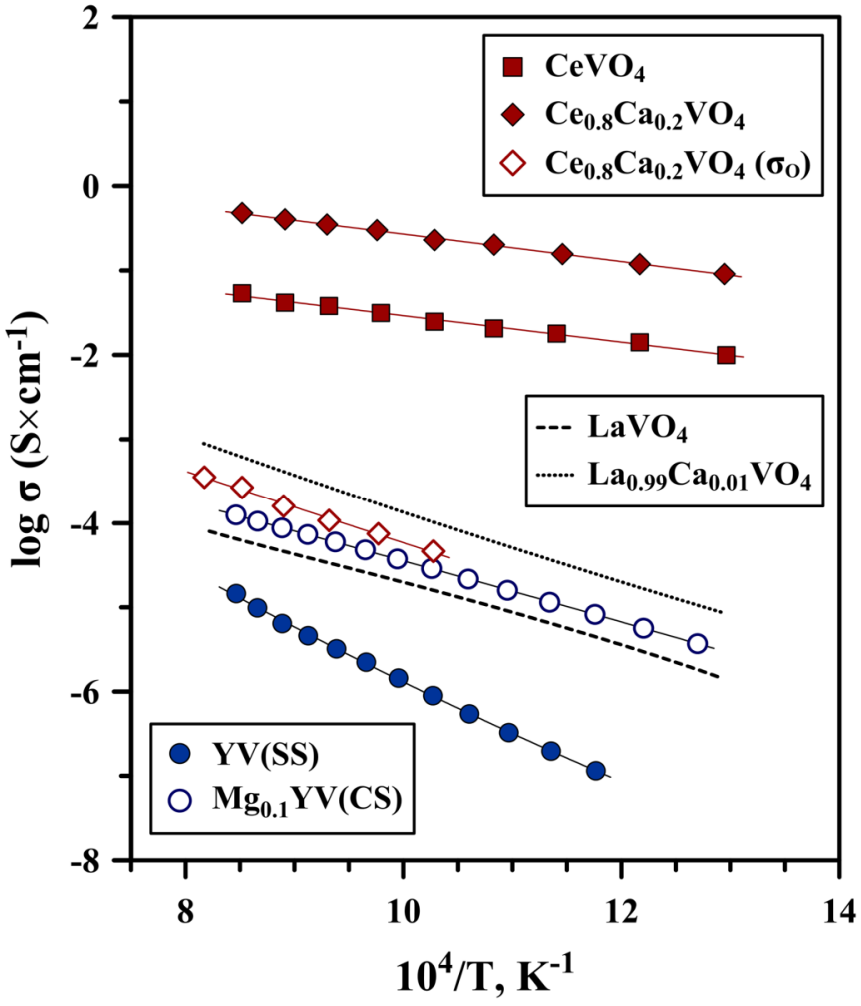

Figure 4.13: Total electrical conductivity of $LnVO_4$-based ceramics: YV and $Mg_{0.1}YV$ in air (this work), $La_{1-x}Ca_xVO_4$ in wet O_2 ($p(H_2O) \approx 0.025$ atm),[38] and $Ce_{1-x}Ca_xVO_4$ in air [39]. Literature data on partial oxygen-ionic conductivity (σ_O) of $Ce_{0.8}Ca_{0.2}VO_4$ in air[39] are also shown for comparison.

Minor doping with magnesium results in an increase of electrical conductivity of $Mg_{0.1}YV$ compared to the parent material, ~one order of magnitude at 900°C, accompanied with a decrease of activation energy to 77-82 kJ/mol at 500-900°C.

Whatever the mechanism of substitution, incorporation of magnesium cations into either yttrium or vanadium sublattices (or both) should be compensated by formation of oxygen vacancies thus promoting oxygen-ionic transport. The effect of acceptor-type doping on electrical properties of YVO_4 is therefore similar to that reported to calcium-substituted $LaVO_4$.[38] In both cases, however, the solubility of acceptor-type cations is very limited leading to only a moderate improvement of ionic conductivity (fig. 4.13).

Table 4.2: Activation energy for the total electrical conductivity of Mg_xYV ceramics in air

Composition	Temperature Range (°C)	E_A (kJmol^{-1})
YV (SS)	580-900	128.9 ± 1.6
$Mg_{0.1}YV$ (SS)	500-900	82.1 ± 0.4
$Mg_{0.3}YV$ (SS)	500-900	86.8 ± 1.1
$Mg_{0.5}YV$ (SS)	500-900	88.1 ± 0.3
$Mg_{0.1}YV$ (CS)	500-900	77.0 ± 0.1
$Mg_{0.3}YV$ (CS)	500-900	81.8 ± 0.4
$Mg_{0.5}YV$ (CS)	500-900	95.4 ± 1.1

Note: The activation energy was calculated using Arrhenius model $\sigma = (A_0/T)\exp(-E_A/(RT))$; given errors are standard errors.

Note that related zircon-type compound $CeVO_4$ is predominantly electronic conductor showing several orders of magnitude higher total conductivity compared to YVO_4 and $LaVO_4$ (fig. 4.13). The electronic transport in $CeVO_4$ is believed to be contributed by electron-hole hopping between cerium cations, with Ce^{4+} representing an electron-hole residing on cerium ion.[15,39] Contrary to YVO_4 and $LaVO_4$, charge compensation of acceptor-type substitution in $Ce_{1-x}A_xVO_4$ (A = Ca, Sr) occurs via partial oxidation of Ce cations ($Ce^{3+} \rightarrow Ce^{4+}$) thus leading to a further increase of p-type electronic conductivity [15,19,39,40] whereas ionic conductivity was found to be essentially independent of acceptor concentration.[15,39] Furthermore, the magnitude of oxygen-ionic conductivity in $Ce_{1-x}A_xVO_4$[15,39] is comparable to the total electrical conductivity of

$Mg_{0.1}YV$ and $La_{0.99}Ca_{0.01}VO_4$ (fig. 4.13), with similar values of activation energy. This may imply that ionic transport in these vanadates occurs via similar mechanism and is limited by a low concentration of oxygen vacancies. Still, $Mg_{0.1}YV$ ceramics show somewhat lower measured ionic conductivity compared to other acceptor-doped $LnVO_4$, at least partly due to the presence of minor phase impurities.

The role of phase impurities is further emphasized by the data shown in fig. 4.14. $Mg_{0.1}YV$ samples synthesized by combustion method were found to exhibit higher conductivity compared to their counterparts prepared by conventional solid state synthesis. This can be attributed most likely to better homogeneity and more uniform distribution of dopant cations in the host structure of CS samples. Magnesium doping beyond x = 0.1 resulted in progressive segregation of insulating impurity (MgO) and decline of the total electrical conductivity of Mg_xYV ceramics.

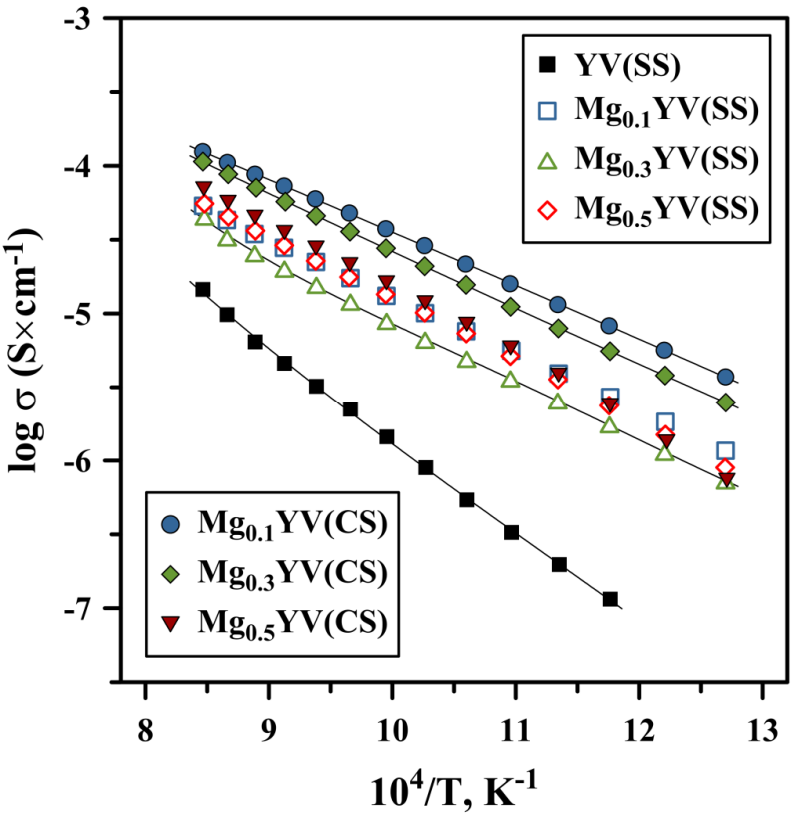

Figure 4.14: Temperature dependence of electrical conductivity of Mg_xYV ceramics in air

4.2.2.9. Thermal Expansion

Fig. 4.15 demonstrates the variation of coefficient of linear thermal expansion (CTE) of $Mg_{0.1}YV$ prepared by both synthetic methods from room temperature to 400°C. The average thermal expansion values are 4.7×10^{-6}/°C at 150-400°C for $Mg_{0.1}YV$ (CS) and 3.8×10^{-6}/°C for $Mg_{0.1}YV$ (SS) respectively. These values are in good agreement with the literature data on YVO_4[41] and other zircon-type vanadates.[15,39]

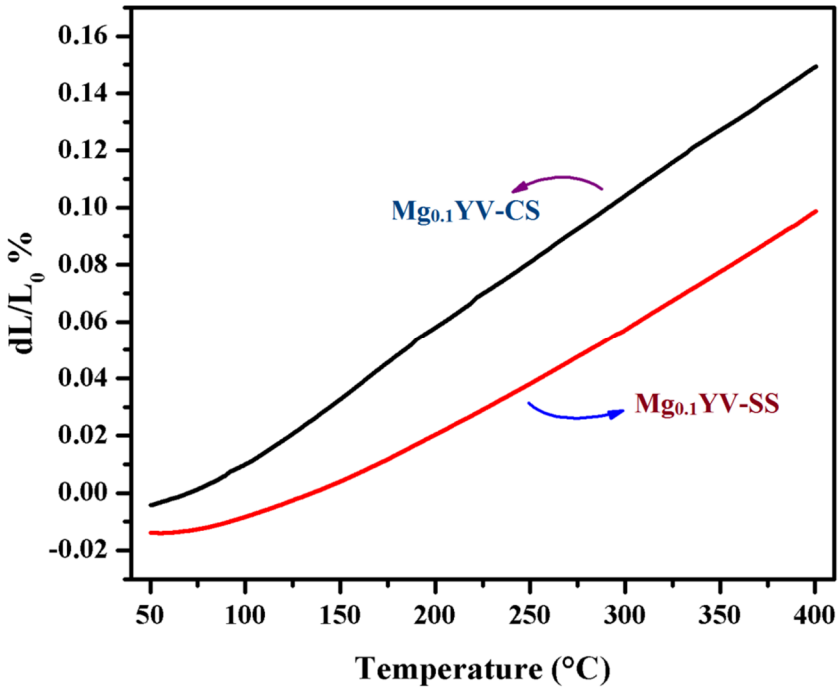

Figure 4.15: CTE curves for $Mg_{0.1}YV$ (SS and CS) samples in air.

4.2.3. Conclusions

- $Y_{1-x/2}Mg_xV_{1-x/2}O_{4-\delta}$, (x = 0.0-0.5) samples were prepared by adopting solid state reaction and combustion methods.
- Combustion synthesis showed zircon-type phase formation at lower temperatures compared to solid state method.
- XRD analysis indicated that single phase formation occurs up to x=0.1 in both cases, whereas the results of SEM/EDS analysis suggest slightly lower solubility limit of Mg in theYVO_4 lattice.
- TEM analysis indicated the smaller grain size of CS samples calcined at 550°C/6h.
- EPR analysis indicated the presence of paramagnetic centres and which may be due to the partial reduction of V(V) ions.
- Electrical measurements carried out in air demonstrated that the ionic conductivities of all Mg-doped samples are higher than that of undoped YVO_4.
- $M_{0.1}$YV-CS sample showed maximum conductivity (σ =1.25×10^{-4} S/cm at 900°C) among the prepared compositions due to its better homogeneity.

4.3. References

[1] P. R. Slater, J. E. H. Sansom, J. R. Tolchard, Development of apatite-type oxide ion conductors., *Chem. Rec.* 4 (2004) 373–384.

[2] T. Ishihara, H. Arikawa, H. Nishiguchi, Y. Takita, Fast oxide ion conductivity and oxygen tracer diffusion in doped $La_2GeO_{5-\delta}$, *Solid State Ionics* 154-155 (2002) 455–460.

[3] J. Boivin, Structural and electrochemical features of fast oxide ion conductors, *Int. J. Inorg. Mater*. 3 (2001) 1261–1266.

[4] T. Esaka, R. Tachibana, S. Takai, Oxide ion conduction in the Sm-substituted $PbWO_4$ phases, *Solid State Ionics.* 92 (1996) 129–133.

[5] P. Lacorre, The LPS concept, a new way to look at anionic conductors, *Solid State Sci.* 2 (2000) 755–758.

[6] R. V. Kumar, Application of rare earth containing solid state ionic conductors in electrolytes, *J. Alloys Compd.* 250 (1997) 501–509.

[7] S. Basu, P. S. Devi, H. S. Maiti, A potential low-temperature oxide-ion conductor $La_{2-x}Ba_xMo_2O_9$, *Appl. Phys. Lett.* 85 (2004) 3486–3488.

[8] R. D. Purohit, A. Chesnaud, A. Lachgar, O. Joubert, M. T. Caldes, Y. Piffard, L. Brohan, Development of new oxygen ion conductors based on Nd_4GeO_8 and Nd_3GaO_6, *Chem. Mater.* 17 (2005) 4479–4485.

[9] P. Lacorre, F. Goutenoire, O. Bohnke, R. Retoux, Y. Laligant, Designing fast oxide-ion conductors based on $La_2Mo_2O_9$, *Nature*. 404 (2000) 856-858.

[10] V. V. Kharton, F. M. B. Marques, A. Atkinson, Transport properties of solid oxide electrolyte ceramics: a brief review, *Solid State Ionics.* 174 (2004) 135–149.

[11] A. Najib, J. E. H. Sansom, J. R. Tolchard, P. R. Slater, M. S. Islam, Doping strategies to optimise the oxide ion conductivity in apatite-type ionic conductors, *Dalton Trans.* 19 (2004) 3106–3109.

[12] V. Panchal, S. Moreno, D. Perez, D. Errandonea, F. J. Manjon, P. Hernandez, A. Munoz, S. N. Achary, A. K. Tyagi, Zircon to monazite phase transition in $CeVO_4$: X-ray diffraction and Raman-scattering measurements, *Phys. Rev. B.* 84 (2011) 024111.

[13] V. Panchal, D. Errandonea, A. Segura, P. Hernandez, A. Munoz, S. Moreno, M. Bettinelli, The electronic structure of zircon-type orthovanadates: Effects of high-pressure and cation substitution, *J. Appl. Phys.* 110 (2011) 043723.

[14] N. Deligne, V. Gonze, D. Bayot, M. Devillers, Yttrium, lanthanide and mixed Y-Ln vanadates prepared from molecular precursors based on EDTA, Eur. *J. Inorg. Chem.* 2008 (2008) 896–902.

[15] E. V. Tsipis, V. V. Kharton, N. P. Vyshatko, A. L. Shaula, J. R. Frade, Stability and oxygen ionic conductivity of zircon-type $Ce_{1-x}A_xVO_{4+\delta}$ (A=Ca, Sr), *J. Solid State Chem.* 176 (2003) 47–56.

[16] L. Sun, Y. Zhang, J. Zhang, C. Yan, C. Liao, Y. Lu, Fabrication of size controllable YVO_4 nanoparticles via microemulsion-mediated synthetic process, *Solid State Commun.* 124 (2002) 35–38.

[17] J. Sun, J. Xian, Z. Xia, H. Du, Synthesis, structure and luminescence properties of $Y(V,P)O_4:Eu^{3+}$, Bi^{3+} phosphors, *J. Lumin.* 130 (2010) 1818–1824.

[18] Z. Xia, D. Chen, M. Yang, T. Ying, Synthesis and luminescence properties of YVO_4: Eu^{3+}, Bi^{3+} phosphor with enhanced photoluminescence by Bi^{3+} doping, *J. Phys. Chem. Solids.* 71 (2010) 175–180.

[19] A. Watanabe, Highly conductive oxides, $CeVO_4$, $Ce_{1-x}M_xVO_{4-0.5x}$ (M=Ca, Sr, Pb) and $Ce_{1-y}Bi_yVO_4$, with Zircon-type structure prepared by solid-state reaction in air, *J. Solid State Chem.* 153 (2000) 174–179.

[20] N. H. Zainol, S. M. Samin, L. Othman, K. B. Isa, W. G. Chong, Z. Osman, Magnesium ion-based gel polymer electrolytes: Ionic conduction and infrared spectroscopy studies, *Int. J. Electrochem. Sci.* 8 (2013) 3602–3614.

[21] G. C. Yin, H. Yin, L. H. Zhong, M. L. Sun, J. K. Zhang, X. J. Xie, et al., Crystal structure and ionic conductivity of Mg-doped apatite-type lanthanum silicates $La_{10}Si_{6-x}Mg_xO_{27-x}$ (x = 0–0.4), *Chin. Phys. B.* 23 (2014) 048202.

[22] T. Kinoshita, T. Iwata, E. Béchade, O. Masson, I. Julien, E. Champion, et al., Effect of Mg substitution on crystal structure and oxide-ion conductivity of apatite-type lanthanum silicates, *Solid State Ionics*. 181 (2010) 1024–1032.

[23] M. Li, M. J. Pietrowski, R. A. De Souza, H. Zhang, I. M. Reaney, S. N. Cook, et al., A family of oxide ion conductors based on the ferroelectric perovskite $Na_{0.5}Bi_{0.5}TiO_3$, *Nature Materials* 13 (2014) 31–35.

[24] S. Li, B. Bergman, Doping effect on secondary phases, microstructure and electrical conductivities of $LaGaO_3$ based perovskites, *J. Eur. Ceram. Soc.* 29 (2009) 1139–1146.

[25] L. Bi, E. Traversa, Synthesis strategies for improving the performance of doped-$BaZrO_3$ materials in solid oxide fuel cell applications, *J. Mater. Res.* 29 (2014) 1–15.

[26] C.H. Hervoches, M.C. Steil, R. Muccillo, Synthesis by the polymeric precursor technique of $Bi_2Co_{0.1}V_{0.9}O_{5.35}$ and electrical properties dependence on the crystallite size, *Solid State Sci.* 6 (2004) 173–177.

[27] T. Razpotnik, J. Maček, Synthesis of nickel oxide/zirconia powders via a modified Pechini method, *J. Eur. Ceram. Soc.* 27 (2007) 1405–1410.

[28] C. Robert, F. Ansart, C. Deloget, M. Gaudon, A. Rousset, Powder synthesis of nanocrystalline ZrO_2 – 8% Y_2O_3 via a polymerization route, *Mater. Res. Bull.* 36 (2001) 2083–2101.

[29] Raghvendra, R. K. Singh, A. S. K. Sinha, P. Singh, Investigations on structural and electrical properties of calcium substituted LSGM electrolyte materials for IT-SOFC, *Ceram. Int.* 40 (2014) 10711–10718.

[30] H. Zhang, X. Fu, S. Niu, G. Sun, Q. Xin, Low temperature synthesis of nanocrystalline YVO_4:Eu via polyacrylamide gel method, *J. Solid State Chem.* 177 (2004) 2649–2654.

[31] D. B. Williams, C. B. Carter, Transmission Electron Microscopy, Springer, 2009.

[32] K. Huang, J. B. Goodenough, Wet chemical synthesis of Sr- and Mg-doped $LaGaO_3$, a perovskite-type oxide-ion conductor, *J. Solid State Chem.* 136 (1998) 274–283.

[33] R. D. Shannon, Revised effective ionic radii and systematic studies of interatomic distances in halides and chalcogenides, *Acta Cryst.* A32 (1976) 751–767.

[34] M. A. Farrukh, Advanced aspects of spectroscopy, In Tech, 2012.

[35] N. Pathak, S. K. Gupta, A. Prince, R. M. Kadam, V. Natarajan, EPR investigation on synthesis of Lithium zinc vanadate using sol–gel-combustion route and its optical properties, *J. Mol. Struct.* 1056-1057 (2014) 121–126.

[36] J. E. Garbarczyk, P. Machowski, M. Wasiucionek, L. Tykarski, R. Bacewicz, A. Aleksiejuk, Studies of silver–vanadate–phosphate glasses by Raman, EPR and impedance spectroscopy methods, *Solid State Ionics.* 136-137 (2000) 1077–1083.

[37] N. Guskos, G. Zolnierkiewicz, J. Typek, M. Bosacka, EPR study of the $Me_2InV_3O_{11-\delta}$ (Me = Mg, Zn) compounds, *Rev. Adv. Mater. Sci.* 14 (2007) 125–129.

[38] M. Huse, T. Norby, R. Haugsrud, Proton conductivity in acceptor-doped $LaVO_4$, *J. Electrochem. Soc.* 158 (2011) B857–B865.

[39] E. V. Tsipis, M. V. Patrakeev, V. V. Kharton, N. P. Vyshatko, J. R. Frade, Ionic and p-type electronic transport in zircon-type $Ce_{1-x}A_xVO_{4\pm\delta}$ (A = Ca, Sr), *J. Mater. Chem.* 12 (2002) 3738–3745.

[40] C. T. G. Petit, R. Lan, P. I. Cowin, S. Tao, Structure and conductivity of strontium-doped cerium orthovanadates $Ce_{1-x}Sr_xVO_4$ ($0 \leq x \leq 0.175$), *J. Solid State Chem.* 183 (2010) 1231–1238.

[41] E. C. Subbarao, D. K. Agrawal, H. A McKinstry, C. W. Sallese, R. Roy, Thermal expansion of compounds of Zircon structure, *J. Am. Ceram. Soc.* 73 (1990) 1246-1252.

CHAPTER 5

ELECTRICAL PROPERTIES OF MONOVALENT (Li^+ and Ag^+) METAL DOPED $SmVO_4$

Undoped $SmVO_4$ and monovalent cation doped $SmV_{0.9}M_{0.1}O_{4\pm\delta}$ (M=Li and Ag) ceramic samples were prepared by solid state reaction technique and were characterized by XRD, SEM and electrical conductivity measurements using impedance spectroscopy. XRD analysis showed the formation of phase-pure materials with tetragonal zircon-type structure.SEM analysis indicated the variation of grain sizes from 0.5-2 μm for the doped ceramics and about 2-25 μm for the parent sample. A.C. impedance spectroscopy reveals that Li- and Ag- doping markedly improved the electrical conductivity of $SmVO_4$. Among the prepared ceramics, the highest conductivity is obtained for $SmV_{0.9}Ag_{0.1}O_{4\pm\delta}$ sample (~ 1.4×10^{-3} S/cm at 400°C) with activation energy of 73 kJ/mol in the studied temperature range of 130-470°C.

5.1. Introduction

Oxide ion conductors are important functional materials and are the subject of significant interest due to their relevant environmental friendly electrochemical applications in vital areas including solid oxide fuel cells, oxygen sensors, oxygen pumping devices etc..[1-6] Currently, Yttria stabilized zirconia (YSZ) is considered as the widely accepted oxide ion conductor, but technologically there is a need for new oxide ion conductors which can be operative at low temperature, due to the limited oxide ion conductivity of YSZ for utilization in electrochemical devices. Therefore, the development of highly conducting oxides, which is essential for applications occur at high temperature, can be considered as a highly demanding research subject.[7] In the past few decades, research was focussed on improving the performance of the existing oxide ion conductors and exploring new classes of materials.

As an important group of inorganic compounds, zircon-type rare earth orthovanadates ($REVO_4$) has been extensively studied for various applications. $REVO_4$ are materials of fundamental and technological significance due to their wide variety of functional properties. Important applications of $REVO_4$ includes solid electrolytes in SOFCs, cathodoluminescent materials, lithium ion batteries, as three way catalysts (TWCs), thermophosphors, scintillators, high-activity catalysts in oxidative dehydrogenation of propane and butane, laser-host materials, photocatalysis materials etc.[8-11] Generally, $REVO_4$ structures crystallize in two polymorphs: a tetragonal (t) zircon-type and monoclinic (m) monazite type.[8,12-14] As the larger rare earth elements have higher coordination number, they prefer to crystallize in the monazite type and the other orthovanadates prefer to crystallize in tetragonal zircon-type structure with space group $I4_1/amd$.[15,16] Tetragonal zircon structure has four formula units per unit cell and can be

described in terms of alternating edge-sharing REO_8 dodecahedra and VO_4 tetrahedra forming chains parallel to c-axis.[9]

Similar to the majority of $REVO_4$, samarium orthovanadate ($SmVO_4$) also crystallize in tetragonal zircon structure. In this structure, Sm atom is coordinated by eight oxygen atoms forming a triangular dodecahedra and V atom is tetrahedrally coordinated with four oxygen atoms.[9] In the last few years $SmVO_4$ based materials have been extensively studied as a potential candidate due to their unique properties and applications in various fields such as gas sensors[17] optical polarizers[18] catalysis[19] lithium intercalated electrodes[20] laser host materials[21] thin film phosphors[22] solar cells[23] and unusual magnetic materials[24]. However, the reports on electrical properties of zircon type $SmVO_4$ and related materials are very scarce. The effect of divalent cations on the electrical properties of known oxide conductors is studied well but that of monovalent cations are found to be comparatively rare. Monovalent metals like Ag and Li have larger size and lower valence than V ($r^{IV}(Ag^+)$ =1.00 Å, $r^{IV}(Li^+)$ = 0.590 Å and $r^{IV}(V^{5+})$ =0.355 Å).[25] To date, only a few reports are available on the influence of Ag and Li-doping on the electrical properties of ionic conductors. Liu et al.[3] reported the enhancement of ionic conductivity by Ag-addition in the lead-free ferroelectric material, $Bi_{0.5}Na_{0.5}TiO_3$ (BNT). They have carried out the conductivity measurement by varying the sintering atmospheres and found that the air sintered $Bi_{0.5}Na_{0.5}Ti_{0.9}Ga_{0.1}O_{3-\delta}$@1wt%$Ag_2O$ (A-BNTG) exhibits a higher conductivity in nitrogen while dramatic decrease in air, indicating an n-type contribution to the conductivity while the nitrogen sintered samples (N-BNTG) showed grain and grain boundary contribution to the total conductivity. The bulk conductivity of N-BNTG increased by almost 2800 times for A-BNTG at 502°C. Microwave assisted synthesis of bismuth vanadates with different cationic substitution (Ag^+, Mn^{4+}, Ga^{3+}, Y^{3+}, and Ce^{4+}) was reported by Vaidhyanathan et al.[26] Among which higher ionic conductivity

was obtained for $Bi_2(V_{0.9}Ag_{0.1})O_{5.3}$ and $Bi_2(V_{0.9}Mn_{0.1})O_{5.35}$ systems. Sharma et al.[7] discussed the influence of oxide ion conductivity by the substitution of Li for V in the $Bi_4V_2O_{11}$ system. Li and Ag –doping on the ionic conductivity of $Bi_2VO_{5.5}$ was reported by Taninouchi et al.[27] Temperature dependence of the electrical conductivity values of the $Bi_2(V_{0.95}Li_{0.05})O_{5.4}$ and $Bi_2(V_{0.9}Li_{0.1})O_{5.3}$ found to be 2 orders of magnitude higher than the values obtained by Sharma et al.[7] According to their report, Li and Ag-doping improved the conductivity of $Bi_2VO_{5.5}$ below 570 °C and also the conductivity values are found to be higher than the well known oxide ion conductors like YSZ [28]SDC[29] and LSGM[1].

5.2. Electrical properties of monovalent (Li^+ and Ag^+) metal doped $SmVO_4$

The objective of the present study is to synthesize monovalent metals such as Li and Ag-doped $SmVO_4$ system and to explore its electrical characteristics with the support of structural and microstructural analysis.

5.2.1. Experimental

Polycrystalline ceramic samples were synthesized by adopting conventional solid state method. Prepared compositions were abbreviated as SV, SVA and SVL for samarium vanadate, silver doped ($SmV_{0.9}Ag_{0.1}O_{4\pm\delta}$) and lithium doped ($SmV_{0.9}Li_{0.1}O_{4\pm\delta}$) doped samarium vanadate respectively.

High purity Sm_2O_3 (99.0%, IRE, India), Li_2CO_3 (>99%, Sigma-Aldrich), Ag_2O (>99%, Sigma-Aldrich) and V_2O_5 (99.6+%, Sigma-Aldrich) were used as the starting reagents. The powders were weighed accurately and mixed thoroughly using agate mortar and pestle using acetone as the mixing medium. The resultant mixtures for the compositions SVA and SVL were then precalcined at 400°C for 4 hours first followed by calcinations at different temperatures with proper intermediate grindings. Calcined powders of all the samples were then pressed uniaxially at 100 MPa into disk-shaped

compacts and sintered for 4 hours at 750°C for $SmV_{0.9}Li_{0.1}O_4$ and at 700°C for $SmV_{0.9}Ag_{0.1}O_4$. Sintered compact of SV was prepared by following the procedures explained in section 2.2.1.1.of Chapter 2. During the process of sintering, the pellets were properly covered by the powders of the same cation composition to minimize possible sample losses. The density of sintered samples was measured by Archimedes method using deionized water as immersion medium.

Powder X-ray Diffraction patterns were collected using PANalytical X'pert Pro diffractometer (Ni-filtered Cu-Kα radiation). Surface morphology of the sintered, polished and thermally etched compacts coated with palladium–gold mixture was performed with the aid of a scanning electron microscope (SEM, JEOL JSM-5600 LV). Electrical conductivity (σ) was determined in controlled atmospheres by means of impedance spectroscopy (Agilent 4284A precision LCR meter, frequency range 20 Hz-1 MHZ) using disc shaped sintered samples (thickness ~2 mm, ∅ ~ 10 mm)with porous Pt electrodes were painted onto the flat surfaces of the polished ceramic samples. The measurements were performed as a function of temperature at 120-550°C range.

5.2.2. Results and Discussion

5.2.2.1. Phase Analysis

Fig. 5.1(a) and (b) shows the XRD pattern for calcined samples of SV, SVA and SVL. All peaks in the XRD patterns can be assigned to a tetragonal symmetry of $SmVO_4$ without the indication of any other crystalline by-products, displaying the formation of a single phase of tetragonal zircon-type structure with space group $I4_1/amd$. All the reflections are in agreement with ICDD PDF #01-074-8274 of $SmVO_4$. The well resolved diffraction patterns indicate the high crystallinity of the prepared samples.

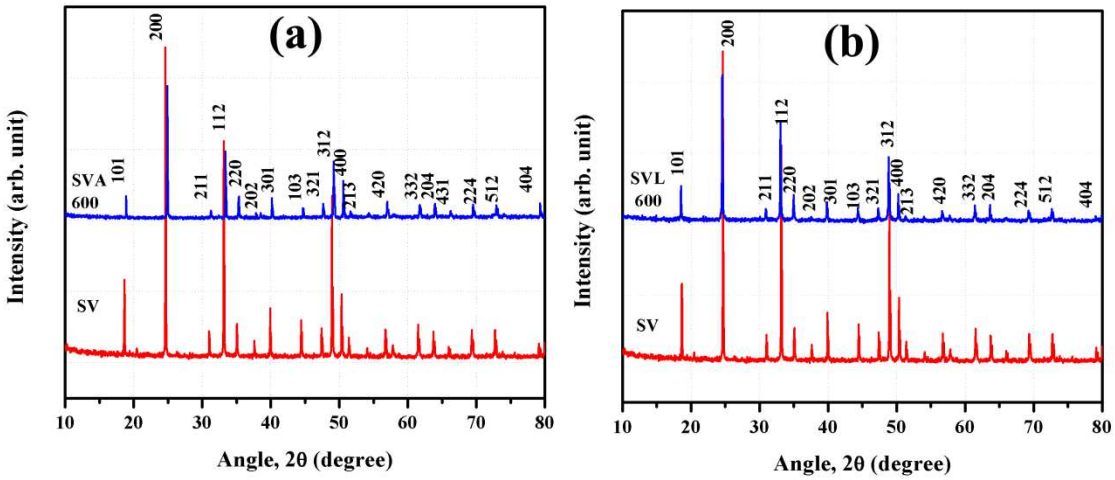

Figure 5.1: XRD pattern for the samples (a) SVA and (b) SVL compared with SV

5.2.2.2. Microstructural analysis and densification

Fig. 5.2 (a), (b) and (c) represents the SEM micrographs of polished and thermal etched surfaces of SVL and SVA respectively. Grain size of the samples varies in the range 0.5-2 μm for the doped ceramics and about 2-25 μm for the SV sample. Density obtained for the materials are listed in Table 5.1.

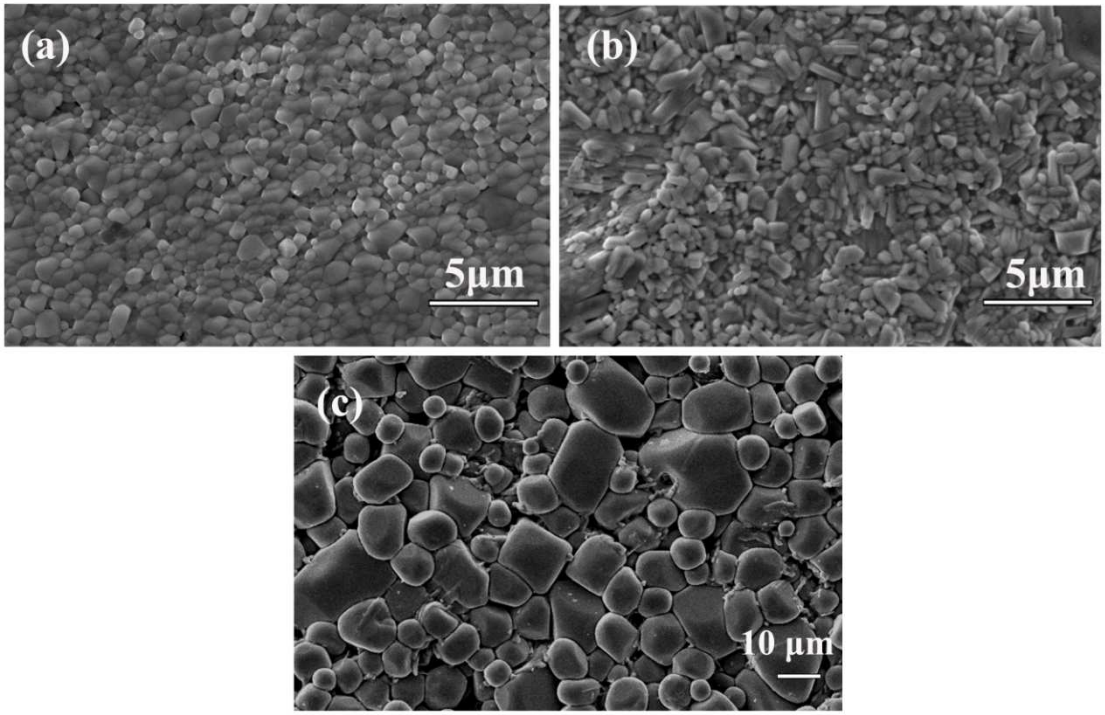

Figure 5.2: Surface morphology of sintered samples (a) SVL and (b) SVA and (c) SV

Relative densities of the sintered ceramics samples are summarised in Table 5.1. SV ceramics was found to be comparatively porous, whereas the doped ceramics had relative density higher than 90%.

Table 5.1: Relative Densities of the sintered ceramics

Composition	Relative Density %
SV	81
SVA	95
SVL	91

5.2.2.3. Electrical Conductivity

Fig. 5.3 shows typical impedance spectra of the prepared ceramics. For all compositions, the spectra comprised of two major contributions: high-frequency semicircle was assigned to the bulk resistance and the low-frequency contribution was attributed to the electrode process. No grain boundary contribution could be noticed in the studied temperature range.

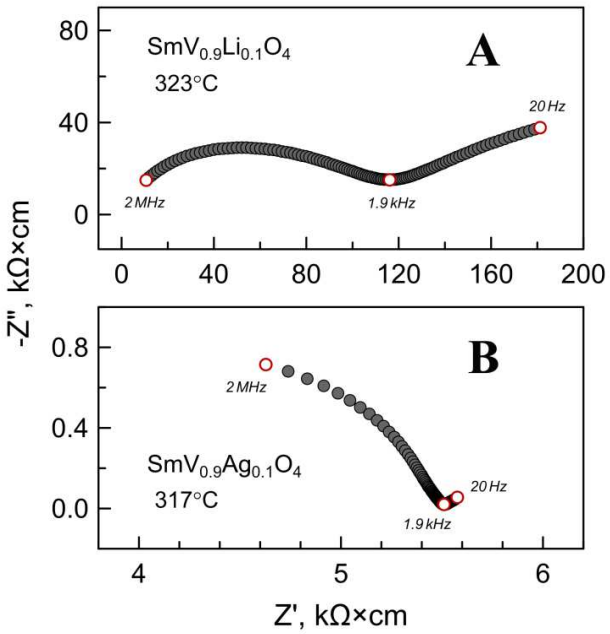

Figure 5.4: Impedance spectra of (A) SVL and (B) SVA

Temperature dependence of electrical conductivity of the prepared ceramics was studied and is shown in fig 5.5. Although the nature electrical transport in these materials

was never reported, the presence of electrode semicircle in the impedance plot (fig. 5.4) implies an ionic contribution to the total electrical conductivity. All the materials exhibit semiconducting behaviour in air (fig 5.5): the values of activation energy of electrical conductivity are listed in Table 5.2. The temperature dependent conduction mechanism in these materials obeys Arrhenius equation, and the activation energies are calculated from the slopes of the fitted straight lines of conductivity –temperature plot.

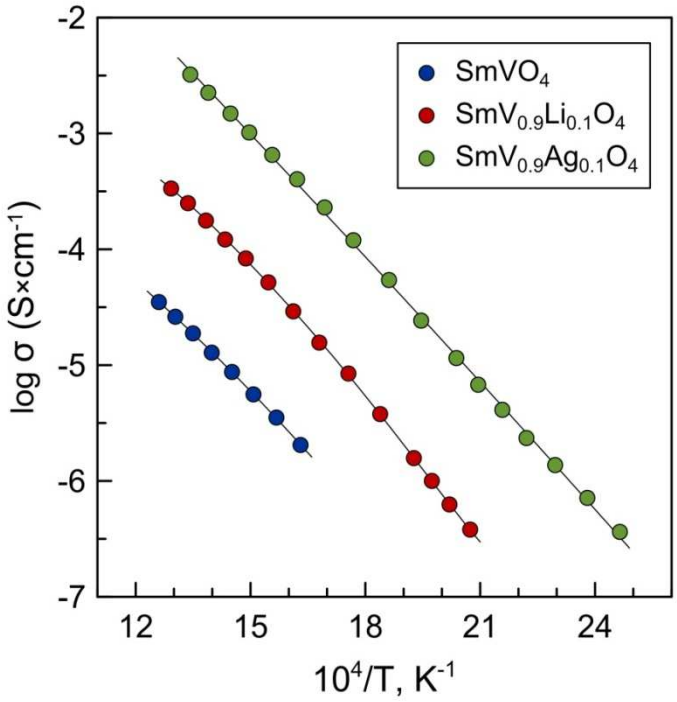

Figure 5.5: Temperature dependence of electrical conductivity of the prepared ceramics

Table 5.2: Activation energy of electrical conductivity of the samples in air

Composition	T, °C	E_A, kJ/mol
SV	340-520	69.5 ± 0.6
SLV	210-500	78.0 ± 1.0
SAV	130-470	73.1 ± 0.4

Conductivity measurements indicated that there was a significant dependence of electrical conductivity of the prepared ceramics on temperature and composition. The conductivity of SV without any dopant was very low and the value was ~5.6×10^{-6} S/cm

at 400°C. Minor doping with lithium and silver results in considerable increase of electrical conductivity of SVL and SVA samples compared to the parent material SV. SVL and SVA samples show conductivity higher than 10^{-4} S/cm and 10^{-3} S/cm respectively at temperature as low as 400°C with activation energy of 78 kJ/mol (SVL) and 73 kJ/mol (SVA) in the studied temperature range. The most likely reason for the considerable conductivity enhancement of SVL and SVA system may be due to the increased concentration of interstitial charge carriers in the zircon host structure, resulted upon the doping with monovalent cations. Whatever the mechanisms of electrical transport (by oxygen-ionic, or cationic, or mixed) acceptor-type doping by Li and Ag significantly improved the electrical conductivities of the parent material. The conductivity of SVA looks to be high is expected to be purely oxygen-ionic, available data are however insufficient to explain this.

It is well known that RE-doped ceria formed a family of solid electrolytes with outstanding conductivity properties compared with the commonly used YSZ, where the ionic conductivity takes place above 1073K, ceria based materials shows highest conductivity in fact at much lower temperatures. The conductivity in ceria based materials occurs via oxygen diffusion through the oxygen vacancies introduced by substituting Ce^{4+} with RE^{3+}. Among the lanthanides suitable dopants selected in terms of ionic conductivity of ceria system is Gd (GDC) and Sm (SDC).[30] Another well known oxide ion conductor as per the literatures is perovskite type $LaGaO_3$ doped with Sr and Mg (LSGM) for the La and Ga sites respectively. These materials exhibits higher oxide ion conductivity and can be comparable with the GDC. Taking this in to account we have made a comparison of temperature dependent electrical conductivities of these materials with the conductivity of the ceramic oxides prepared in this work.[31,32]

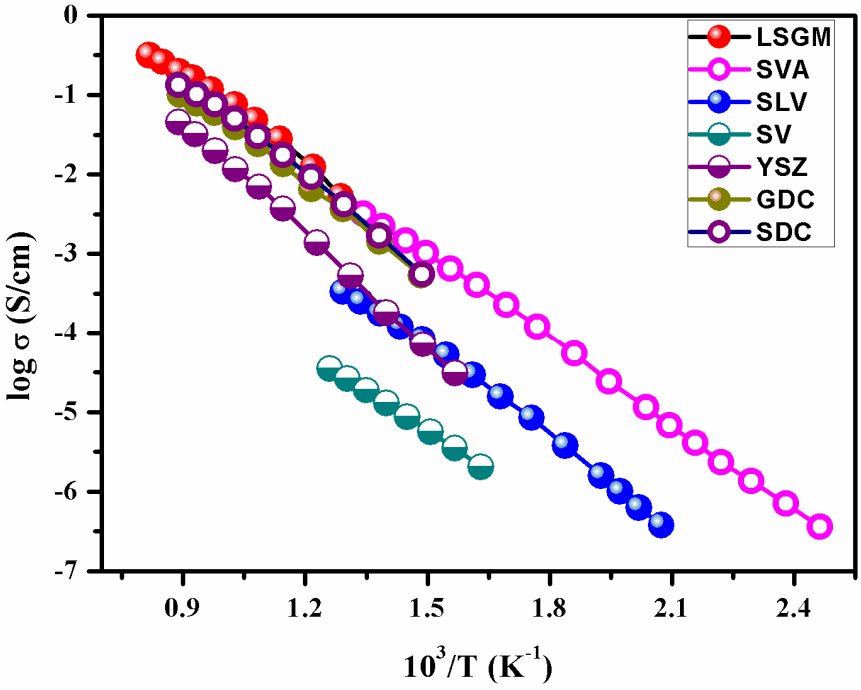

Figure 5.6: Comparison of temperature dependent electrical conductivity of SV, SVL and SVA (this work) with YSZ [28], LSGM [1], SDC and GDC[29].

Fig. 5.6 shows comparison of temperature dependence of electrical conductivity of the prepared ceramics with the conductivities of other oxide ion conductors $(ZrO_2)_{0.92}(Y_2O_3)_{0.08}$ (YSZ)[28], $Ce_{0.85}Gd_{0.15}O_{1.875}$ (GDC), $Ce_{0.85}Sm_{0.15}O_{1.875}$ (SDC)[29] and $La_{0.8}Sr_{0.2}Ga_{0.8}Mg_{0.2}O_3$ (LSGM)[1]. The conductivity of SVA at 450°C is ~1 order of magnitude higher than YSZ which is the most popular solid electrolyte and is comparable to SDC and GDC and the well known as the best oxide ion conductor LSGM. The value obtained for SVL also can be comparable to YSZ at 450°C.

5.2.3. Conclusions

- Undoped and monovalent Ag- and Li- doped $SmV_{1-x}M_xO_{4\pm\delta}$ (M= Ag and Li) ceramics were prepared by solid state reaction method.
- XRD analysis indicated the formation of single-phase materials with tetragonal zircon-type structure
- SEM analysis shows the variation of grain sizes 0.5-2 μm for the doped ceramics and about 2-25 μm for the parent sample.
- Electrical conductivity measurement carried out in air demonstrated that the conductivities of the doped samples are higher than that of undoped $SmVO_4$.
- SVA sample showed maximum conductivity ($\sigma = 3.2 \times 10^{-3}$ S/cm at 470°C) among the prepared compositions.
- The conductivity of the SVA ceramics is higher than the well known oxide ion conductors YSZ and can be comparable to SDC, GDC and LSGM.

5.3. References

[1] T. Ishihara, H. Furutani, M. Honda, T. Yamada, T. Shibayama, T. Akbay, et al., Improved oxide ion conductivity in $La_{0.8}Sr_{0.2}Ga_{0.8}Mg_{0.2}O_3$ by doping Co, *Chem. Mater.* 11 (1999) 2081–2088.

[2] C. Tealdi, G. Chiodelli, L. Malavasi, G. Flor, Effect of alkaline-doping on the properties of $La_2Mo_2O_9$ fast oxygen ion conductor, *J. Mater. Chem.* 14 (2004) 3553–3557.

[3] X. Liu, H. Fan, J. Shi, L. Wang, H. Du, Enhanced ionic conductivity of Ag addition in acceptor-doped $Bi_{0.5}Na_{0.5}TiO_3$ ferroelectrics, *RSC Adv.* 6 (2016) 30623–30627.

[4] J. Boivin, Structural and electrochemical features of fast oxide ion conductors, *Int. J. Inorg. Mater.* 3 (2001) 1261–1266.

[5] R.V. Kumar, Application of rare earth containing solid state ionic conductors in electrolytes, *J. Alloy. Compd.* 250 (1997) 501–509.

[6] P. Che, Q. Bo, J. Feng, Q. Wang, X. Cao, J. Meng, Study on structure and oxide ionic conductivity for new compound $Ce_{6-x}Ln_xMoO_{15-\delta}$, *J. Alloy. Compd.*408- 412 (2006) 645–648.

[7] V. Sharma, A. K. Shukla, J. Gopalakrishnan, Effect of aliovalent-cation substitution on the oxygen-ion conductivity of $Bi_4V_2O_{11}$, *Solid State Ionics*. 58 (1992) 359–362.

[8] Z. Xu, C. Li, Z. Hou, C. Peng, J. Lin, Morphological control and luminescence properties of lanthanide orthovanadate $LnVO_4$ (Ln = La to Lu) nano-/ microcrystals via hydrothermal process, *CrystEngComm.* 13 (2011) 474–482.

[9] C. Popescu, A. B. Garg, D. Errandonea, J. A. Sans, P. Hernández, S. Radescu, et al., Pressure-induced phase transformation in zircon-type orthovanadate $SmVO_4$ from experiment and theory, *J. Phys. Condens. Matter.* 28 (2016) 035402.

[10] D. Errandonea, S.N. Achary, J. Porres, A. K. Tyagi, Pressure-induced transformations in $PrVO_4$ and $SmVO_4$ and isolation of high-pressure metastable phases, *Inorg. Chem.* 52 (2013) 5464–5469.

[11] T. H. Gayathri, A. A. Yaremchenko, K. Zakharchuk, J. James, Effect of magnesium addition on the structural , microstructural and electrical properties of YVO_4, *J. Alloy. Compd.* 672 (2016) 549–557.

[12] C. Yu, M. Yu, C. Li, C. Zhang, P. Yang, J. Lin, Spindle-likelanthanide orthovanadate nanoparticles: Facile synthesis by ultrasonic irradiation, characterization, and luminescent properties, *Cryst. Growth Des.* 9 (2009) 783–791.

[13] W. Fan, X. Song, S. Sun, X. Zhao, Microemulsion-mediated hydrothermal synthesis and characterization of zircon-type $LaVO_4$ nanowires, *J. Solid State Chem.* 180 (2007) 284–290.

[14] Y. Oka, T. Yao, N. Yamamoto, Hydrothermal synthesis of lanthanum vanadates: Synthesis and crystal structures of Zircon-type $LaVO_4$ and a new compound LaV_3O_9, *J. Solid State Chem.* 152 (2000) 486–491.

[15] C. T. G. Petit, R. Lan, P. I. Cowin, S. Tao, Structure and conductivity of strontium-doped cerium orthovanadates $Ce_{1-x}Sr_xVO_4$ ($0 \leq x \leq 0.175$), *J. Solid State Chem.* 183 (2010) 1231–1238.

[16] N. Ekthammathat, T. Thongtem, A. Phuruangrat, S. Thongtem, Synthesis and characterization of $CeVO_4$ by microwave radiation method and its photocatalytic activity, *J. Nanomater*. 2013 (2013) 1–7.

[17] E. V. Tsipis, M. V. Patrakeev, V. V. Kharton, N.P. Vyshatko, J.R. Frade, Ionic and p-type electronic transport in zircon-type $Ce_{1-x}A_xVO_4$ (A = Ca, Sr), *J. Mater. Chem.* 12 (2002) 3738–3745.

[18] F. Chen, X. L. Wang, S. Li, G. Fu, K. Wang, Q. Lu, et al., Low-loss optical planar waveguides in YVO_4 produced by silicon ion implantation at low doses, *J. Appl. Phys.* 94 (2003) 4708–4710.

[19] C. Au, W. Zhang, Oxidative dehydrogenation of propane over rare-earth orthovanadates, *J. Chem. Soc. Faraday Trans.* 93 (1997) 1195–1204.

[20] G. Picardi, F. Varsano, F. Decker, U. Krasovec, A. Surca, B. Orel, Electrochemical characterization of optically passive $CeVO_4$ counterelectrodes, *Electrochim. Acta.* 44 (1999) 3157–3164.

[21] R. A. Fields, M. Birnbaum, C. L. Fincher, Highly efficient Nd:YVO_4 diode-laser end-pumped laser, *Appl. Phys. Lett.* 51 (1987) 1885–1886.

[22] M. Yu, J. Lin, S. B. Wang, Effects of x and R^{3+} on the luminescent properties of Eu^{3+} in nanocrystalline $YV_xP_{1-x}O_4:Eu^{3+}$ and $RVO_4:Eu^{3+}$ thin-film phosphors, *Appl. Phys. A.* 80 (2005) 353–360.

[23] J. Liu, Q. Yao, Y. Li, Effects of downconversion luminescent film in dye-sensitized solar cells, *Appl. Phys. Lett.* 88 (2006) 173119.

[24] K. Gaur, H. B. Lal, Unusual magnetic behaviour of heavy rare earth vanadates at higher temperature, *J. Mater. Sci. Lett.* 2 (1983) 744–746.

[25] R. D. Shannon, Revised effective ionic radii and systematic studies of interatomic distances in halides and chalcogenides, Acta Cryst. A32 (1976) 751–767.

[26] B. Vaidhyanathan, K. Balaji, K. J. Rao, Microwave-assisted solid-state synthesis of oxide ion conducting stabilized bismuth vanadate phases, *Chem. Mater.* 10 (1998) 3400–3404.

[27] Y. Taninouchi, T. Uda, T. Ichitsubo, Y. Awakura, E. Matsubara, High oxide-ion conductivity of monovalent-metal-doped bismuth vanadate at intermediate temperatures, *Solid State Ionics*. 181 (2010) 719–723.

[28] J. Van Herle, A. McEvoy, K. R. Thampi, Conductivity measurements of various yttria-stabilised zirconia samples, *J. Mater. Sci.* 29 (1994) 3691–3701.

[29] S. Zha, C. Xia, G. Meng, Effect of Gd (Sm) doping on properties of ceria electrolyte for solid oxide fuel cells, *J. Power Sources.* 115 (2003) 44–48.

[30] C. Artini, M. Pani, M. M. Carnasciali, M. T. Buscaglia et al., Structural features of Sm- and Gd- doped ceria studied by synchrotron X-ray diffraction and μ-Raman spectroscopy, *Inorg. Chem.* 54(2015) 4126-4137.

[31] T. Ishihara, H. Matsuda, Y. Takita, Doped $LaGaO_3$ perovskite type oxide as a new oxide ionic conductor, *J. Am. Ceram. Soc.* 116 (1994) 3801-3803.

[32] P. N. Huang, A. Petric, Superior oxygen ion conductivity of lanthanum gallate doped with strontium and magnesium, *J. Electrochem. Soc.* 143 (1996) 1644-1648.

CHAPTER 6

SCOPE FOR FUTURE WORK

This chapter discusses the possible extensions of the work that may be pursued in future

Scope for future work

Reliable, clean and sustainable energy supply is more relevant today than ever before. Due to the increasing industrialization and population, the demand of energy is growing day by day. The existing energy supply systems, which are largely based on the combustion of fossil fuels, grounds for many environmental problems such as air pollution, acid gas emissions, and the emission of greenhouse gases. One of the largest issues at hand is that it is hard to create the quantity of energy that fossil fuel generators produce. Also, many renewable energy sources, such as wind and solar, rely on resources that aren't present forever. Furthermore, these alternative energy resources are typically more expensive when comparing them to fossil fuel costs. One of the most vital problems in the twenty-first century concerns both the logical use of energy resources and the decrease of toxic gases emission. This problem can be translated in terms of reduction of consumption of energy and increasing the use of advanced/efficient energy systems on a large scale.

Materials research is expected to play a growing part in sustainable technologies for energy conversion, storage and savings. Primary areas of research interest includes: solar cells, batteries and supercapacitors, fuel cells, thermoelectrics, superconductors, more efficient lighting and hydrogen technologies, sensors, catalysts etc. In most of these areas, incremental advancements of existing technologies are not adequate to address the important issues of durability, efficiency and costs. New materials research avenues are therefore essential to design, elaborate and incorporate materials for energy applications.

Solid state electrochemical cells based on oxygen ion conducting materials play crucial role for the generation of oxygen, gas purification (oxygen removal), generation of gases with known oxygen concentration and for precise control of oxygen levels in gas streams or enclosures. Wide range of applications includes medical, defence, on-site

calibration gases for sensors, food packaging (oxygen removal), aquaculture and several others. Worldwide market potential is of the order of several billion dollars.

The present study concentrates mainly on the structure-property correlation between the crystal structure, chemical composition and electrical properties of zircon-type mixed metal vanadates. A detailed investigation on the other zircon-type materials and the effect of different dopants may be done to understand the electrical property variation. Two synthesis methods are adopted for the present study, and it is interesting to study the various synthesis approaches to obtain better results. Development of new solid oxide ion conductor for various technological application including SOFC, sensor, ceramic membrane for gas separation, catalysts etc are of significant importance. Chemical stability and compatibility of the electrolyte is a prime requirement for the application point of view. When such compatibility between the electrode-electrolyte is achieved an SOFC unit or sensor unit can be fabricated and its total performance analysis can be done. There is a continuing requirement for the development of fast, sensitive, rugged, consistent, and economic sensors for applications in harsh industrial environments. Development of highly sensitive and selective sensors with long-term stability in such aggressive environments is another interesting topic to be pursued.

In summary, the work presented in this Ph.D. thesis is the beginning of a big research program to develop new class of oxide ion conductors which can be tuned to useful alternative for the conventional solid electrolytes in various energy related applications.

List of publications from the thesis

1. **T. H. Gayathri**, A. A. Yaremchenko, K. Zakharchuk, P. Abhilash, S. Ananthakumar "Impact of acceptor-type substitution on electrical transport properties of zircon-type $EuVO_4$", *J. Eur. Ceram. Soc*. 38 (2018) 145-151.
2. **T. H. Gayathri**, A. A. Yaremchenko, K. Zakharchuk, Jose James, Effect of magnesium addition on the structural, microstructural and electrical properties of YVO_4, *J. Alloys Compd.* 672 (2016) 549-557.
3. **T. H. Gayathri**, A. A. Yaremchenko, J. Macías, P. Abhilash, S. Ananthakumar, "Magnesium-doped zircon-type rare-earth orthovanadates: structural and electrical characterization", *Ceram. Int.* 44 (2018) 96-103.
4. **T. H. Gayathri**, A. A. Yaremchenko, J. Macías, P. Abhilash, S. Ananthakumar , "Oxide ion conductivity of monovalent metal (Li^+ and Ag+) doped $SmVO_4$ at intermediate temperatures" (Manuscript under preparation).

List of publications not related to thesis

1. **T. H. Gayathri**, A. A. Yaremchenko, J. Macías, P. Abhilash, S. Ananthakumar, Structural, microstructural and electrical characterizations of double perovskite Ba_2SmWO_6 (To be communicated)
2. L. S. Kumari, **T. H. Gayathri**, S. Sameera, P. Prabhakar Rao, "Y-Doped Bi_2MoO_6 Yellow Pigments for the Coloration of Plastics", *J. Am. Ceram. Soc*., 94 [2] 320–323 (2011), DOI: 10.1111/j.1551-2916.2010.04268.x.

Conference proceedings

1. **Gayathri T. H.** and Jose James, Electrical and dielectric properties of mixed metal vanadates, International conference on Advanced materials for power Engineering (ICAMPE -2015) Kottayam
2. **Gayathri T. H.** and Jose James, Role of RE^{3+} (Y^{3+}, Pr^{3+} And Sm^{3+}) on electrical and dielectric properties of mixed metal vanadates, International Conference Science, Technology and Application of Rare Earths (STAR 2015), Trivandrum**.**
3. **Gayathri T. H.** and Jose James, "Room temperature ionic conductivity of rare earth based mixed metal vanadates", 2^{nd} International Conference on Advanced Functional Materials (ICAFM 2014) Trivandrum**.**
4. **Gayathri T. H.** and Jose James, "Rare earth based mixed vanadates as solid electrolytes for SOFCs", National Seminar on Stimulating Concepts in Green Chemistry (SCGC)- 2014, SNM College, Maliankara
5. **Gayathri T. H.** and Jose James,*"* Frequency dependence of ionic conductivity in novel rare earth based mixed metal vanadates", NMAT-2013, Trivandrum.